Studying CP-violation using

$B^0 \to D^{*-}\rho^+$ at *BABAR*

Ajit Kurup

Physics Department
Royal Holloway, University of London

Submitted to the University of London
for the Degree of Doctor of Philosophy.
September 2002.

Abstract

The studies presented here investigate different techniques which could be used to measure CP-violating effects (i.e. measure $\sin(2\beta+\gamma)$) with the decay mode $B^0 \to D^{*-}\rho^+$, and its charge conjugate mode. To obtain a large sample of events, a partial reconstruction method is used to select signal events. The usefulness of this selection method was investigated by measuring the branching fraction $\mathcal{B}(B^0 \to D^{*-}\rho^+)$ and measuring the B^0 lifetime using 20.07 fb^{-1} of data collected with the *BABAR* detector at the PEP-II storage ring. A value of $(4.24 \pm 0.09 \pm 1.57) \times 10^{-3}$ was obtained for the branching fraction and a value of 1.75 ± 0.06 (stat.) ps for the B^0 lifetime. The discrepancy between the measured lifetime and the current best measurement of 1.548 ± 0.032 ps indicates that the technique used here needs to be improved before being used for $CP-$violation studies.

A toy Monte Carlo study was performed to investigate the improvement in the statistical error of $\sin(2\beta+\gamma)$ as a result of including measured decay angles. The statistical error, for a data sample of 10000 signal events, was found to be 1.6. This is significantly greater than the corresponding error in a similar effective parameter obtained by just measuring the decay time difference. However, including the measured decay angles provides an easier comparison with theoretical predictions.

Acknowledgments

I would like to thank:

- My parents and my sisters.
- My supervisor Glen Cowan and my adviser Mike Green.
- Abi Soffer for his help in showing me the ropes.
- The *BABAR* and PEP-II collaborations for building and running a fine experiment!
- "The Creator of the Universe" for the sunshine (and the occasional downpour) in California!
- Chris Marker for giving me the title of chapter 2!
- All the people who have made doing this PhD a very enjoyable experience. Especially those who have been generous in providing libation!

One more thing, the missing anti-matter is not in the fridge!

Declaration

Contents

List of Figures

List of Tables

Chapter 1

Introduction

> "'All hands to tackle!' They sprang to orders, hoisting the pinewood mast, they stepped it firm in its block amid ships, lashed it fast with stays and with braided rawhide halyards hauled the white sail high. Suddenly wind hit full and the canvas bellied out and a dark blue wave, foaming up at the bow, sang out loud and strong as the ship made way, skimming the whitecaps, cutting toward her goal."
>
> The Odyssey, Homer.

$CP-$violation is a necessary ingredient of the explanation for why we live in a matter dominated universe. $CP-$violation was first discovered in 1964 in the K-meson system. It has only recently been possible, with the use of B-factories (e.g. PEP-II), to investigate $CP-$violation in the B-meson system and thus provide new tests of our explanation for $CP-$violation.

This thesis presents an analysis of the decay mode $B^0 \to D^{*-}\rho^+$ (and its charge conjugate $\overline{B}^0 \to D^{*+}\rho^-$), which can be used to measure the $CP-$violation parameter $\sin(2\beta+\gamma)$, where β and γ are two angles of the unitarity triangle. The work presented here includes measurements of the $B \to D^*\rho$ branching fraction and of the neutral B meson lifetime. A study has also been done to investigate the possibility of using an angular analysis to obtain an improved measurement of $\sin(2\beta+\gamma)$.

To obtain a large sample of $B \to D^*\rho$ events, a partial reconstruction technique has been developed. This allows the kinematics of the decay to be determined without having to reconstruct the $\overline{D}^0$ produced by the D^* decay. However, using this partial reconstruction method introduces a significant amount of background in the event sample. The process of measuring the $B \to D^*\rho$ branching fraction would allow

us to determine if this would cause significant problems for measuring $\sin(2\beta+\gamma)$ in this channel. Another important aspect of the measurement of $\sin(2\beta+\gamma)$ is the ability to accurately reconstruct the decay vertices of the B mesons. By measuring the B lifetime it is possible to study how background events in the sample will affect this.

It has been proposed [36] that the measurement of $\sin(2\beta+\gamma)$ might be improved by including measurements of the angles between certain decay products. The benefits of including more information in the fit could however be outweighed by the increased complexity of the fit procedure. A toy Monte Carlo study was performed to investigate the potential of this technique to measure $\sin(2\beta+\gamma)$.

Chapter 2

Theoretical Overview

> "Thou didst hasten on in search of knowledge, of light, of the sun. Thy only thought was to reach the pure air, the broad day of eternal truth; but, in rushing toward the dazzling loophole which opens upon another world - a world of brightness, of intellect, of science - infatuated fly! insensate sage! thou didst not see the subtle web suspended by destiny between the light and thee."
>
> The Hunchback of Notre-Dame, Victor Hugo.

Our current understanding of the way nature behaves can be described by general relativity and quantum mechanics. General relativity describes the gravitational interaction of matter at macroscopic scales, whereas quantum mechanics describes the behaviour of matter at microscopic scales. Quantum mechanics was first developed by Max Planck, in 1900, to explain the observed black-body radiation spectrum. Planck made the assumption that the allowed photon frequencies were quantised. This assumption was confirmed by Einstein, in 1905, who used this quantisation of energy levels to explain the photo-electric effect. Since the development of quantum mechanics in the 1920s and specifically, its application to the description of point-like particles, it has successfully been used to describe many observed phenomena and has led to our current understanding of the interaction of particles at the quantum scale, which is known as the Standard Model. Throughout the last century, experimental evidence and developments in theory have led to the understanding that all observable phenomena can be described by the interaction of twelve particle types with four fundamental forces. Three of these forces act at the quantum scale and are described by quantum field theory. The fourth, gravity, acts at much larger scales

and is not incorporated in the Standard Model. Other theories, such as supersymmetric string theories, include gravity. However, current technology is not able to probe the energies where it would be possible to test these theories.

The Standard Model consists of six quarks and six leptons and describes their interactions with the electromagnetic, the weak and the strong force. These forces are mediated by gauge bosons, which can be described by a quantum field theory. The quarks and leptons are grouped into three families:

$$\text{Quarks} \qquad \begin{pmatrix} u \\ d \end{pmatrix} \quad \begin{pmatrix} c \\ s \end{pmatrix} \quad \begin{pmatrix} t \\ b \end{pmatrix}. \tag{2.1}$$

$$\text{Leptons} \qquad \begin{pmatrix} e \\ \nu_e \end{pmatrix} \quad \begin{pmatrix} \mu \\ \nu_\mu \end{pmatrix} \quad \begin{pmatrix} \tau \\ \nu_\tau \end{pmatrix}. \tag{2.2}$$

The electromagnetic force is mediated by the photon (γ), the weak force is mediated by three gauge bosons ($W^{\pm}$ and Z) and the strong force is mediated by eight gluons (g). By requiring invariance of the Lagrangian describing the quantum fields under certain types of gauge transformation, the interactions of all of these particles are determined. Table 2.1 lists some basic properties of the quarks, leptons and gauge bosons. The quarks interact with all three forces, whereas the massive leptons only interact with the electromagnetic and weak forces and the massless leptons, i.e. neutrinos (ν_x), only interact with the weak force. Only two of the six types of quarks (u and d) are used to make up the atoms of every-day matter. The other quarks are only produced at high energies and therefore would have only existed, in abundance, just after the big bang. The strong force is responsible for binding quarks together to form mesons and baryons. In the early 1960's, a large number of baryons had been observed but a few posed problems for the current theory of the strong interaction. For example, the Δ^{++} has spin 3/2 and is composed of three u quarks. However, since the quarks are fermions they cannot all be in the same quantum state. This problem was solved by Greenberg [1], in 1964, who introduced a new quantum number called colour. A quark can have one of three possible colours red, green or blue and therefore the Δ^{++} is composed of three u quarks each of different colours and is itself colour neutral. Thus, the three u quarks that make up the Δ^{++} are not

Particle	Charge(e)	Spin	Mass
Quarks			
u	$2/3$	$1/2$	$1-5\,\mathrm{MeV}$
d	$-1/3$	$1/2$	$3-9\,\mathrm{MeV}$
s	$-1/3$	$1/2$	$75-170\,\mathrm{MeV}$
c	$2/3$	$1/2$	$1.15-1.35\,\mathrm{MeV}$
b	$-1/3$	$1/2$	$4.0-4.4\,\mathrm{GeV}$
t	$2/3$	$1/2$	$174.3\pm5.1\,\mathrm{GeV}$
Leptons			
e	-1	$1/2$	$0.5110\,\mathrm{MeV}$
μ	-1	$1/2$	$105.7\,\mathrm{MeV}$
τ	-1	$1/2$	$1.777\,\mathrm{GeV}$
ν_e	0	$1/2$	0
ν_μ	0	$1/2$	0
ν_τ	0	$1/2$	0
Gauge Bosons			
γ	0	1	0
g	0	1	0
Z	0	1	$91.2\,\mathrm{GeV}$
W^+	1	1	$80.4\,\mathrm{GeV}$

Table 2.1: Properties of quarks, leptons and gauge bosons. Only the matter particles have been listed. The charge conjugate (i.e. anti-matter) particles have the same values for spin and mass but opposite sign charges.

in the same quantum state. The interaction between colour charges can be described by an $SU(3)$ gauge group and by requiring invariance of the Lagrangian under $SU(3)$ transformations, eight particles, called gluons, are introduced that mediate the strong force.

For a quantum field theory where the Lagrangian is invariant under Lorentz transformations, it can be shown that it must also be invariant under the combined discrete symmetry operations of parity (P), charge-conjugations (C) and time reversal (T). Parity is the operation of spatial reversal, i.e. $x, y, z \rightarrow -x, -y, -z$, charge conjugation is the exchange of particle for anti-particle and time reversal is the temporal reversal of a process. One consequence of the invariance of the Lagrangian under CPT transformations is that the masses and lifetimes of particles and their anti-particles are the same. The violation of parity was proposed by Lee and Yang [2], in 1956, to solve the problem of the spin-parity assignments of the decay of kaons to two and three pions. It was pointed out in their paper that parity conservation could be studied by looking at β-decay and in 1957, Wu *et al.* [3] observed parity violation in the β-decay of ^{60}Co. It was found that the direction of the emitted electrons, from the β-decay, was not isotropic and that they were emitted preferentially in a direction opposite to the nuclear spin direction. Thus in the parity transformed process, where the nuclear spin direction stays the same but the momentum vector of the electron is reversed, the emission of the electrons will be preferentially in the same direction as the nuclear spin instead of in the opposite direction. This shows that the weak force is not invariant under parity transformations. Subsequent measurements of the neutrino helicity and the angular distributions in the decay sequence $\pi \rightarrow \mu \rightarrow e$, showed that the weak force not only maximally violates parity but also maximally violates charge-conjugation.

It was thought however, that the combined operation of parity and charge-conjugation (CP) was a symmetry of the weak interaction. This was shown not to be true by Christenson, Cronin, Fitch and Turlay in 1964 [4]. In their experiment, the branching fraction of the long lived neutral kaon decaying to two charged pions was found to be non-zero, i.e. $\mathcal{B}(K^0_{\rm L} \rightarrow \pi^+\pi^-) = (2.0 \pm 0.4) \times 10^{-3}$. It was thought that $K^0_{\rm L}$ was the CP-odd state, K^0_2 and so the decay $K^0_2 \rightarrow \pi^+\pi^-$ violates CP. Thus, the results of the experiment led to a redefinition of the $K^0_{\rm S}$ and $K^0_{\rm L}$

mesons being mixtures of the CP eigenstates K_1^0 and K_2^0,

$$\left|K_{\rm S}^0\right\rangle = \frac{|K_1^0\rangle + \epsilon\,|K_2^0\rangle}{\sqrt{1+|\epsilon|^2}},$$
$$\left|K_{\rm L}^0\right\rangle = \frac{|K_2^0\rangle + \epsilon\,|K_1^0\rangle}{\sqrt{1+|\epsilon|^2}}, \tag{2.3}$$

where ϵ is a small complex number that gives the degree of $CP-$violation due to the mixing of the kaon states. $CP-$violation also exists in the decays of other particles and is expected to show a large effect in the B meson system. The following sections describe how $CP-$violation arises in the Standard Model and its relevance to the decay of B mesons and, in particular, $B^0 \to D^{*-}\rho^+$.

2.1 The Standard Model and CP-violation

Over the period 1961-1968 Glashow, Salam and Weinberg [5] unified the theories of the electromagnetic and the weak force and it is from the spontaneous symmetry breaking of this, via the Higgs mechanism, that $CP-$violation arises. The electro-weak interaction can be described by a $SU(2)_L \otimes U(1)_Y$ group, where the $SU(2)_L$ indicates that the charged current part of the weak force only couples to left-handed fermions. This is a result of experimental evidence that shows the weak force maximally violates P and C and that right-handed neutrinos have not been observed. By requiring $SU(2)_L \otimes U(1)_Y$ gauge invariance, the electro-weak Langrangian density can be written as

$$\mathcal{L} = \mathcal{L}(f,W,B) + \mathcal{L}(f,\Phi) + \mathcal{L}(W,B,\Phi) - V(\Phi). \tag{2.4}$$

The first term describes the interaction of fermions (f) with the massless gauge bosons (W and B) of the electro-weak field. The second term describes the interaction of fermions with the scalar Higgs doublet (Φ) field where

$$\Phi = \begin{pmatrix} \phi^+ \\ \phi^0 \end{pmatrix} \text{ and } \Phi^\dagger = \begin{pmatrix} \phi^- \\ \overline{\phi}^0 \end{pmatrix}. \tag{2.5}$$

The third term gives the interaction of the gauge bosons with the Higgs field and the last term gives the potential of the Higgs field. The leptons and quarks interact in left-handed doublets and right-handed singlets. The neutrinos are assumed to have no mass, therefore only left-handed neutrinos and right-handed anti-neutrinos are included in this model. The gauge bosons are divided into a triplet (W_μ^i) and a singlet (B_μ) that are the $SU(2)_L$ and $U(1)_Y$ gauge bosons, respectively.

$CP-$violation in the Standard Model is due to quark mixing in charged current interactions, which is a result of the fact that the quark flavour eigenstates are not the same as the mass eigenstates. The fermions, gauge bosons and neutral scalar field acquire mass after spontaneous symmetry breaking through the Higgs mechanism. As a result of this, the second term in Eq. 2.4 becomes

$$\begin{aligned}\mathcal{L}(f,\phi)^{SSB} &= \sum_{j=1}^{3}(m_j)_l \overline{l}_L^j l_R^j \left(1+\frac{\phi}{v}\right) \\ &- \sum_{j,k=1}^{3}\left[(m_{jk})_U \overline{u}_L^j u_R^k + (m_{jk})_D \overline{d}_L^j d_R^k\right]\left(1+\frac{\phi}{v}\right) + \text{h.c.}, \end{aligned} \tag{2.6}$$

where the three terms give the interaction of the left and right handed leptons (l_L and l_R), up-type quarks (u_L and u_R) and down-type quarks (d_L and d_R) with the physical Higgs scalar ϕ and v is the neutral Higgs vacuum expectation value. The mass terms $(m_j)_l$ and $(m_{jk})_{U,D}$ are proportional to the Yukawa coupling terms, which are arbitrary complex numbers. Therefore the mass matrices m_U and m_D are not diagonal. In order to write the Lagrangian in Eq. 2.6 in terms of the quark mass eigenstates m_U and m_D need to be diagonalised using two unitary matrices

$$V_L^{up} m_U V_R^{up\dagger} = m_U^{phys.} = \begin{pmatrix} m_u & & 0 \\ & m_c & \\ 0 & & m_t \end{pmatrix}, \tag{2.7}$$

$$V_L^{down} m_D V_R^{down\dagger} = m_D^{phys.} = \begin{pmatrix} m_d & & 0 \\ & m_s & \\ 0 & & m_b \end{pmatrix}, \tag{2.8}$$

where the diagonal elements are the masses of the quarks and all other elements are

zero. The up-type quark term in Eq. 2.6 then becomes

$$\begin{aligned} \overline{u}_L m_U u_R &= \overline{u}_L V_L^{up\dagger} V_L^{up} m_U V_R^{up\dagger} V_R^{up} u_R \\ &= \overline{u_L V_L^{up}} m_U^{phys.} V_R^{up} u_R \end{aligned} \tag{2.9}$$

and similarly for the down-type term. Thus, the quark mass eigenstates are given by

$$u_L^{phys.} = V_L^{up} u_L \tag{2.10}$$

$$d_L^{phys.} = V_L^{down} d_L. \tag{2.11}$$

As mentioned earlier, CP-violating processes are due to flavour changing, charged current interactions. The quark, charged current part of $\mathcal{L}(f, W, B)$, after spontaneous symmetry breaking, can be written as

$$\mathcal{L}^{CC} = \frac{e}{2\sqrt{2}\sin^2\theta_w} \sum_{i=1}^{3} \overline{u}_L^i \gamma^\mu W_\mu^+ d_L^i + \text{h.c.}, \tag{2.12}$$

where θ_w is the electroweak mixing angle and comes from the diagonalisation of the gauge boson mass matrix. Writing $\mathcal{L}^{CC}$ in terms of the mass eigenstates, using $V^\dagger V = 1$, gives:

$$\mathcal{L}^{CC} = \frac{e}{2\sqrt{2}\sin^2\theta_w} \sum_{i=1}^{3} \overline{u}_L^i V_L^{up\dagger} V_L^{up} \gamma^\mu W_\mu^+ V_L^{down\dagger} V_L^{down} d_L^i + \text{h.c.} \tag{2.13}$$

$$= \frac{e}{2\sqrt{2}\sin^2\theta_w} \sum_{i=1}^{3} \left(\overline{u}_L^{phys.}\right)^i \gamma^\mu W_\mu^+ \left(V_L^{up} V_L^{down\dagger}\right)_{ij} \left(d_L^{phys.}\right)^j + \text{h.c.} \tag{2.14}$$

$$= \frac{e}{2\sqrt{2}\sin^2\theta_w} \overline{u}_L^{phys.} \gamma^\mu W_\mu^+ V_{\text{CKM}} d_L^{phys.} + \text{h.c.}, \tag{2.15}$$

where V_{CKM} was first written down by Kobayashi and Maskawa in 1973 [6] and is referred to as the CKM matrix. Thus, the physical up-type quark states couple to a mixture of down-type quarks where the strength of the coupling is given by the elements of V_{CKM}. There are no restrictions on V_{CKM} except $V_{\text{CKM}}^\dagger V_{\text{CKM}} = 1$. V_{CKM}

can be symbolically written as

$$V_{\rm CKM} = \begin{pmatrix} V_{ud} & V_{us} & V_{ub} \\ V_{cd} & V_{cs} & V_{cb} \\ V_{td} & V_{ts} & V_{tb} \end{pmatrix}, \tag{2.16}$$

where V_{ij} is a complex number that represents the coupling of quark i to j. So, the quark, charged current Lagrangian, $\mathcal{L}^{CC}$, will violate CP if $V_{\rm CKM}$ contains a non-trivial complex phase.

2.1.1 Representations of the CKM Matrix

Since measurable quantities are related to the square of the amplitude, it is possible to redefine the CKM matrix using a similarity transform

$$V'_{\rm CKM} = U^{\dagger} V_{\rm CKM} U. \tag{2.17}$$

This transformation does not change any physically observable quantities but the freedom to be able to make this transformation leads to a constraint on the number of complex parameters that the matrix can have. For any unitary 3x3 matrix there is one complex phase and 3 real parameters. Thus, all CP-violating effects in the Standard Model are due to the one complex phase parameter in the CKM matrix. The parameterisation due to Wolfenstein [7] is a convenient way of expressing this but is only an approximation up to terms $\mathcal{O}(\lambda^4)$. In this case the CKM matrix is given by

$$V_{\rm CKM} \approx \begin{pmatrix} 1 - \frac{\lambda^2}{2} & \lambda & A\lambda^3 (\rho - i\eta) \\ -\lambda & 1 - \frac{\lambda^2}{2} & A\lambda^2 \\ A\lambda^3 (1 - \rho - i\eta) & -A\lambda^2 & 1 \end{pmatrix}, \tag{2.18}$$

where A, λ, η and ρ are real and η represents the magnitude of the CP-violating phase. The parameter $A \approx 1$ and $\lambda = \sin\theta_c \approx 0.221$, where θ_c is the Cabibbo angle that describes two generation quark mixing [8]. Thus all CP-violating effects in the Standard Model are related to η.

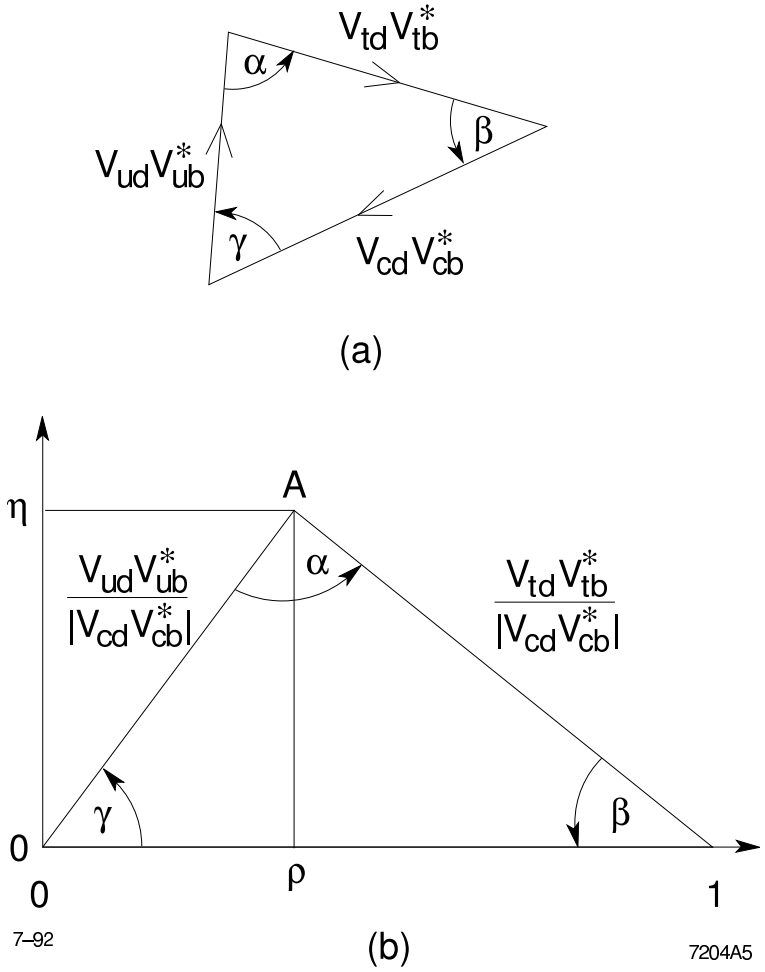

Figure 2.1: (a) The unitarity triangle corresponding to Eq. 2.20. (b) The unitarity triangle with the sides normalised by $|V_{cd}V_{cb}^*|$ and with the Wolfenstein parameters ρ and η indicated [10].

The unitarity of $V_{\rm CKM}$ leads to a number of relations of the form

$$\sum_i V_{ij}V_{ik}^* = 0, \tag{2.19}$$

where i is summed over up-type quarks, j and k are down-type quarks and $j \neq k$. These relations can be visualised as triangles in the complex plane. The most interesting for B physics is

$$V_{ud}V_{ub}^* + V_{cd}V_{cb}^* + V_{td}V_{tb}^* = 0. \tag{2.20}$$

The triangle corresponding to Eq. 2.20, commonly referred to as the unitarity triangle, is illustrated in Fig. 2.1. Measurements of the interior angles of this triangle can

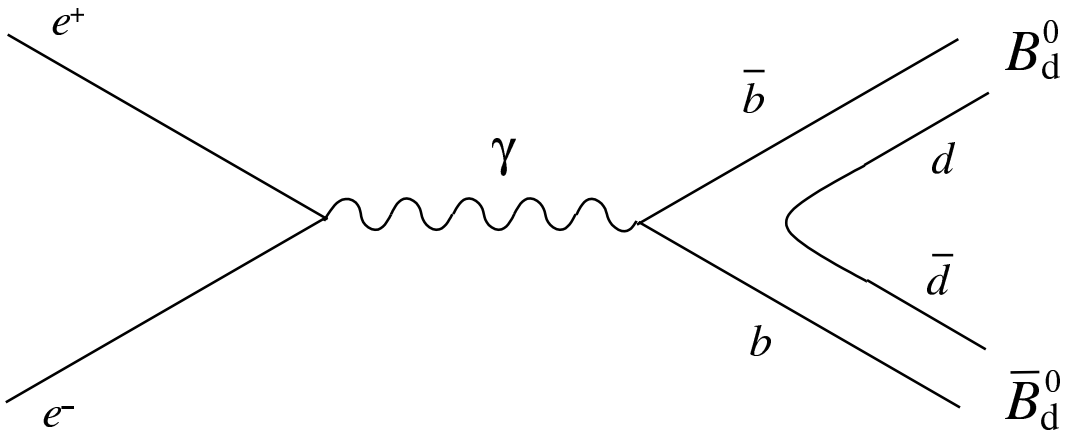

Figure 2.2: Feynman diagram of the production of the $\Upsilon(4S)$ and its decay to a pair of $B_{\rm d}\overline{B}_{\rm d}$ mesons.

be obtained from the time-dependent decay rates of B mesons. Since these angles are large and of comparable size, CP-violating effects in the B meson system are expected to be relatively large.

2.2 CP-violation in the B Meson System

The first experimental evidence for the existence of the b quark came in 1977 with the discovery of the Υ meson, which is the bound state of a $b\overline{b}$ quark pair. Higher resonances of the Υ were later studied by the CLEO experiment and it was found that the $\Upsilon(4S)$ is the lightest resonance that is able to decay, via the strong force, to a pair of $B\overline{B}$ mesons, as illustrated in Fig. 2.2. Table 2.2 lists the properties of the B mesons that have been observed. The following introduces the $CP-$violation physics

Meson	Quark Content	Mass(GeV/c^2)	Mean Lifetime (s)
B_u^+	$u\overline{b}$	5.2790 ± 0.0005	$(1.653 \pm 0.028) \times 10^{-12}$
B_d^0	$d\overline{b}$	5.2794 ± 0.0005	$(1.548 \pm 0.032) \times 10^{-12}$
B_s^0	$s\overline{b}$	5.3696 ± 0.0024	$(1.493 \pm 0.062) \times 10^{-12}$
B_c^+	$c\overline{b}$	6.4 ± 0.4	$\left(0.46^{+0.18}_{-0.16}\right) \times 10^{-12}$

Table 2.2: Properties of B mesons from the Review of Particle Physics [9].

that can be studied by the *BABAR* experiment and in particular, the theoretical motivation for studying $B^0 \to D^{*-}\rho^+$. A more general description of B physics can

be found in [10] and [11].

The primary objective of the *BABAR* experiment is to study the decays of B_d and B_u mesons, which are commonly referred to as B^0 and B^+, produced by the decays of the $\Upsilon(4S)$. The centre-of-mass (CM) energy of PEP-II is at the threshold for production of the $\Upsilon(4S)$, i.e. 10.58 GeV and the $\Upsilon(4S)$ almost always decays to a $B^0\overline{B}^0$ or a B^+B^- pair, i.e. $\mathcal{B}(\Upsilon(4S) \to B^0\overline{B}^0) \approx \mathcal{B}(\Upsilon(4S) \to B^+B^-) \approx 50\%$. In order to study most of the CP-violating effects at this energy, it is necessary to measure time-dependent decays rates. PEP-II was designed to have different energies for the e^+ and the e^- beams so that the CM will be moving in the laboratory frame. This means that the $B\overline{B}$ pair is boosted in the lab frame by an amount sufficient to allow the separation of the decay vertices of the B mesons to be measured. Using this measured separation and the known boost of the CM, the time difference between the decays of the B mesons can be measured. Since the B mesons are produced in a coherent $L = 1$ state, it is possible to measure the time-dependent decay rates from the time difference between the subsequent decays of the $B\overline{B}$ pair. Thus, the measurement of the separation of the B decay vertices is crucial for studying $CP-$violation using *BABAR*.

There are three basic types of CP-violating phenomena; CP-violation in decay, CP-violation in mixing and CP-violation due to decay and mixing. The following sections describe how these effects are manifest in the B meson system.

2.2.1 CP-violation in Decay

CP-violation in decay is due to the fact that the amplitude for a particular decay is not the same as the amplitude for the CP-conjugate decay. The amplitude for a decay (and its CP-conjugate) can symbolically be written as the sum over all amplitudes that contribute to the decay

$$\begin{aligned} A_f &= \sum_i A_i e^{i(\delta_i+\phi_i)} \text{ and} \\ \overline{A}_{\overline{f}} &= \sum_i e^{2i\left(\xi_f-\xi_B\right)} A_i e^{i(\delta_i-\phi_i)}, \end{aligned} \tag{2.21}$$

where A_i is the magnitude of the amplitude of term i. The phases δ_i are due to strong interaction effects such as rescattering. The phases ϕ_i, often referred to as weak phases, are products of CKM matrix elements and are due to flavour changing weak interactions. The phase ξ is a convention-dependent phase introduced by the CP transformation. If f is a CP eigenstate, $e^{2i\xi_f} = \pm 1$. Thus CP-violation in decay is equivalent to the statement

$$\left|\overline{A}_{\overline{f}}/A_f\right| = \left|\frac{\sum_i A_i e^{i(\delta_i+\phi_i)}}{\sum_i e^{2i\left(\xi_f-\xi_B\right)} A_i e^{i(\delta_i-\phi_i)}}\right| \neq 1. \tag{2.22}$$

Therefore CP-violation of this type will not occur unless at least two terms with different weak phases have different strong phases, since

$$|A|^2 - |\overline{A}|^2 = -2\sum_{i,j} A_i A_j \sin(\phi_i - \phi_j)\sin(\delta_i - \delta_j). \tag{2.23}$$

2.2.2 CP-violation in Mixing

The two neutral B mesons produced in the $\Upsilon(4S)$ decay can oscillate between the B^0 and $\overline{B}^0$ states via the Feynman diagrams given in Fig. 2.3. The flavour eigenstates, $|B^0\rangle$ and $\left|\overline{B}^0\right\rangle$, are eigenstates of the strong and electromagnetic interactions but are not eigenstates of the weak interaction. The Hamiltonian in the flavour eigenstate basis is given by

$$H = M - \frac{i}{2}\Gamma = \begin{bmatrix} M & M_{12} \\ M_{12}^* & M \end{bmatrix} - \frac{i}{2}\begin{bmatrix} \Gamma & \Gamma_{12} \\ \Gamma_{12}^* & \Gamma \end{bmatrix}, \tag{2.24}$$

where, M (Γ) is the mass (decay width) of the flavour eigenstates. The off-diagonal terms, M_{12} and Γ_{12} are responsible for the $B^0\overline{B}^0$ transition. Diagonalising H gives us the weak interaction (and mass) eigenstates $|B_H\rangle$ and $|B_L\rangle$

$$\begin{aligned} |B_L\rangle &= p\left|B^0\right\rangle + q\left|\overline{B}^0\right\rangle, \\ |B_H\rangle &= p\left|B^0\right\rangle - q\left|\overline{B}^0\right\rangle, \end{aligned} \tag{2.25}$$

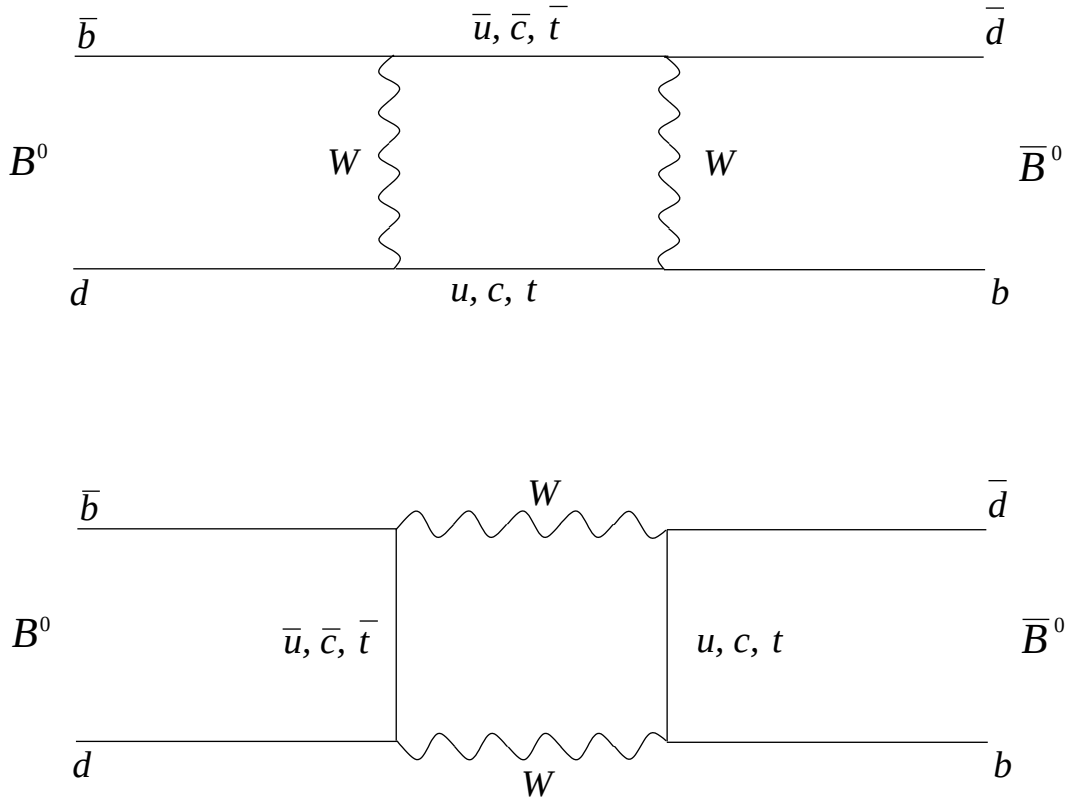

Figure 2.3: Feynman diagrams of $B^0\overline{B}^0$ mixing.

where p and q are complex coefficients and obey the relation

$$|q|^2 + |p|^2 = 1. \tag{2.26}$$

The eigenstates $|B_H\rangle$ and $|B_L\rangle$ are often referred to as the heavy and light mass eigenstate, respectively, since

$$\Delta m = M_H - M_L > 0. \tag{2.27}$$

The condition for $CP-$violation in $B^0\overline{B}^0$ mixing to exist is

$$\left|\frac{q}{p}\right|^2 = \left|\frac{M_{12}^* - \frac{i}{2}\Gamma_{12}^*}{M_{12} - \frac{i}{2}\Gamma_{12}}\right| \neq 1. \tag{2.28}$$

For the B meson system, the Γ_{12} term is very small. Therefore, q/p approximates to

$$\frac{q}{p} \approx \sqrt{\frac{M_{12}^*}{M_{12}}} = e^{-i2\beta}, \tag{2.29}$$

where β is an angle of the unitarity triangle illustrated in Fig. 2.1.

2.2.3 CP-violation in Decay and Mixing

This type of $CP-$violation is possible for decay modes where the final state can be produced by the decay of a B or a $\overline{B}$. In the case where

$$\left|\frac{A_f}{\overline{A_{\overline{f}}}}\right| = 1 \text{ and } \left|\frac{q}{p}\right| = 1, \tag{2.30}$$

$CP-$violation can still occur due to the interference between decays with and without mixing. In this case

$$\mathrm{Im}(\lambda) \neq 0, \tag{2.31}$$

where

$$\lambda = \frac{q}{p}\frac{\overline{A}_f}{A_f}. \tag{2.32}$$

This is the case for $B \to D^*\rho$. The following section describes the theoretical motivation for studying $CP-$violation in $B \to D^*\rho$.

2.3 Theoretical Motivation for Studying $B^0 \to D^{*-}\rho^+$

The primary goal of studying $B^0 \to D^{*-}\rho^+$ is to measure the parameter $\sin(2\beta+\gamma)$, where β and γ are angles of the unitarity triangle illustrated in Fig. 2.1. Feynman diagrams of the decays that are considered are illustrated in Fig. 2.4 and their amplitudes can be written as

$$\mathcal{A} = Amp(B^0 \to D^{*-}\rho^+) = ae^{i\delta^a}, \tag{2.33}$$

$$\overline{\mathcal{A}} = Amp(\overline{B}^0 \to D^{*+}\rho^-) = ae^{i\delta^a}, \tag{2.34}$$

$$\mathcal{A}' = Amp(\overline{B}^0 \to D^{*-}\rho^+) = be^{i\delta^b}e^{-i\gamma}, \tag{2.35}$$

$$\overline{\mathcal{A}}' = Amp(B^0 \to D^{*+}\rho^-) = be^{i\delta^b}e^{i\gamma}, \tag{2.36}$$

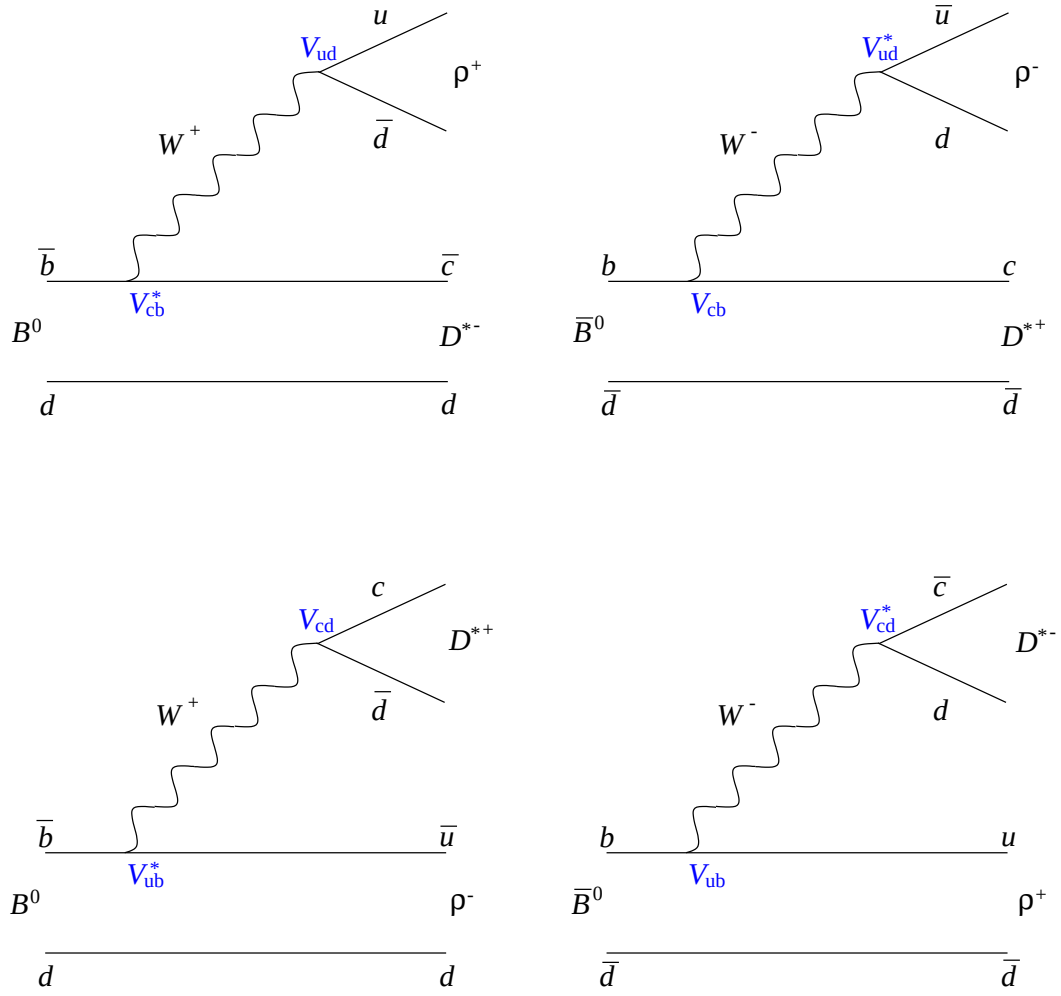

Figure 2.4: Feynman diagrams of the $B \to D^*\rho$ decays considered. The CKM matrix element V_{xy} (in blue) involved at each vertex is noted. The bottom two diagrams (whose corresponding amplitudes are Eq. 2.36 and Eq. 2.35) are referred to as suppressed modes since $|V_{cb}| \gg |V_{ub}|$.

where a and b are the magnitudes of the amplitudes, δ^i is the strong phase (as in Eq. 2.21) and γ is the angle of the unitarity triangle. For each decay, the B meson that decays could have undergone mixing prior to it decaying. Since $|V_{cb}| \gg |V_{ub}|$ (and therefore $a \gg b$) the amplitudes given by Eq. 2.35 and Eq. 2.36 are referred to as suppressed decays. The interference between the amplitudes for decays with and without mixing is therefore expected to be small. The interference between decays with and without mixing allows the parameter $\sin(2\beta + \gamma)$ to be measured from the time-dependent decay rate. The form for the time-dependent decay rate can be derived as follows. Consider the mass eigenstates B_H and B_L in Eq. 2.25. Writing

the flavour eigenstates in terms of the mass eigenstates gives

$$\begin{aligned}\left|B^0\right\rangle &= \frac{|B_L\rangle + |B_H\rangle}{2p},\\ \left|\overline{B}^0\right\rangle &= \frac{|B_L\rangle - |B_H\rangle}{2q}.\end{aligned} \tag{2.37}$$

The time evolution of the mass eigenstates is given by

$$\begin{aligned}|B_L(t)\rangle &= e^{-t\left(\frac{\Gamma}{2}+iM_L\right)}|B_L\rangle,\\ |B_H(t)\rangle &= e^{-t\left(\frac{\Gamma}{2}+iM_H\right)}|B_H\rangle.\end{aligned} \tag{2.38}$$

where the difference in widths is neglected, i.e.

$$\Gamma \equiv \Gamma_H = \Gamma_L, \tag{2.39}$$

since $\Delta\Gamma \ll \Gamma$. Therefore the time evolution of a state which is initially a B^0 or $\overline{B}^0$ is given by substituting Eq. 2.38 into Eq. 2.37

$$\left|B^0(t)\right\rangle = \frac{1}{2p}\left(e^{-t\left(\frac{\Gamma}{2}+iM_L\right)}|B_L\rangle + e^{-t\left(\frac{\Gamma}{2}+iM_H\right)}|B_H\rangle\right), \tag{2.40}$$

$$\left|\overline{B}^0(t)\right\rangle = \frac{1}{2q}\left(e^{-t\left(\frac{\Gamma}{2}+iM_L\right)}|B_L\rangle - e^{-t\left(\frac{\Gamma}{2}+iM_H\right)}|B_H\rangle\right). \tag{2.41}$$

Using Eq. 2.27 and

$$M = \frac{M_H + M_L}{2} \tag{2.42}$$

gives

$$\left|B^0(t)\right\rangle = \frac{1}{2p}e^{-t\left(\frac{\Gamma}{2}+iM\right)}\left[e^{i\frac{\Delta mt}{2}}|B_L\rangle + e^{-i\frac{\Delta mt}{2}}|B_H\rangle\right], \tag{2.43}$$

$$\left|\overline{B}^0(t)\right\rangle = \frac{1}{2q}e^{-t\left(\frac{\Gamma}{2}+iM\right)}\left[e^{i\frac{\Delta mt}{2}}|B_L\rangle - e^{-i\frac{\Delta mt}{2}}|B_H\rangle\right]. \tag{2.44}$$

Writing this in terms of the flavour eigenstates (using Eq. 2.25) leads to the following expressions

$$\left|B^0(t)\right\rangle = e^{-t\left(\frac{\Gamma}{2}+iM\right)}\left[\cos\left(\frac{\Delta mt}{2}\right)\left|B^0\right\rangle + i\frac{q}{p}\sin\left(\frac{\Delta mt}{2}\right)\left|\overline{B}^0\right\rangle\right],$$

$$\left|\overline{B}^0(t)\right\rangle = e^{-t\left(\frac{\Gamma}{2}+iM\right)}\left[\cos\left(\frac{\Delta mt}{2}\right)\left|\overline{B}^0\right\rangle + i\frac{p}{q}\sin\left(\frac{\Delta mt}{2}\right)\left|B^0\right\rangle\right]. \tag{2.45}$$

The amplitude for these states to decay to a final state $\langle f|$ is therefore given by

$$\begin{aligned}\langle f|\,H\left|B^0(t)\right\rangle &= \mathcal{A}e^{-t\left(\frac{\Gamma}{2}+iM\right)}\left[\cos\left(\frac{\Delta mt}{2}\right)+i\lambda\sin\left(\frac{\Delta mt}{2}\right)\right],\\ \langle f|\,H\left|\overline{B}^0(t)\right\rangle &= \mathcal{A}\frac{p}{q}e^{-t\left(\frac{\Gamma}{2}+iM\right)}\left[\lambda\cos\left(\frac{\Delta mt}{2}\right)+i\sin\left(\frac{\Delta mt}{2}\right)\right],\end{aligned} \tag{2.46}$$

where

$$\lambda = \frac{q}{p}\frac{\mathcal{A}'}{\mathcal{A}} \tag{2.47}$$

and $\mathcal{A}$ and $\mathcal{A}'$ are given by Eq. 2.33 and Eq. 2.35, respectively. The time-dependent decay rate is then given by

$$\Gamma\left(B^0(t)\to f\right) = |\mathcal{A}|^2 e^{-\Gamma t}\left[\begin{array}{l}\frac{1+|\lambda|^2}{2}+\frac{1-|\lambda|^2}{2}\cos\left(\Delta mt\right)\\ -\mathrm{Im}(\lambda)\sin\left(\Delta mt\right)\end{array}\right], \tag{2.48}$$

$$\Gamma\left(\overline{B}^0(t)\to f\right) = |\mathcal{A}|^2 e^{-\Gamma t}\left[\begin{array}{l}\frac{1+|\lambda|^2}{2}-\frac{1-|\lambda|^2}{2}\cos\left(\Delta mt\right)\\ +\mathrm{Im}(\lambda)\sin\left(\Delta mt\right)\end{array}\right], \tag{2.49}$$

where $\mathrm{Im}(\lambda) = \sin(2\beta+\gamma)$ if strong phases are neglected. As mentioned before, the $B\overline{B}$ pair is produced in a coherent state. This means that the decay rate, as a function of the time between the decays of the $B\overline{B}$ pair (Δt), has exactly the same form as Eq. 2.48 and Eq. 2.49 except that $t \to \Delta t$. Therefore, by measuring the decay rate as a function of the time between the decays of the $B\overline{B}$ pair, the parameter $\sin(2\beta+\gamma)$ can be measured.

Chapter 3

BABAR and PEP-II

> "'I'm a computer with an IQ of twelve thousand, three hundred and sixty-eight. You, of all the intelligences in the universe - a lowly, plastic Toaster, with a retail value of $£19.99 plus tax - you alone have the opportunity to have any question answered. You could for instance, ask me the secret of Time Travel. You could ask me: is there a God, and what is His address? You don't seem to understand: I know everything, and I want to share it with you.'
> 'That's not answering my question,' said the Toaster.
> 'No, I would not like a crumpet. Ask me a sensible question. Preferably one that isn't bread-related.' "
>
> Better Than Life, Grant Naylor.

The *BABAR* experiment is located at the Stanford Linear Accelerator Center (SLAC) in California, USA. Figure 3.1 is an aerial picture of the SLAC site.

In order to study $CP-$violation in the B meson system, it is necessary to measure the time dependent decay rates of B mesons. B mesons are produced by colliding electrons with positrons at a centre of mass (CM) energy equal to the mass of the $\Upsilon(4S)$ resonance. The $\Upsilon(4S)$ then decays to a $B\overline{B}$ pair. The boost of the $\Upsilon(4S)$ needs to be large enough so that silicon strip devices are able to measure the separation between the decay vertices of the B mesons. This is achieved by having different energies for the electron and positron beams. The linear accelerator at SLAC is used to produce electron bunches of 9 GeV and positron bunches of 3.1 GeV. These are then injected into the PEP-II storage rings. The asymmetric energies of the electron and positron beams give the CM a boost of $\beta\gamma = 0.56$, which means the separation of the B decay vertices is of the order of a few hundred micrometers. The design

Figure 3.1: Aerial photograph of the Stanford Linear Accelerator Centre (SLAC) indicating the linear accelerator (linac) and the *BABAR* experiment hall [12].

luminosity of PEP-II is high, 3×10^{33} cm^{-2}s^{-1} and allows the study of the decay modes of B mesons that have small branching fractions. The following sections describe how PEP-II produces B mesons, how their decay products are detected by the different components of the *BABAR* detector and how the data obtained are used to study the decay products of the collisions.

3.1 PEP-II

A 2 mile long, linear accelerator (linac) is used to produce and accelerate electrons and positrons which are then injected into the PEP-II storage rings. The electron and positron bunches then circulate, in opposite directions, in separate vacuum pipes that have a circumference of 2.2 km. The beams are then tuned and collided where the *BABAR* experiment is located. A more detailed description of PEP-II can be found in [13]

Figure 3.2 illustrates the main components of the accelerator and storage rings. An electron gun produces electrons by passing an electrical current through a filament. The electrons are pulled out of the filament by an electric field and are bunched and then accelerated by a series of klystrons that power copper cavities.

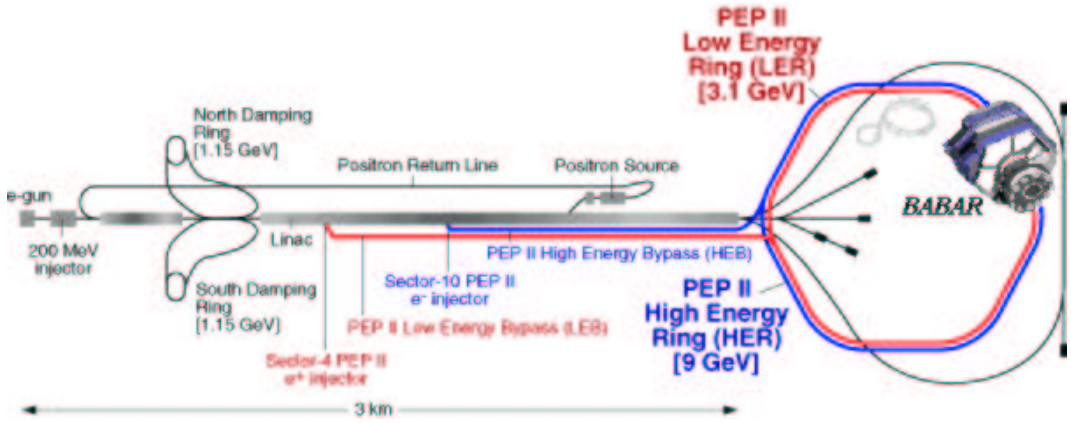

Figure 3.2: Diagram illustrating the components of the linear accelerator and the PEP-II storage rings [14].

The klystrons produce microwaves (with a frequency of 2856 MHz) that are transmitted through wave guides to the accelerating structure made up of a series of cavities; see Fig. 3.3. This creates, in the cavity, an oscillating electric field in the direction of the accelerator and an oscillating magnetic field in a circle around the accelerator pipe. The oscillating field is synchronised with the arrival of a bunch of electrons or positrons to provide optimal acceleration.

Positrons are produced by taking some of the electrons from the accelerator and colliding them with a tungsten target. This produces a large number of electron-positron pairs. The positrons are collected and then sent to the beginning of the accelerator.

The transverse size of the electron and positron bunches tends to increase as the electrons and positrons are accelerated. This is undesirable as this would decrease the luminosity of the beam. To minimise the effect of this, the electron and positron bunches are diverted into a pair of storage rings, which are used to dampen them. The bunches circulating in the damping rings loose energy due to synchrotron radiation. The bunches are then accelerated again but since the acceleration is in the direction parallel to the accelerator and the bunches emit synchrotron radiation in all directions, the transverse size of the bunch decreases. The bunches are then returned to the accelerator, after they have been damped, where the positron bunches are accelerated to 3.1 GeV and the electron bunches are accelerated to 9 GeV. The positron and electron bunches are then injected into the low energy ring (LER) and high energy (HER) ring of PEP-II, respectively, until the beams circulating in

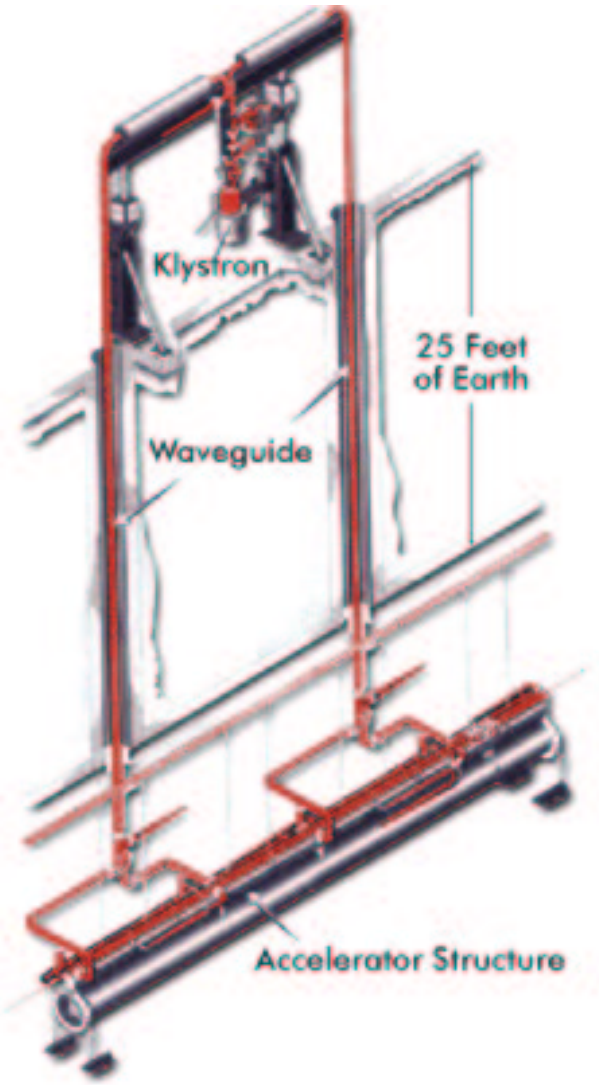

Figure 3.3: Illustration of the waveguides that transmit the microwaves, produced by the klystrons, to the copper cavities [14].

PEP-II have reached the desired currents. The spacing between bunches is typically $6-10$ ns. The time it takes to fill the LER and HER beams from scratch is approximately $10-15$ minutes with a typical beam current circulating in the LER of 1.3 A and 0.7 A in the HER. PEP-II normally operates on a $40-50$ minute fill cycle and replenishing the beams between cycles normally takes about 3 minutes.

As the beams circulate in PEP-II, they are tuned to give a small beamspot. The bending of the beams causes energy loss due to synchrotron radiation. This is compensated for by using room-temperature radio frequency (476 MHz) cavities to accelerate the beam. To achieve the strong focusing and beam separation needed, magnets are placed close to the interaction region. Figure 3.4 is a plan view of the interaction region illustrating the direction of the beams and the location of the magnets. The z-axis is along the axis of the detector and is almost parallel to the e^- beam direction. The x-axis is perpendicular to the z-axis and points away from the centre of PEP-II with the xz plane containing the e^+e^- beams. The y-axis is perpendicular to both the x and z axes and points up. The bunches collide head on and are horizontally separated by the dipole magnets (B1) followed by a series of offset quadrupoles (Qi). The B1 and Q1 magnets are located within the solenoid field of the *BABAR* detector (as in Fig. 3.5) and the others are located at the edges of the solenoid field. The B1 and Q1 magnets are permanent magnets made of samarium-cobalt, since they need to operate within the solenoid field, whereas the other magnets are made of iron. The z-axis of the *BABAR* detector is offset from the collision axis by about 20 mrad, in the horizontal (xz) plane, to minimise the perturbation of the beams due to the solenoid field.

For the data used in the branching fraction and B lifetime studies, PEP-II was typically operating with $550-830$ bunches with a transverse rms beam size of 120 μm in the x direction and 5.6 μm in the y direction. This provided an average luminosity of 2.5×10^{33} cm^{-2}s^{-1}. PEP-II has since then achieved a peak luminosity of 4.21×10^{33} cm^{-2}s^{-1} which exceeds its design luminosity.

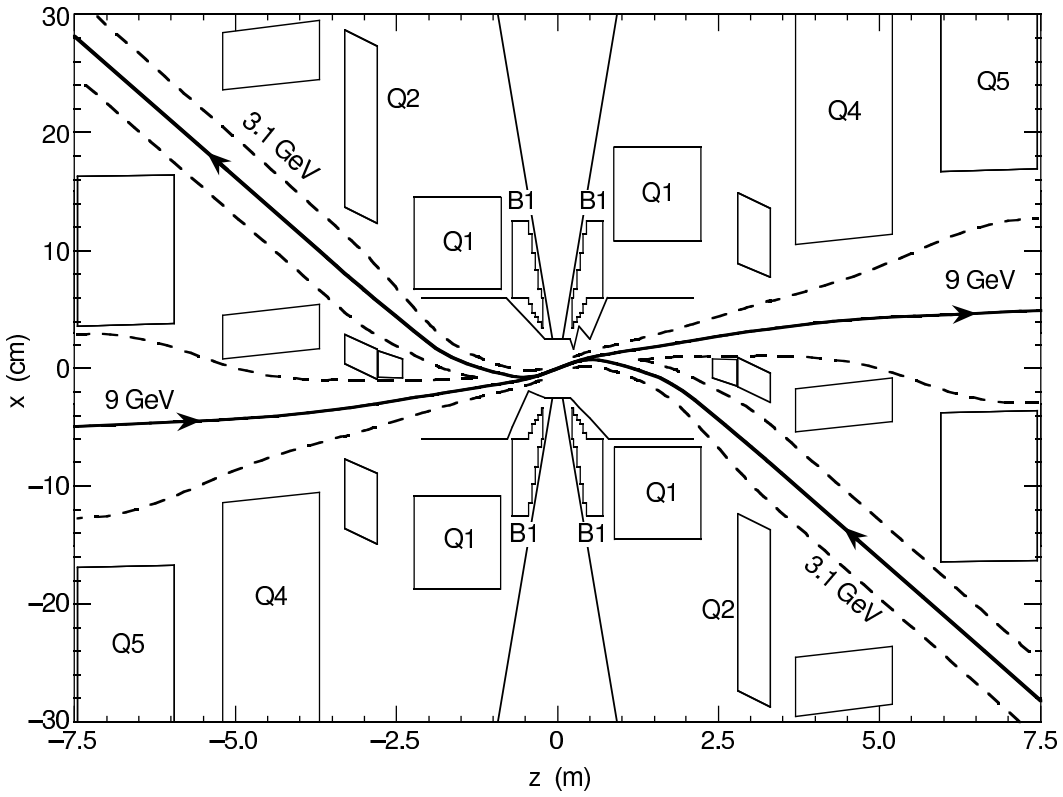

Figure 3.4: Diagram illustrating the beam direction and location of the magnets close to the interaction region [15].

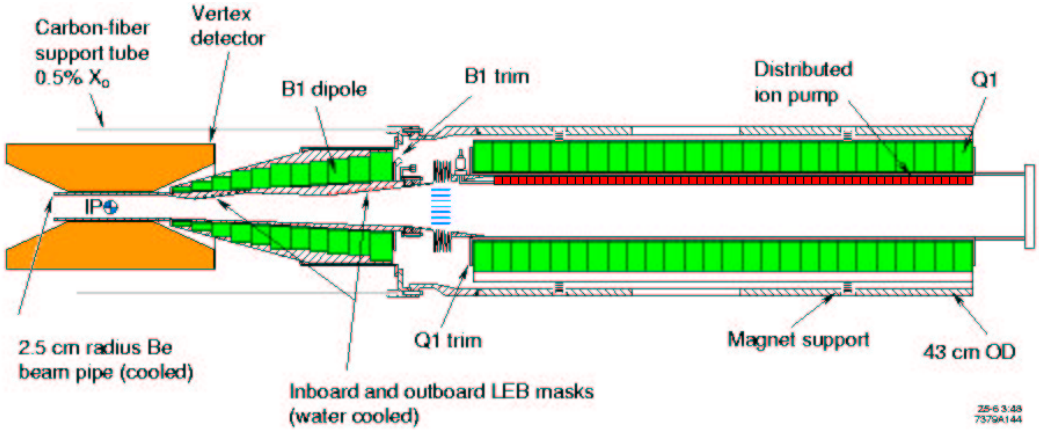

Figure 3.5: Diagram showing the location of the B1 and Q1 permanent magnets. The B1 dipole magnet is placed right up to the vertex detector [15].

3.2 The *BABAR* Detector

The main aim of the *BABAR* experiment is to study the decays of $B\overline{B}$ mesons ($B\overline{B}$ sounds similar to Babar, the fictional character, hence the name). A more detailed description of the *BABAR* detector can be found in [16]. Some of the important requirements of the detector are:

- A large and uniform acceptance down to small polar angles with respect to the direction of the boost.
- High reconstruction efficiency for charged particles with momenta down to 60 MeV/c and for photons with an energy down to 20 MeV.
- Very good momentum resolution for charged tracks and excellent energy and angular resolution for photons.
- Very good vertex resolution, both transverse and parallel to the beam direction.
- Efficient and accurate identification of hadrons and leptons over a wide range of momenta.

The *BABAR* detector consists of different sub-detector systems arranged concentrically around the beam pipe; see Fig. 3.6. Each sub-detector system is designed to measure different properties of the particles (e.g. energy and momentum) to satisfy the requirements listed above. The following sections describe each of the subdetector components and the way in which the data from them are used to perform analyses.

3.2.1 The Silicon Vertex Tracker

The Silicon Vertex Tracker (SVT); see Fig. 3.7, is used to determine the decay vertices of particles, which is necessary to study $CP-$violation. The SVT is made of strips of double-sided silicon that are arranged in five concentric cylindrical layers. A charged particle passing through the SVT will create a signal in each silicon strip that it passes through, allowing its trajectory to be measured. The strips are arranged perpendicular and parallel to the beam axis which means the trajectory in 3D is

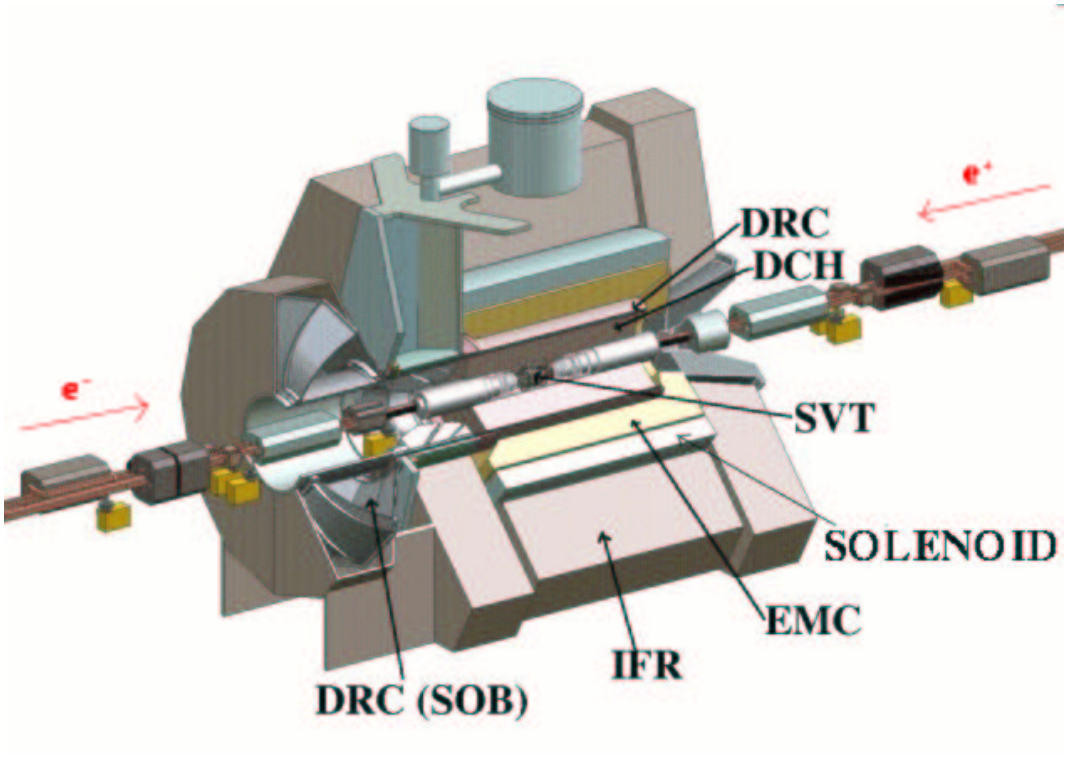

Figure 3.6: Cut-away diagram of the *BABAR* detector. The components labelled are: the silicon vertex tracker (SVT), the drift chamber (DCH), the detector of internally reflected Cherenkov radiation (DRC), the DRC standoff box (SOB), the electromagnetic calorimeter (EMC), the solenoid and the instrumented flux return (IFR) [12].

determined. Figure 3.8 is a schematic diagram of the SVT showing the arrangement of the strips and its dimensions. In addition to measuring the trajectory of the particle, the rate of ionisation, dE/dx, is also measured and is used for particle identification. Figure 3.9 shows dE/dx as a function of momentum for different particles.

3.2.2 The Drift Chamber

The Drift Chamber (DCH), see Fig. 3.10, is the main tracking device and is used to measure the momentum of charged particles. This is done by measuring the curvature of their trajectories in the constant magnetic field of 1.5T produced by the solenoid. The DCH is made up of 40 layers of wires that run parallel to the beam axis in a chamber filled with Helium-isobutane (80%-20%) gas. As the charged particle passes through the chamber it causes ionisation in the gas which is collected by the wires. This allows the trajectory of the track, in the plane perpendicular to the

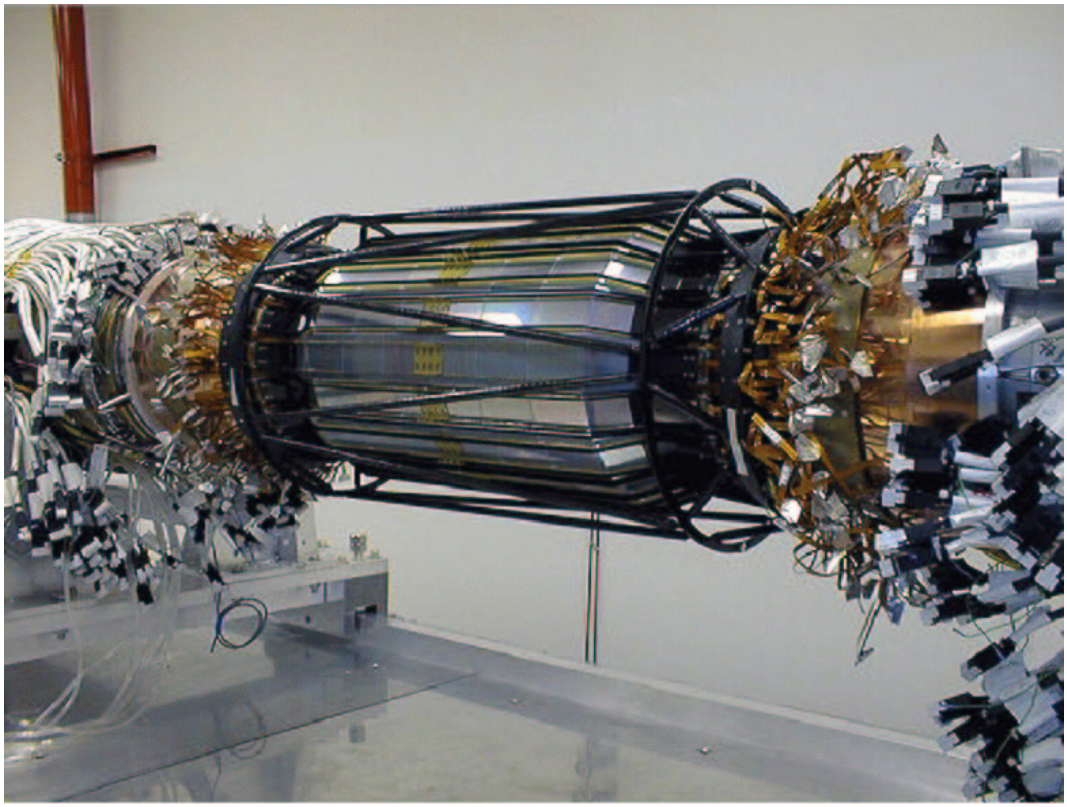

Figure 3.7: Photograph of the SVT showing the outer layer of silicon strips, the support structure and the readout wires [12].

beam direction and the rate of ionisation, dE/dx, to be measured. Figure 3.11 shows dE/dx as a function of momentum for different particles.

3.2.3 The Detector of Internally Reflected Cherenkov Light

The Detector of Internally Reflected Cherenkov light (DRC) is mainly used for particle identification. The DRC consists of 144 synthetic fused silica bars arranged in a 12-sided polygonal barrel; see Fig 3.12. The backward-facing ends of the bars enter a container, called the Standoff Box (SOB), of purified water. The far end of the SOB is instrumented with photomultiplier tubes (PMTs). A charged particle passing through a material will create a cone of Cherenkov light if its speed exceeds the speed of light in that material, i.e. if

$$\beta > \frac{1}{n}, \tag{3.1}$$

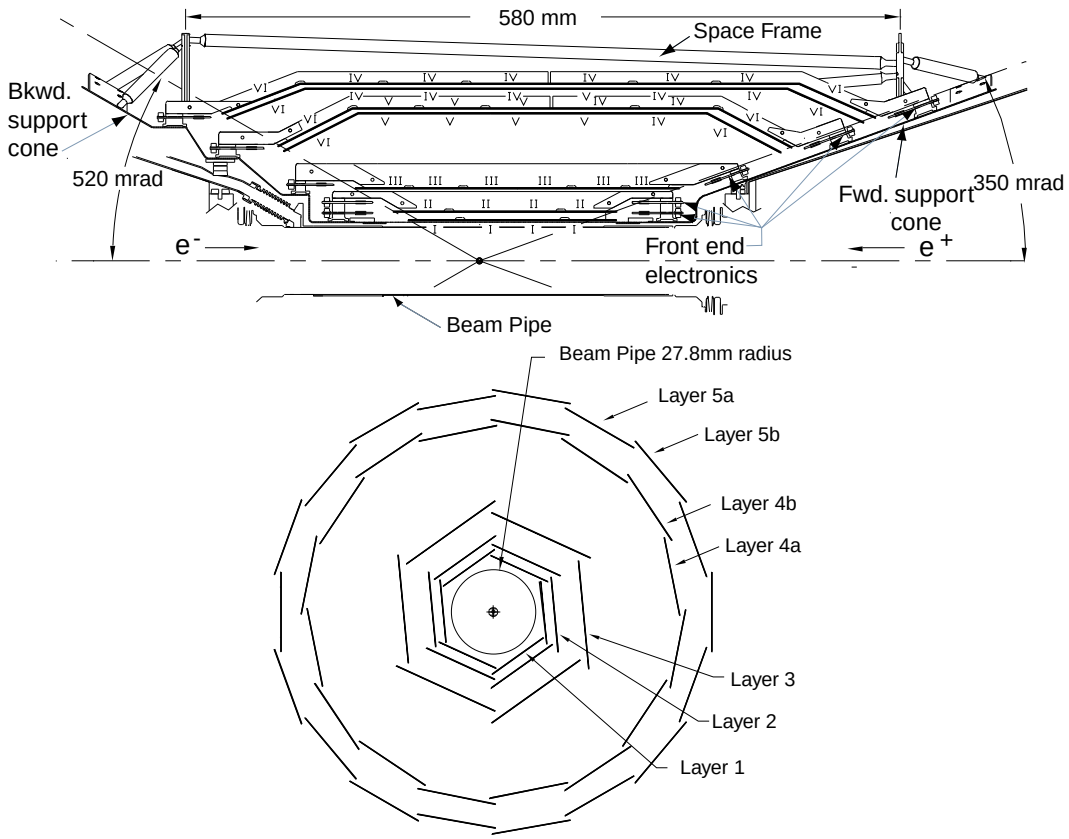

Figure 3.8: Diagram of the SVT showing the arrangement of the layers. The coverage of the SVT is limited by the need to accommodate the beam dipole magnets [16].

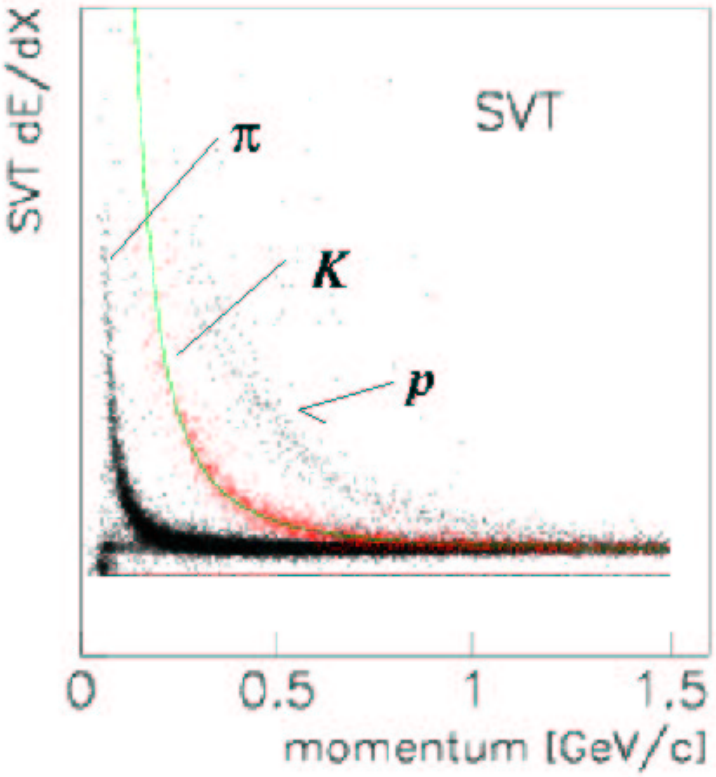

Figure 3.9: Monte Carlo data scatter plot of dE/dx in the SVT versus momentum for pions, kaons and protons. The green line through the kaon band is the fitted pdf, used for particle identification; see Sec. 3.3.3.

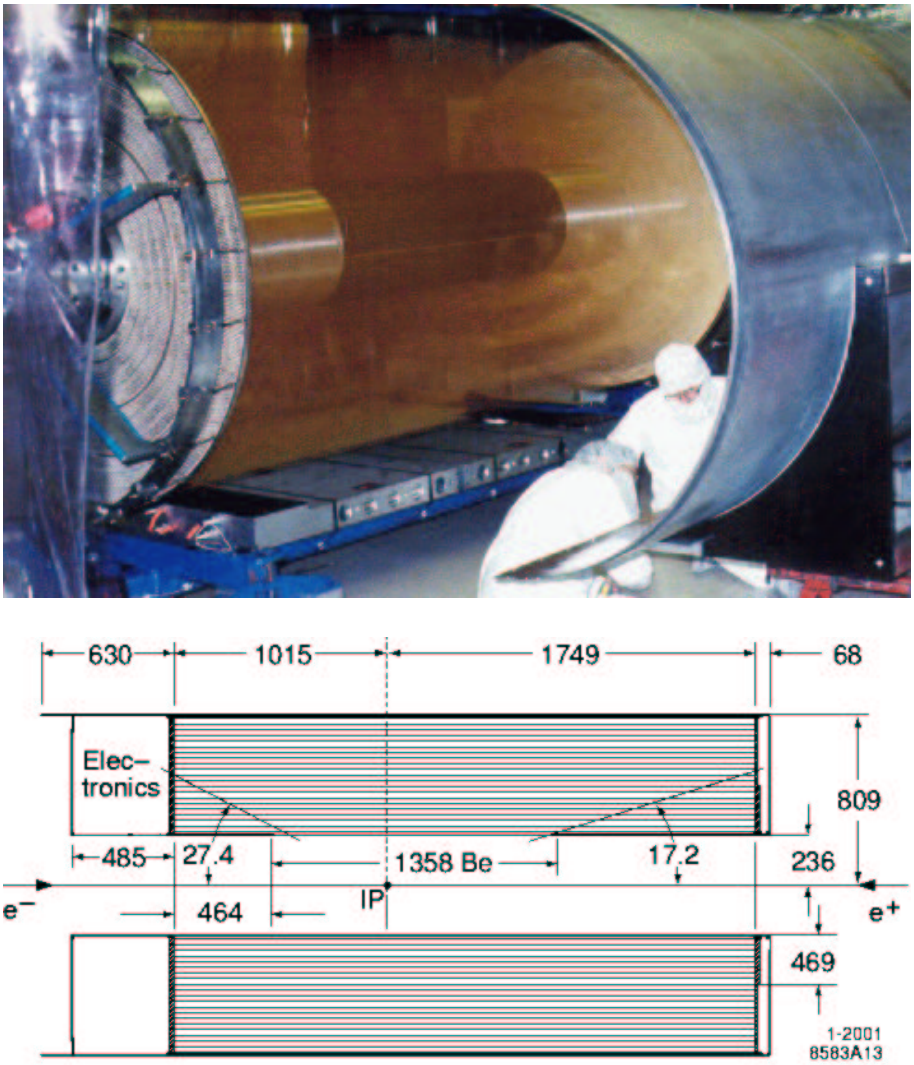

Figure 3.10: Photograph of the DCH during the installation of the outer wall and a diagram showing the dimensions of the DCH and showing the position of the beryllium (Be) inner wall [12][16].

where β is the speed of the particle given by the ratio of its momentum and energy (p/E) and n is the refractive index of the material. For the silica bars used in the DRC, $n = 1.473$. The Cherenkov light (which has an average wavelength $\lambda \approx 440\,\text{nm}$) is emitted at an angle, with respect to the track, given by

$$\cos\theta_c = \frac{1}{n\beta}. \tag{3.2}$$

In the DRC, the cone of Cherenkov light travels along the length of the silica bar toward the SOB by a series of total internal reflections that preserve the shape of the cone. When the cone reaches the SOB it expands and is projected against the

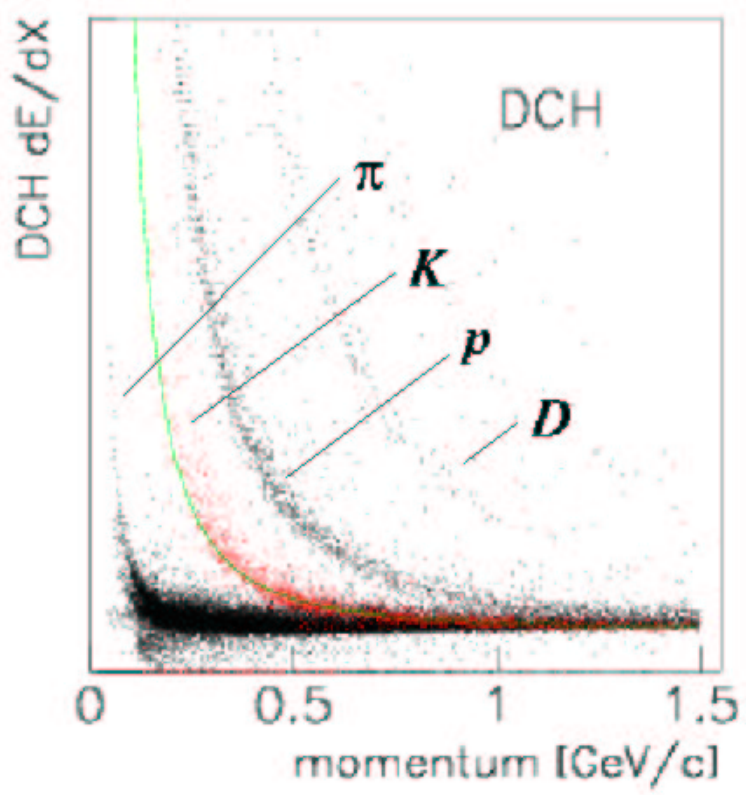

Figure 3.11: Monte Carlo data scatter plot of dE/dx in the DCH versus momentum for pions, kaons, protons and deuterons. The green line through the kaon band is the fitted pdf, used for particle identification; see Sec. 3.3.3.

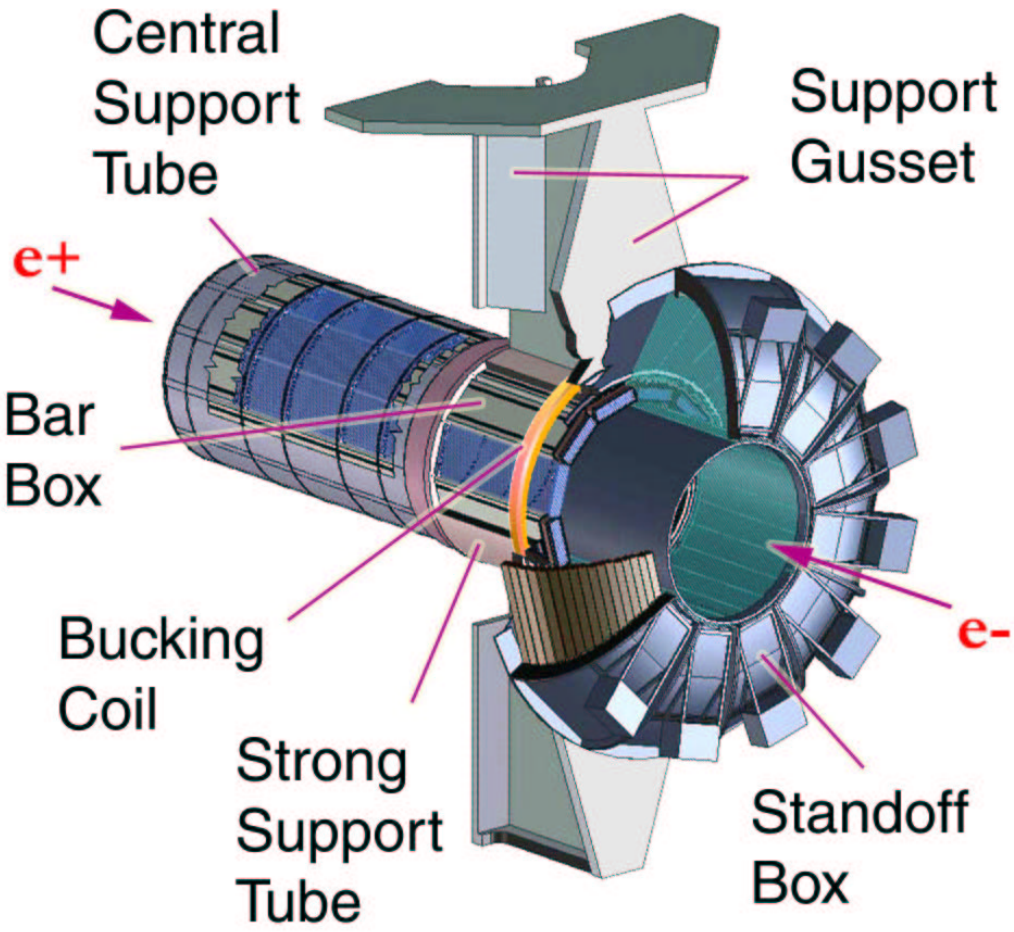

Figure 3.12: Diagram of the DRC showing the arrangement of the twelve bar boxes (which contain the silica bars) and the standoff box that contains the photomultiplier tubes used to detect the Cherenkov light [12].

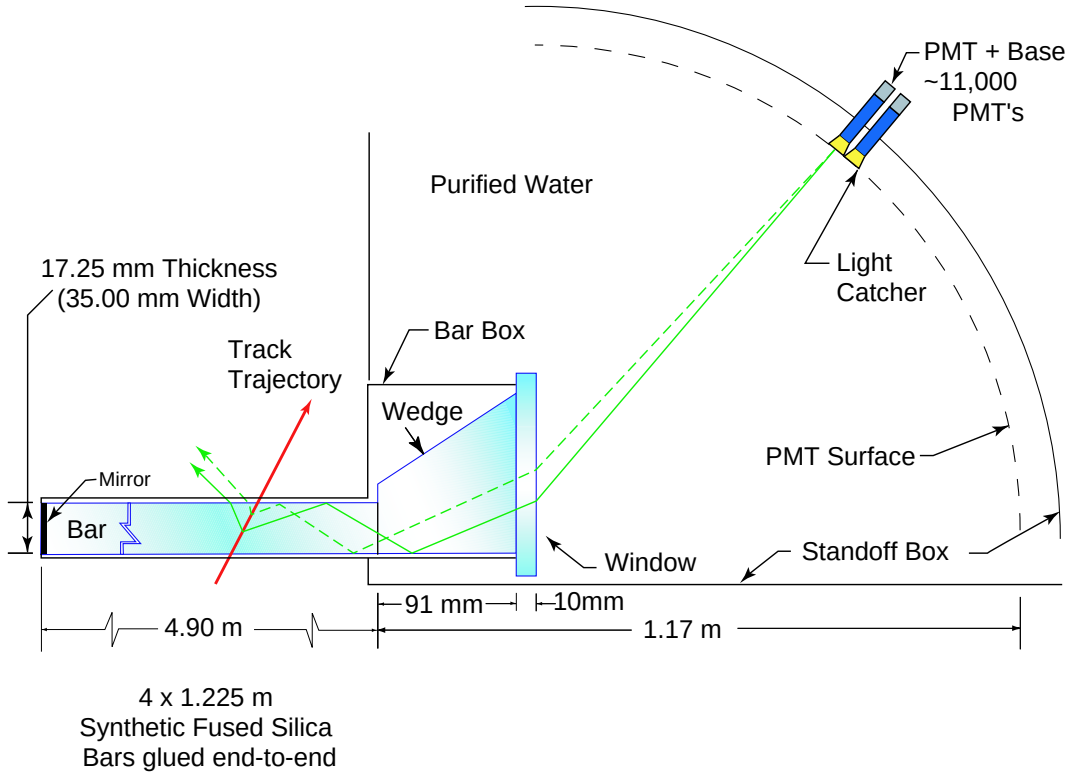

Figure 3.13: Diagram showing how the DRC works. An incoming charged particle (the red line) produces Cherenkov light (the green lines) which travels to the standoff box by a series of total internal reflections. The Cherenkov light emerges at the end in the standoff box, travels through the purified water and is detected by the photomultiplier tubes (PMT's). The series of total internal reflections preserves the angle at which the Cherenkov light is emitted and this produces a circle (or arc) on the surface of the standoff box, the size of which depends on the angle at which the Cherenkov light is emitted [12].

face instrumented with PMTs; see Fig. 3.13.

The PMTs are used to measure the angle subtended by the cone, from which the particle's speed is determined using Eq. 3.2. Thus, knowing the particle's speed and momentum, its mass can be determined. Figure 3.14 shows the distribution of θ_c as a function of momentum for different types of particle.

3.2.4 The Electromagnetic Calorimeter

The Electromagnetic Calorimeter (EMC) is used to measure the energy of particles. The EMC consists of 5760 thallium doped caesium iodide crystals arranged in a cylindrical barrel and 820 crystals arranged in a conical end-cap; see Fig. 3.15. Each crystal is instrumented with a photodiode read-out. An incoming particle deposits energy in a crystal which initiates a shower of particles. The shower is eventually

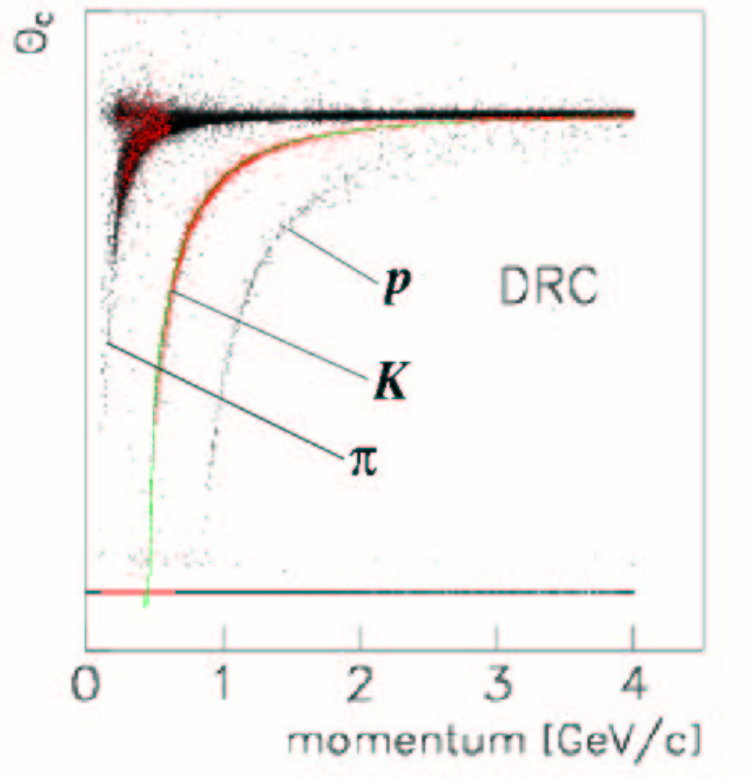

Figure 3.14: Scatter plot of θ_c versus momentum for different particle types.

absorbed and causes the crystal to scintillate. The amount of scintillation light produced is proportional to the energy deposited in the crystal. A particle typically deposits its energy in a number of adjacent crystals and creates what is called a cluster of energy deposits. Clusters are required to have at least one crystal with a deposit of at least 10 MeV and adjacent crystals are included if they have deposits > 1 MeV or if they are neighbours of a crystal with a deposit of 3 MeV or more. The total energy deposited in a cluster is required to be > 20 MeV. The position of a cluster, i.e. the cluster's centroid, is determined using a logarithmic centre-of-gravity method. It is possible for more than one particle to create clusters that appear as one merged cluster, e.g. the decay of a fast π^0 to two photons. In this case it is necessary to split the cluster to identify the energy deposits from the two particles. The EMC is vital for neutral particle detection and is used for identification of charged particles. The trajectories of charged particles are projected through to the face of the EMC and are compared to clusters that originate from that region. The track impact point and the cluster centroid are calculated and if they are consistent with each other, the track is associated with that cluster.

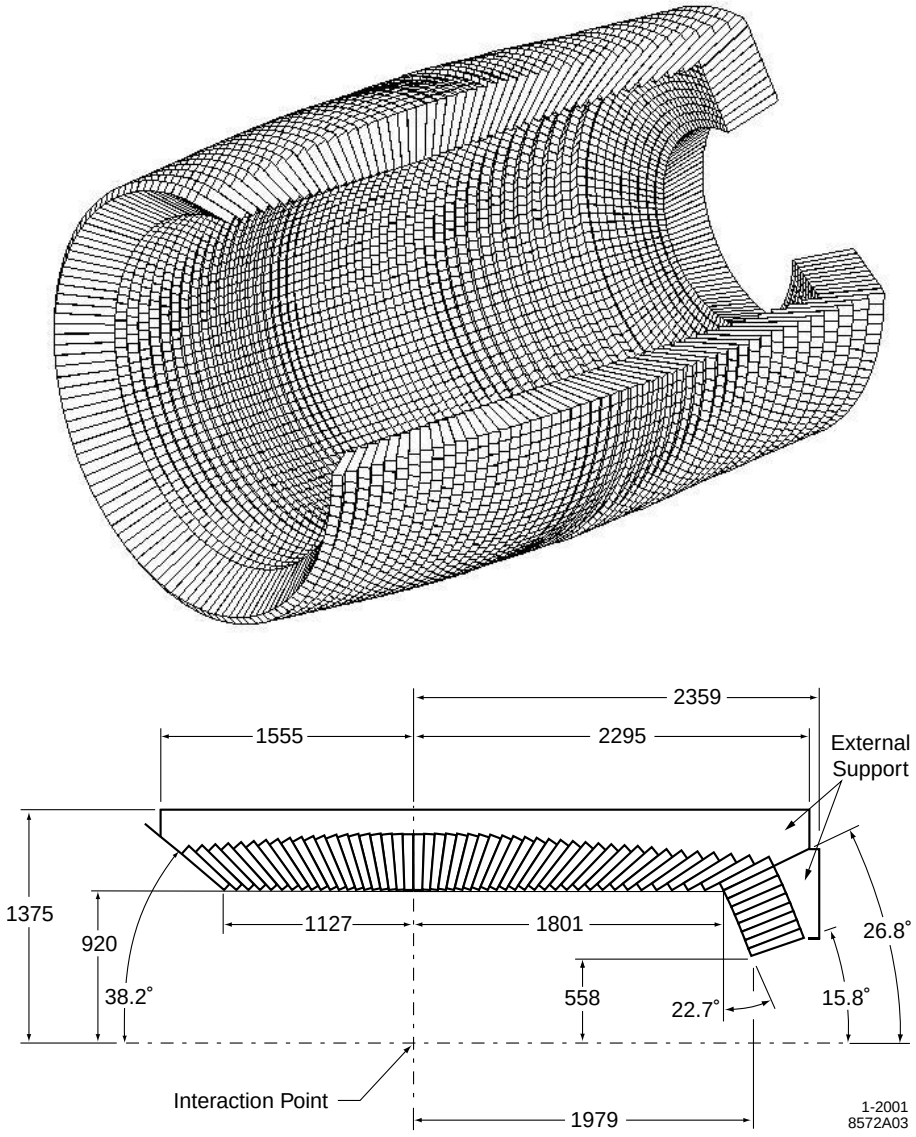

Figure 3.15: Diagram of the EMC showing the arrangement of the crystals [16].

The shapes of clusters give information on the identity of the particle that deposited the energy, since the longitudinal and lateral energy distributions are different for electromagnetic and hadronic showers. Electromagnetic showers tend to deposit their energy in one or two crystals whereas hadronic showers have a broader lateral energy distribution. Two lateral shower shape variables are used for particle identification:

- Lateral energy distribution, LAT, first introduced by the ARGUS experiment [17], is given by

$$LAT = \frac{\sum_{i=3}^{N} E_i r_i^2}{E_1 r_0^2 + E_2 r_0^2 + \sum_{i=3}^{N} E_i r_i^2}, \tag{3.3}$$

  where N is the number of crystals in the cluster, E_i is the energy of crystal i and $E_1 \geq E_2 \geq ... \geq E_N$, $r_0 = 5\,\text{cm}$ is the average distance between the front faces of two adjacent crystals and r_i is the distance between crystal i and the centre of the shower (calculated using the centre-of-gravity method but with linear energy-weighting of each crystal).

- The modulus of the (4,2) order Zernike moment, $|A_{42}|$, first used by the ZEUS experiment [18] gives a measure of the oblateness of the cluster. The (n,m) order Zernike moment is given by

$$A_{nm} = \sum_{\substack{i=1 \\ r_i \leq R_0}}^{N} \frac{E_i}{E} \cdot f_{nm}\left(\frac{r_i}{R_0}\right) \cdot e^{-im\phi_i}, \tag{3.4}$$

  where $R_0 = 15\,\text{cm}$, E_i, N and r_i are the same as for LAT, E is the total energy of the cluster, ϕ_i is the phi position of crystal i and

$$f_{nm}\left(\rho_i \equiv \frac{r_i}{R_0}\right) = \sum_{s=0}^{(n-m)/2} \frac{(-1)^s\,(n-s)!\rho_i^{n-2s}}{s!\left(\frac{n+m}{2}-s\right)!\left(\frac{n-m}{2}-s\right)!}. \tag{3.5}$$

3.2.5 The Instrumented Flux Return

The Instrumented Flux Return (IFR) is mainly used for muon identification and the detection of neutral hadrons, which are primarily K_{L} mesons. The steel bulk of the IFR is used as the flux return for the solenoid. The steel is segmented and instrumented with Resistive Plate Chambers (RPCs); see Fig. 3.16. The IFR is

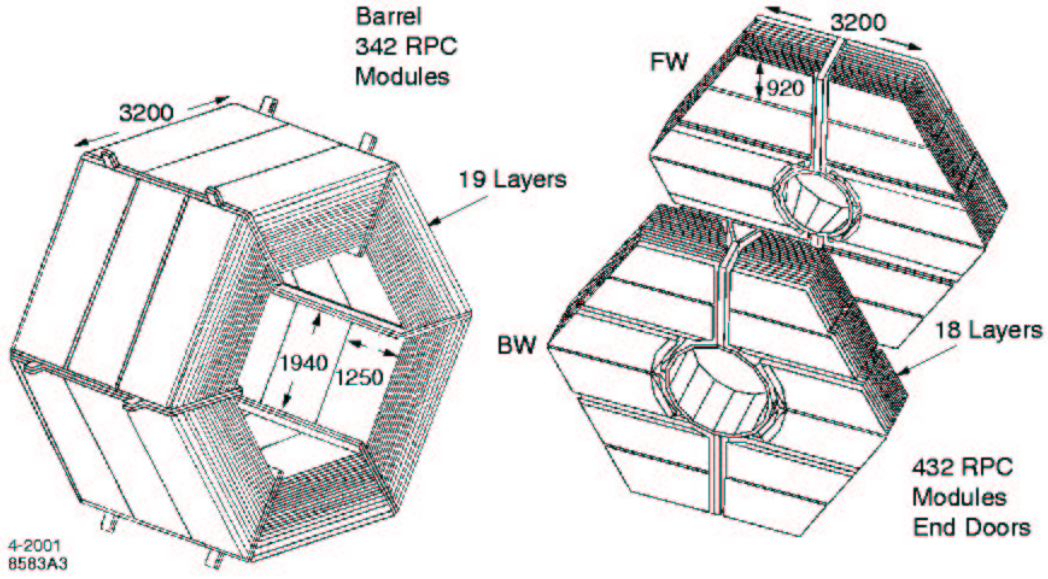

Figure 3.16: Diagram of the IFR illustrating the segmentation of the steel flux return [16].

composed of three main sections; a hexagonal barrel section and two end sections which are the forward and backward end doors. The barrel section is divided into six sectors, which are composed of 19 layers. Each of these layers is divided into three modules. Each module, which contains an RPC, has 32 readout strips to measure the z position and 96 readout strips, which extend over three modules, to measure the position in ϕ. An RPC, as illustrated in Fig. 3.17, is composed of two bakelite sheets separated by a 2 mm gap, which is filled with a mixture of Argon, Freon ($C_2H_2F_4$) and a few percent of isobutane gas. The external surfaces of the bakelite are coated with graphite. One is connected to high voltage (8 kV) and the other is connected to ground. The graphite coating is protected by an insulating mylar film on top of which are the aluminium readout strips. As a particle passes through the IFR it undergoes nuclear interactions in the steel of the magnetic yoke. Products from these interactions cause ionisation within the active region of the RPC, which produces sparks that are detected by the readout strips.

Two additional layers of cylindrical RPCs are placed between the EMC and the solenoid, to detect particles leaving the EMC. The cylindrical RPCs are based on the same concept described above but differ in their construction and organisation of readout strips.

By looking at the signals generated throughout the segments of the IFR, it is

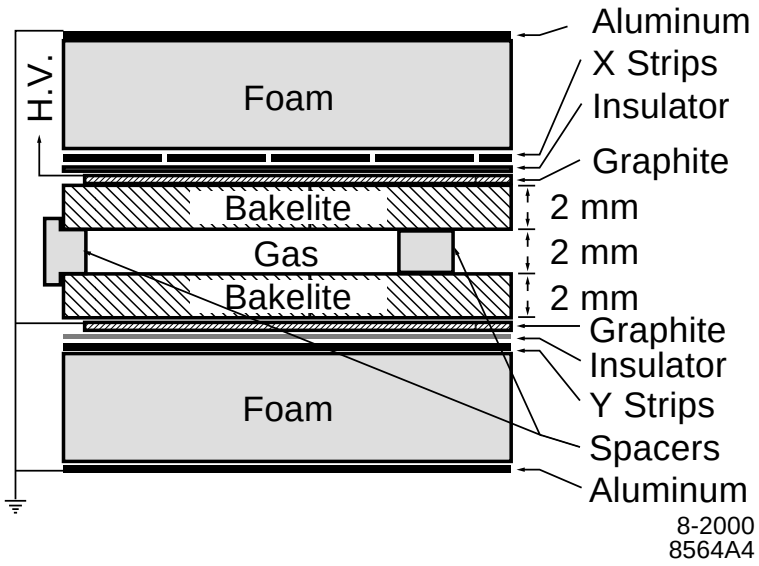

Figure 3.17: Cross section of an RPC [16].

possible to determine if the particle was a muon or a hadron.

3.2.6 The Trigger and Data Acquisition System

The design luminosity of the PEP-II collider is 3×10^{33} events $\mathrm{cm}^{-2}\mathrm{s}^{-1}$ which produces of the order of 100 useful events per second. The high beam currents required to deliver such a high luminosity also produce a large number of background interactions that will not contain any useful physics. It is therefore necessary to select events that contain useful physics and this is the job of the trigger system.

The trigger system has two levels of filtering, the Level-1 and Level-3 trigger systems. The Level-1 trigger processing is done by custom built electronics that use information from the DCH, EMC and IFR to create fundamental objects, e.g. the sum of energy deposits in a section of the calorimeter. These objects are then passed to the Global Trigger (GLT) electronics, which makes a decision whether to keep the event or not. Since these objects require little processing time to construct, trigger decisions can be made at a high enough rate to match the luminosity of PEP-II. The author was involved in maintaining the electromagnetic calorimeter trigger (EMT), which is part of the Level-1 trigger system. The main function of the EMT is to condense information from the EMC and to package it in a form which allows the GLT to make trigger decisions. Data from the EMC crystals are grouped into towers

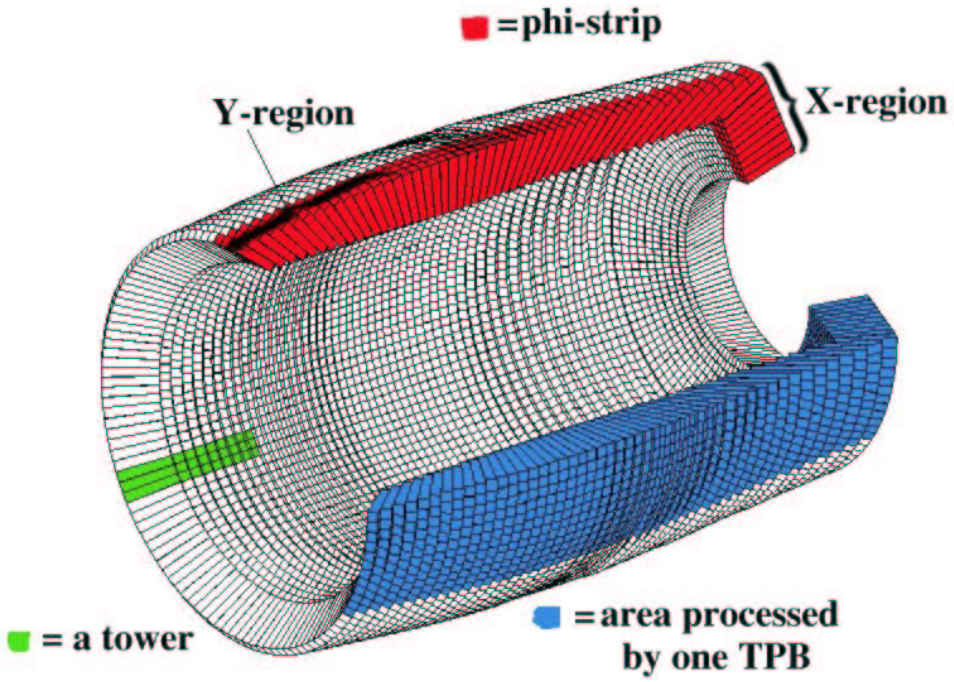

Figure 3.18: Diagram of the EMC showing crystal and tower groupings.

that are 8 crystals in θ and 3 in ϕ; see Fig 3.18.

Thus the EMC consists of 40 towers in ϕ and 7 towers in θ. The energy deposited in each crystal in a tower is summed to form a tower-sum. A minimum deposit of 20 MeV per crystal is required before the crystal is included in the tower sum. These tower sums are then sent continuously to the EMT by the EMC Untriggered Personality Cards (UPCs). The main components of the EMT are 10 Trigger Processor Boards (TPBs) and a Transition Board. The Transition Board is used to control the TPBs. The TPBs process the tower sums and pass their results to the global trigger (GLT). Figure 3.19 illustrates the flow of data from the EMC crystals to the GLT.

Each TPB processes data from four towers in ϕ and all seven towers in θ. The tower sums for a particular ϕ are then summed over θ to form 40 phi strips. Each phi strip is then summed with its nearest neighbour, i.e. phi strip 0 is summed with phi strip 1, phi strip 1 is summed with strip 2 ... and strip 39 is summed with strip 0 to give 40 nearest neighbour summed phi strips. As well as summing over all θ two other phi strips are considered; the sum of the last two barrel towers (i.e. theta=5, 6) and the forward endcap (i.e. theta=0). The energy deposited in each of the three phi strip regions ϕ, Y and X, i.e. all theta, theta=5,6 and theta=0 respectively, are then compared to five different thresholds. The phi strips in the ϕ region are

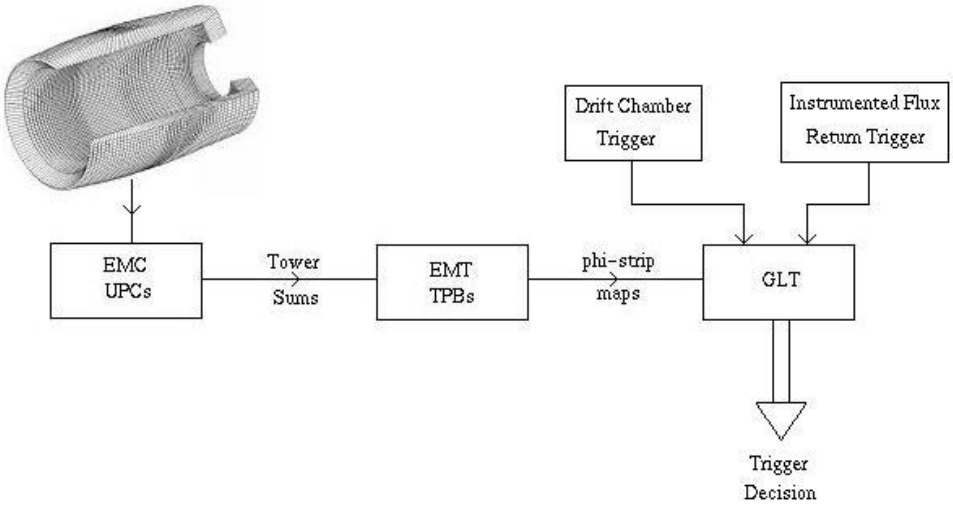

Figure 3.19: Schematic diagram of the flow of data from the EMC crystals to the GLT.

compared against 3 thresholds whereas the phi strips in the X and Y regions are compared to one threshold each. A map is created that indicates the phi strips that exceed the different thresholds. This information is sent to the GLT, which uses it to make a trigger decision.

An event passing the Level-1 trigger is then processed by the Level-3 trigger, which is done purely by software. The Level-3 trigger selection reduces the data rate from around 800 Hz to 100 Hz. After an event is accepted by the Level-3 trigger system it is processed by the Online Event Processing (OEP) software, where some basic event identification is done, e.g. identifying bhabha or hadronic events. Events are then processed by the offline reconstruction code, which is used to construct the basic quantities (eg lists of tracks, clusters, etc.) used in analyses. The following section describes how the important quantities used in the branching fraction and B lifetime studies are determined.

3.3 Basic Reconstruction and Particle Identification

This section describes how the raw data obtained by the various subdetector systems, described in the previous section, are used to reconstruct particles. The basic objects used in the analyses are tracks and clusters. A track is the trail of hits made by a

charged particle that traverses the SVT and DCH. A cluster is an isolated deposit of energy within the EMC. Information from the DRC and IFR is also used to provide discrimination between electrons, muons, pions and kaons.

The following sections describe how tracks, clusters and particle identification information are used in the reconstruction code.

3.3.1 Reconstruction of Charged Tracks

Helical tracks are first separately identified in the SVT and the DCH. These are then projected up to the support tube of the SVT and matching tracks are combined. The combined track is then refitted to a helix by an algorithm that takes into account multiple scattering and energy loss effects. The result of this fit gives the momentum of the particle. Certain quality requirements are made of the reconstructed tracks before they are made available as a list for use in an analysis. All the tracks used in the branching fraction and B lifetime analyses have the following quality requirements:

- Momentum $\leq 10\,\mathrm{GeV}$.
- Distance of closest approach in the plane perpendicular to the beam direction $\leq 1.5\,\mathrm{cm}$.
- Distance from the beam spot, along the beam direction, $\leq 10\,\mathrm{cm}$.

3.3.2 Reconstruction of π^0 mesons

Clusters, as described in Sec. 3.2.4, are combined to form π^0 candidates. There are two basic types of π^0 mesons; one where the two photons create two distinct clusters in the EMC and the other case is where the two photons form a merged cluster. In the latter case the π^0 is referred to as a merged π^0. Merged π^0 mesons can be classified into two groups where either the merged cluster has one or two maxima. Both types of merged π^0 mesons and unmerged π^0 mesons are combined together to give the list of π^0s used for the selection of $B^0 \to D^{*-}\rho^+$ events. Unmerged π^0 mesons are required to pass the following criteria

- Energy of each cluster $> 30\,\mathrm{MeV}$.

- LAT (defined in Sec. 3.2.4) of each cluster < 0.8.
- Energy of the $\pi^0 > 200\,\mathrm{MeV}$.

Merged π^0 mesons with two(one) maxima are required to have a cluster energy $> 0.9(2.1)\,\mathrm{GeV}$ and to pass the following criteria

- Track matching consistency ≤ 0.01.
- Merged π^0 consistency ≥ 0.001.
- The likelihood ratio $(\pi^0/\gamma) \geq 1$.

The track match consistency is based on a χ^2 fit of the projected track position and the position of the cluster. The merged π^0 consistency is based on the distribution of an estimator of the mass given by

$$m = E \times \sqrt{S - const}, \tag{3.6}$$

where E is the energy and S is the second moment of the cluster and the *const* variable is determined from Monte Carlo data. The variable m is calculated for five neutral particle hypotheses: merged π^0, photons, K_L, neutrons and anti-neutrons. The likelihood ratio (π^0/γ) is the ratio of the likelihood function of m for the π^0 and the photon hypotheses.

3.3.3 Particle Identification

Information from the various sub-detector systems are used to distinguish between pions, muons, electrons and kaons. The two sub-detectors whose main task it is to provide particle identification information are the DRC and the IFR. The DRC is most useful in differentiating pions from kaons in the momentum region $> 0.7\,\mathrm{GeV/c}$, where dE/dx information does not provide good separation. The IFR is mainly used to provide muon identification. Most charged particles that make it as far as the IFR are pions and muons. The dense steel absorbs a lot of energy from the pions, whereas the cross section for muons to interact with nucleons is relatively low. Thus, most of the pions get absorbed in the IFR, whereas the muons mainly pass straight through.

Many selection algorithms are used to provide either high purity or high efficiency for the selection of particles. For the branching fraction and B lifetime analyses, the high purity selection algorithms for electrons, muons and kaons are used to select pions. A track is assumed to be a pion if it does not pass any of the high purity selection criteria for electrons, muons or kaons, which are described below.

Electron Selection Criteria

The electron identification criteria are based on information from the DCH and the corresponding cluster in the EMC:

- $500 < dE/dx < 1000$ in arbitrary units where a minimum ionising particle has a dE/dx of about 450.
- $0.75 <$ Energy/momentum < 5.0.
- Number of crystals in the EMC cluster > 3.
- $0 < LAT < 0.6$.
- $-10 < |A_{42}| < 10$,

where LAT is the lateral shower shape variable and A_{42} is the Zernike moment of order(4,2), defined in Sec. 3.2.4.

Muon Selection Criteria

The muon identification is based on information from the IFR and EMC:

- $0.05 <$ Energy deposited in the EMC $< 0.4\,\mathrm{GeV}$.
- Number of layers in the IFR with deposited energy $(N_{\mathrm{L}})> 1$.
- $(\lambda_{\mathrm{e}} - \lambda_{\mathrm{m}}) < 1$.
- The χ^2 of the track (extrapolated from the DCH) matched with the track in the IFR < 5.
- The χ^2 of the fitted IFR track $/N_{\mathrm{L}} < 3$.

- $\lambda_{\rm m} > 2.2$.
- track continuity > 0.3.
- $\overline{N} = N_{\rm s}\ /\ N_{\rm L} < 8$.
- $\sigma_{\rm multi} < 4$.

Here, $N_{\rm s}$ is the total number of readout strips (described in section 3.2.5) hit, $\lambda_{\rm e}$ is the number of interaction lengths, from the interaction region, that a muon with the measured momentum and trajectory is expected to traverse and $\lambda_{\rm m}$ is the measured number of interaction lengths traversed. The track continuity is a measure of the continuity of the track through the forward part of the IFR barrel and the IFR forward door and is given by

- $N_{\rm L}/N_{\rm last} - N_{\rm first}$ if the track is detected by the inner cylindrical RPCs and
- $N_{\rm L}/N_{\rm last} - N_{\rm first} + 1$ if it is not,

where $N_{\rm last}$ and $N_{\rm first}$ are the layer numbers of the first and last layers with hits. The variable $\sigma_{\rm multi}$ is defined as

$$\sigma_{\rm multi} = \sqrt{\sum_{i=N_{\rm first}}^{N_{\rm last}} \frac{\left(N_i - \overline{N}\right)^2}{(N_{\rm L} - 1)}}, \tag{3.7}$$

where N_i is the number of readout strips hit in layer i.

Kaon Selection Criteria

The kaon selection is based on the ratios of the likelihood for three particle hypotheses; kaon, pion and proton. dE/dx information from the SVT (see Fig. 3.9) and the DCH (see Fig. 3.11) and information from the DRC is used to construct a likelihood for each of the different particle hypotheses for different momentum regions. If the momentum of the particle is less than 0.7 GeV/c then dE/dx information is used from the SVT and DCH. Information from the DRC is used if the momentum of the track is greater than 0.6 GeV/c. Thus, only information from the DRC is used to identify kaons at higher momenta. At low momenta, the triangular region in θ_c vs. momentum is excluded, i.e. region B in Fig. 3.20. This region is populated by kaons

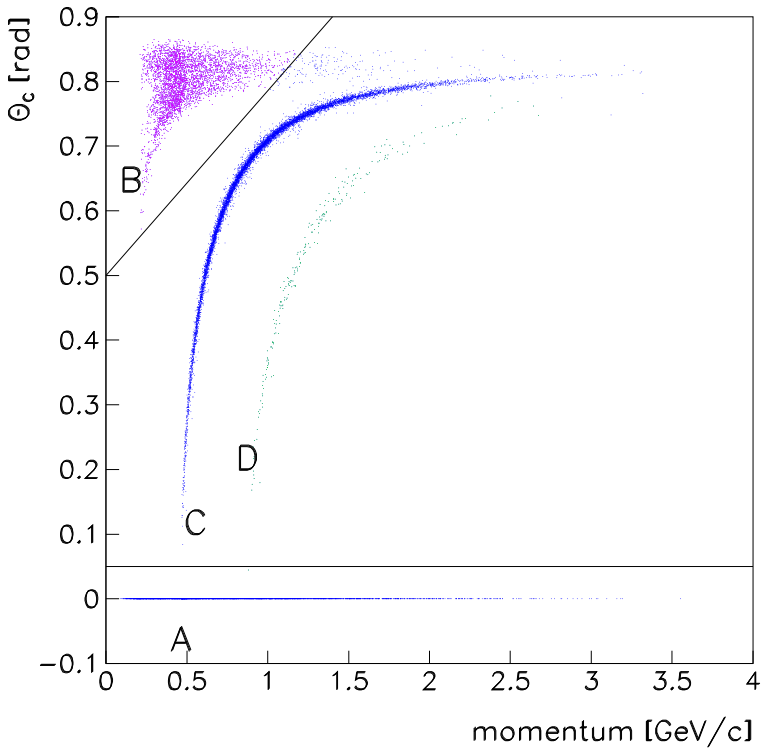

Figure 3.20: Monte Carlo data scatter plot of θ_c versus momentum for kaons. Region A is populated by kaons where no Cherenkov angle fit is performed (because either the kaon did not enter the DRC or too few Cherenkov photons were produced) or if the fit for the Cherenkov angle failed. Region B is populated by kaons where they either interacted or decayed before reaching the DRC. Region C is the band for kaons. Region D is the band for protons, which is slightly populated due to kaons that underwent hadronic interactions and released protons.

that decayed or interacted before reaching the DRC and overlaps with the electron, muon and pion band. A particle is identified as a kaon if

- $\ell_{\mathrm{K}} > w_\pi \ell_\pi$ and
- $\ell_{\mathrm{K}} > \ell_{\mathrm{p}}$,

where l_x is the likelihood for particle x and w_π is a momentum dependent weight and

- $w_\pi = 1$ for $p < 2.7\,\mathrm{GeV/c}$,
- $w_\pi = 80$ for $p > 2.7\,\mathrm{GeV/c}$ and
- $w_\pi = 15$ for $0.5 < p < 0.7\,\mathrm{GeV/c}$.

3.3.4 Data Sets

There are three basic types of data sets used in the branching fraction and B lifetime studies, on-resonance, off-resonance and Monte Carlo data. The on-resonance data sample was obtained with a CM energy of 10.58 GeV and the total integrated luminosity used was $20.07\,\mathrm{fb}^{-1}$. The off-resonance data set is obtained with a CM energy of about 10.54 GeV, which is below the $\Upsilon(4S)$ production threshold and thus this data sample does not contain any B decays. This is useful for studying processes other than B decays (i.e. $q\overline{q}$ events ,where $q = u,\ d,\ s$ and c) that exist in the on-resonance sample since it does not rely on the accuracy of the Monte Carlo simulation. The size of the off-resonance sample used was $3.07\,\mathrm{fb}^{-1}$. Throughout the branching fraction and B lifetime studies, the off-resonance sample is used to describe $q\overline{q}$ events.

The Monte Carlo data used were generated by two event generators, EvtGen [19] and JETSET [20]. EvtGen is used to generate exclusive decays of B mesons and is able to generate decays with specified Δt and angular distributions, $B^0\overline{B}^0$ mixing and $CP-$violation effects. JETSET is used to generate all other decay modes not generated by EvtGen. The simulation of the *BABAR* detector was done using GEANT3 [21]. The same reconstruction code that is used on real data is used on the simulated data after it has been processed by the detector simulation.

Chapter 4

Analysis Method

> "However, the second time round, she came upon a low curtain she had not noticed before, and behind it was a little door about fifteen inches high: she tried the little golden key in the lock, and to her great delight it fitted!"
>
> Alice's Aventures in Wonderland, Lewis Carroll.

The decay mode $B \to D^*\rho$ can be used to study $CP-$violation and, in particular, the parameter $\sin(2\beta+\gamma)$ can be measured from the time dependent decay rates. As explained in Sec. 2.3, the measured asymmetry for $B \to D^*\rho$ is expected to be small since the magnitudes of the two interfering amplitudes are very different. It is therefore necessary to obtain as many $B \to D^*\rho$ events as possible. Preliminary studies of $B^0 \to D^{*-}\pi^+$ indicated that the error on $\sin(2\beta+\gamma)$ is expected to be about twice that of the error on $\sin(2\beta)$ (measured using $B^0 \to J/\psi K^0_S$), i.e. $\sigma(\sin(2\beta+\gamma))$ is expected to be 0.22 for $30\,\mathrm{fb}^{-1}$[10]. The branching fraction for $B \to D^*\rho$ is 2.5 times that of $B^0 \to D^{*-}\pi^+$ so the naive expectation would be that the error should be $0.22/\sqrt{2.5}$. However, taking into account the π^0 efficiency and the lower purity, this may not be the case. The aim of the branching fraction and B lifetime studies is to investigate this.

If one were to fully reconstruct all of the decay products, including the decay products of the D, one could only expect to obtain about 1% of $B \to D^*\rho$ decays. However, it is possible to select $B \to D^*\rho$ events by using only the ρ and π_s and not the decay products of the D. This method, called partial reconstruction, has been successfully used in the past by the CLEO experiment to measure the $B^0 \to D^{*-}\pi^+$

branching fraction [22]. Using the partial reconstruction technique should provide a significant increase in the available statistics but with the drawback that the purity of the selection decreases significantly. Therefore, it is necessary to study this mode to see if it is possible to use the partial reconstruction method to measure $\sin(2\beta+\gamma)$ using $B \to D^*\rho$.

4.1 The Partial Reconstruction Method

Consider the decay illustrated in Fig. 4.1. Throughout the following chapters where the mode $B^0 \to D^{*-}\rho^+$ is referred to, the charge conjugate mode is also implied.

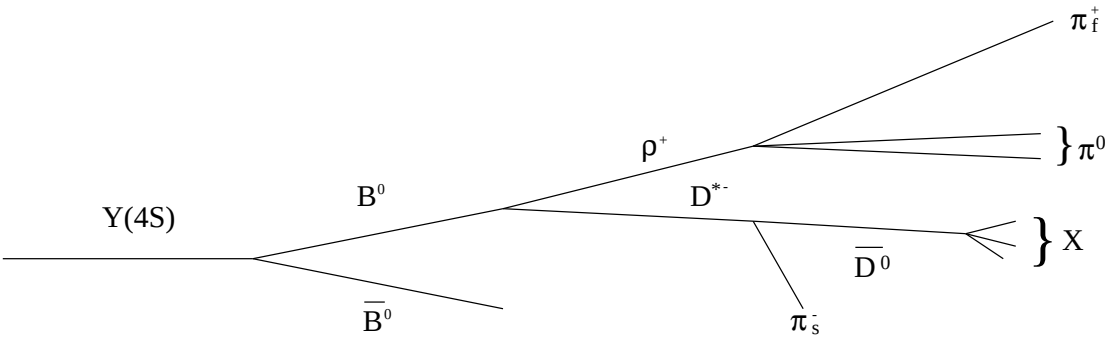

Figure 4.1: The decay chain of signal events (the charge conjugate decay chain is also considered).

The partial reconstruction method selects events of interest by using the decay kinematics and only having to reconstruct certain decay products of the B^0. For $B \to D^*\rho$, it is only necessary to reconstruct the ρ and the π_s daughter of the D^*, which is referred to as the slow pion since its momentum is low.

The main quantity used to select events is the missing mass, i.e. the invariant mass of the recoiling particles that are not reconstructed. If the reconstructed ρ and π come from a $B \to D^*\rho$ decay then the missing mass will be equal to the mass of the D. Since there is an ambiguity involved in determining the momentum of the D there is also a corresponding ambiguity in determining the missing mass. Section 5.1.3 describes how an estimator for the missing mass is constructed. The missing mass could be used to select signal events by applying a cut at $1.855\,\mathrm{GeV/c^2}$, with an efficiency of 6.5% and a purity of 24% but it would be difficult to accurately determine the number of background events in the sample due to the uncertainty

in their branching fractions. In order to model the backgrounds more accurately, the missing mass is used in an unbinned likelihood fit for the branching fraction and B lifetime measurements. The $m_{\rm miss}$ range considered for fitting is $1.75 < m_{\rm miss} < 1.875\,{\rm GeV/c^2}$. The background modes that are treated separately are

- $B \to D^*\pi\pi^0$.
- $B \to D^* a_1$.
- $B^+ \to D_1^0\rho^+, D_1^0 \to D^{*-}\pi^+$ and the charge conjugate decay. Here D_1 includes D_1^0 and $D_1^{\prime 0}$ [23].
- $B^+ \to D_2^{*0}\rho^+$ and the charge conjugate decay.
- Other B decays.
- $q\overline{q}$ events ,where $q = u$, d, s and c.

In order to do $CP-$violation studies it is necessary to measure the separation of the two B vertices. This requires being able to identify which reconstructed tracks come from which B. If all of the decay products of the $B_{\rm CP}$ (i.e. the B that decays to $D^*\rho$) were reconstructed then it would be simple to determine the tracks that come from the $B_{\rm tag}$ (i.e. the other B produced by the Υ(4S) decay). For the partial reconstruction method this is not the case, so an assumption needs to be made to estimate which tracks come from the D decay. Section 6.1.2 describes how this is done.

4.2 Selection of Events

For real data and generic Monte Carlo (i.e $B\overline{B}$) data the selection of events is done in two stages. In the first step a very rough selection of events is made to reduce the large size of the data sample. This is done automatically as part of the standard reconstruction procedure. After this pre-selection has been done, a more complex algorithm is used specifically to select $B \to D^*\rho$ events. For other Monte Carlo data sets, the pre-selection is not done as a separate processing stage but the pre-selection criteria are included in the final selection algorithm.

4.2.1 Pre-selection of Events

The pre-selection of events is made by looking at quantities relating to the whole event and quantities relating to specific tracks. The normalized second Fox-Wolfram moment [24], called R_2, is used to distinguish a $B\overline{B}$ event from a $q\overline{q}$ (where $q = u, d, s$ and c) event. R_2 is defined as

$$R_2 = \frac{H_2}{H_0}, \tag{4.1}$$

where

$$H_l = \frac{4\pi}{(2l+1)} \sum_{m=-l}^{l} \left| \sum_i Y_l^m(\Omega_i) \frac{|\vec{p}_i|}{E_{\rm tot}} \right|^2$$

and $Y_l^m(\Omega_i)$ are the spherical harmonics. Since the B mesons are significantly heavier than those produced in a $q\overline{q}$ event, the decay products of a $B\overline{B}$ event tend to be more spherically distributed than those of a $q\overline{q}$ event. R_2 expresses this fact quantitatively. Figure 4.2 shows the R_2 distributions for $B\overline{B}$, $q\overline{q}$ and $B^0 \to D^{*-}\rho^+$ events. R_2 is required to be less than 0.35. ρ candidates are constructed using the track and the π^0 lists, which are described in Sections 3.3.1 and 3.3.2. π_f candidates are selected from the track list and are combined with π^0s from the π^0 list. The resulting ρ candidate is then accepted if it passes the following criteria:

- $|m_\rho - M_\rho| < 0.320\,\mathrm{GeV/c^2}$
- $1.95 \leq |\vec{p}_\rho| \leq 2.45\,\mathrm{GeV/c}$
- $0.100 < m_{\pi^0} < 0.160\,\mathrm{GeV/c^2}$
- $|\vec{p}_{\pi^0}| \geq 0.200\,\mathrm{GeV/c}$

where $m_X(M_X)$ is the reconstructed (nominal [9]) mass of the candidate and $|\vec{p}_X|$ is the magnitude of the centre-of-mass (CM), i.e. the e^+e^- CM, momentum of the particle X.

π_s candidates are selected from the track list and are required to have a CM momentum greater than 0.050 but less than 0.800 GeV/c. The π_s candidate is then checked to see if it overlaps with the π_f produced by the decay of the ρ. If it does, it is rejected. The event is passed if at least one ρ candidate and one π_s candidate have passed the selection criteria.

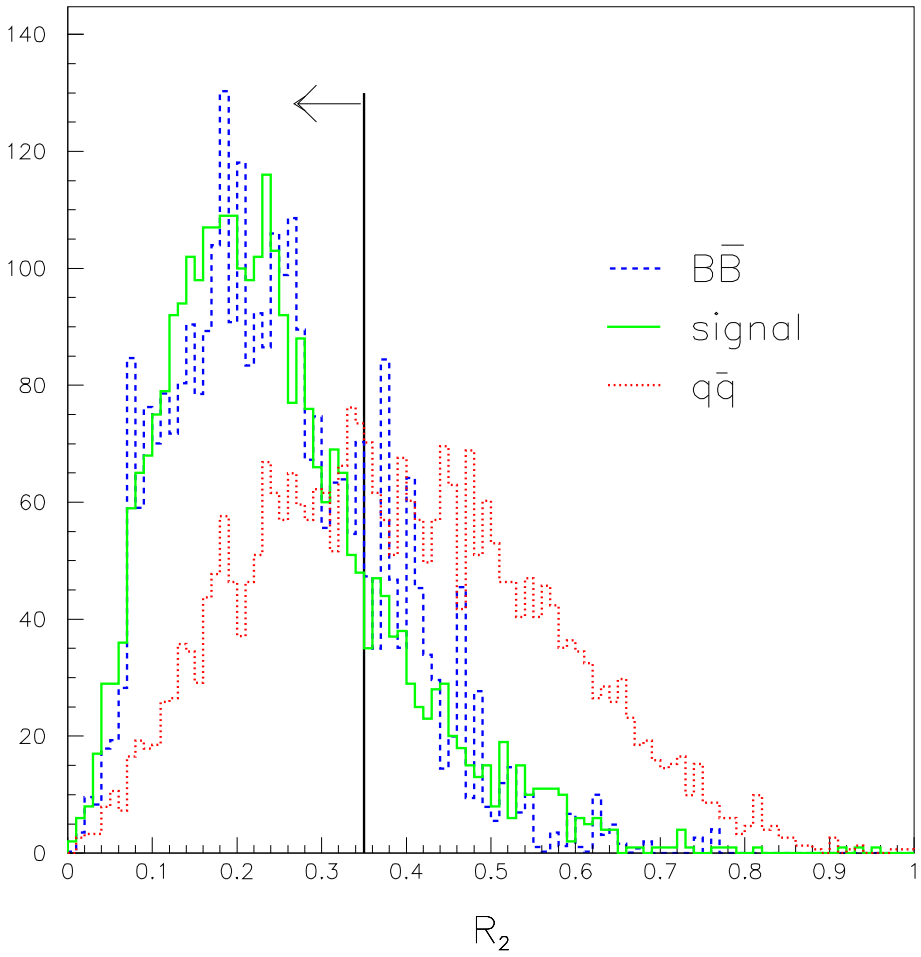

Figure 4.2: R_2 distribution for signal, $B\overline{B}$ and $q\overline{q}$ events. Events are required to have $R_2 < 0.35$.

All of these cuts are designed to reduce the data volume without rejecting many signal events. Table 4.1 lists the efficiency of the pre-selection, based on events that pass the Level-3 trigger, for signal Monte Carlo data and on-resonance and off-resonance data.

4.2.2 Final Event Selection

After an event has passed the pre-selection, the final event selection criteria are then applied. If the event passes these and the total charge of the $\rho\pi_s$ pair is zero certain quantities will be written to a file to be used in fitting the branching fraction and the B lifetime.

Event Type	Efficiency (%)
signal	31
on-resonance	2
off-resonance	4

Table 4.1: Pre-selection efficiencies.

ρ Candidate Selection Criteria

In the final selection the ρ and π^0 cuts are tightened to:

- $0.115 \leq m_{\pi^0} \leq 0.155\,\mathrm{GeV/c^2}$
- $|\vec{p}_{\pi^0}| > 0.400\,\mathrm{GeV/c}$
- $0.450 \leq m_{\rho} \leq 1.070\,\mathrm{GeV/c^2}$

Figure 4.3 shows the distributions of m_ρ, $|\vec{p}_\rho|$, m_{π^0} and $|\vec{p}_{\pi^0}|$ and indicates where the cuts are made. ρ candidates are selected if their mass is within about twice the nominal width from the nominal mass. The cut on $|\vec{p}_\rho|$ is made to select ρ candidates that lie within the kinematically allowed region. The cut on $|\vec{p}_{\pi^0}|$ is made just after the region in which background events peak. The cut on m_{π^0} is made at twice the expected π^0 mass resolution.

The point-of-closest-approach of the π_f to the beamspot is used to reject ρ candidates if this point is

- > 1.5 cm in the xy-plane, or
- > 6.0 cm in the z direction from the beamspot,

where the xy-plane is perpendicular to the beam direction and the z direction is along beam direction. Figure 4.4 shows the distributions of the point-of-closest-approach in the xy-plane and z direction. This cut is made to reject events where the selected π_f either comes from a K_s or is a random track that does not come from the interaction region.

Particle identification information is used to reject the ρ candidate if the π_f daughter is found to be in the e, μ, or K lists described in Section 3.3.3. The probability that a true π_f candidate is rejected by this selection is 3%. Table 4.2

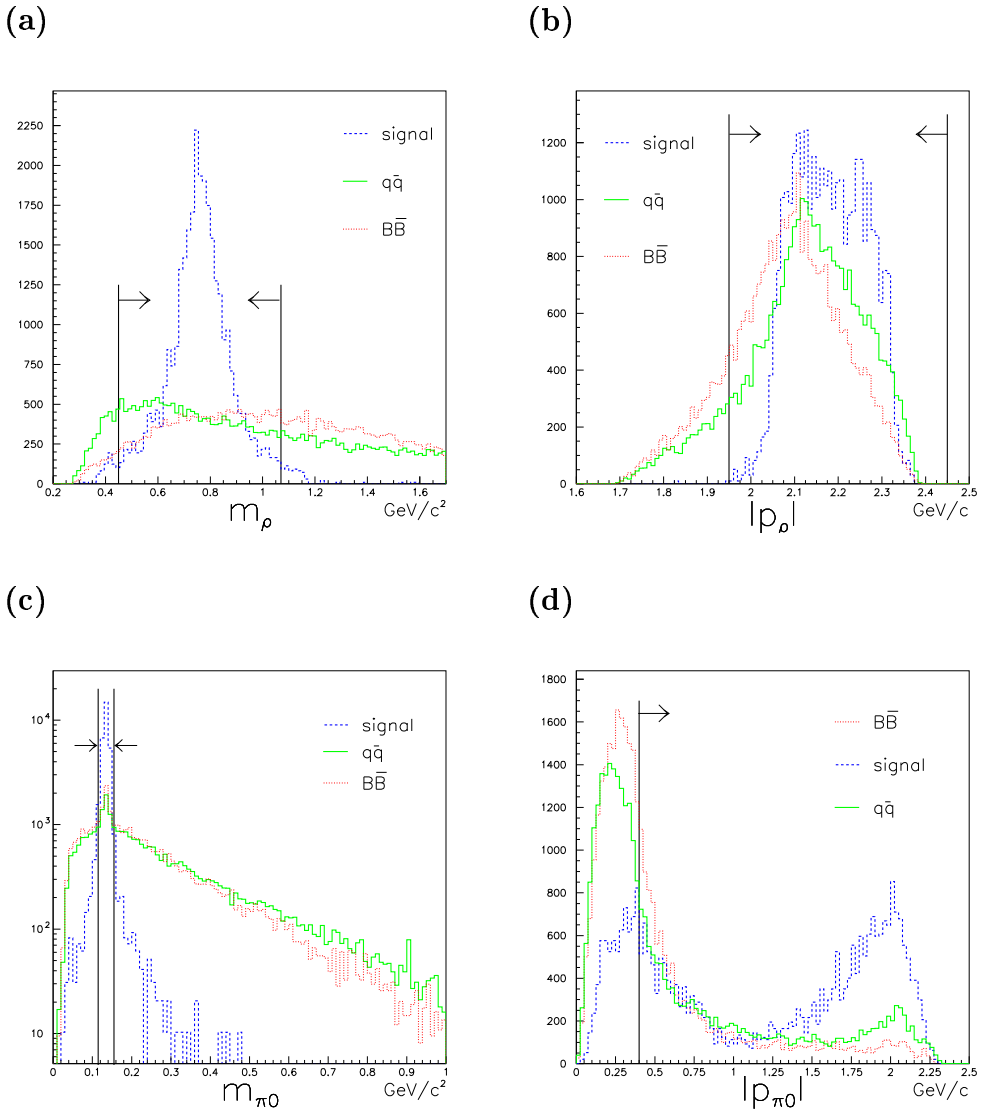

Figure 4.3: (a) ρ mass, (b) ρ CM momentum, (c) π^0 mass and (d) π^0 CM momentum for signal, $B\overline{B}$ and $q\overline{q}$ event types. The regions accepted by the final selection are indicated by the arrows.

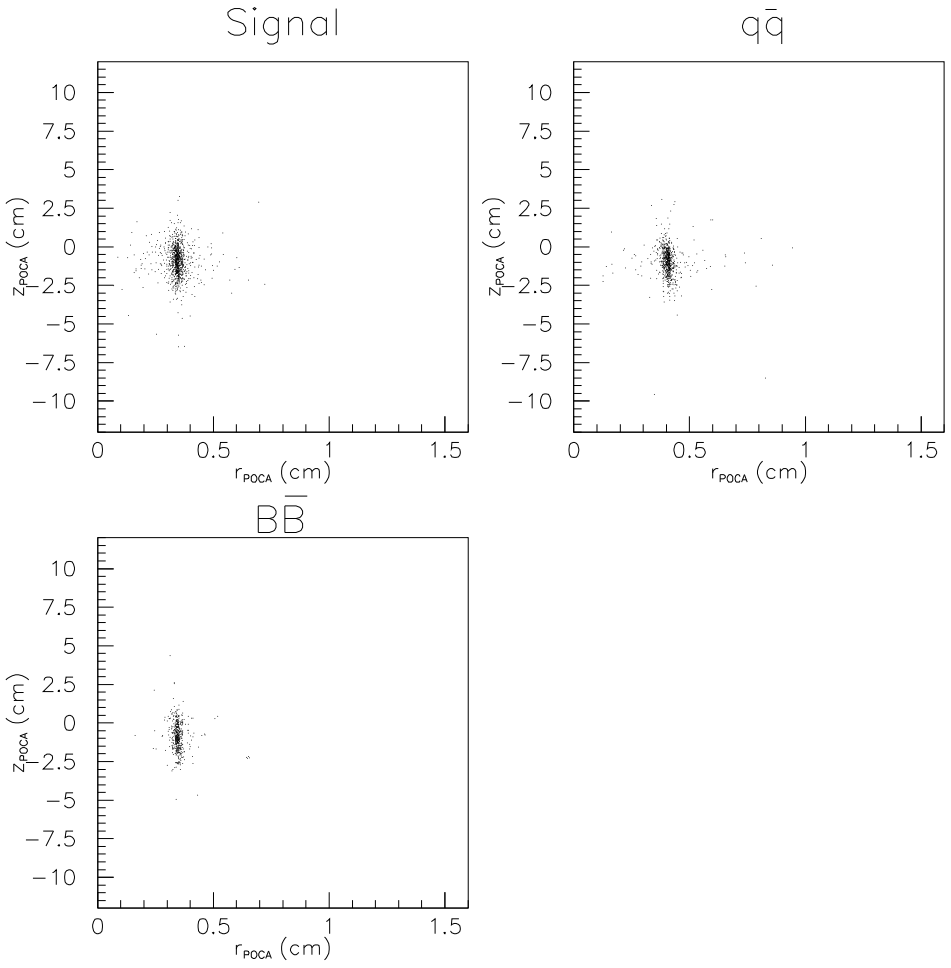

Figure 4.4: The distribution of the point-of-closest-approach, in the xy plane and the z direction, for the π_f.

lists the percentage of signal and $B\overline{B}$ events where the selected π_f candidate is either a muon, electron, kaon or proton.

π_s Candidate Selection Criteria

In the final selection, the CM momentum cut is tightened to $0.050 \leq |\vec{p}_{\pi_s}| \leq 0.600\,\mathrm{GeV/c}$. The π_s candidate is also required not to be in the e, μ or K lists. The probability that a true π_s candidate is rejected by this selection is 1%. Table 4.3 lists the percentage of signal and $B\overline{B}$ events where the selected π_s candidate is either a muon, electron, kaon or proton.

True id of π_f candidate	% of mis-identified π_f candidates	
	signal	$B\overline{B}$
μ	0.42	3.74
e	1.00	2.39
K	0.32	1.93
p	0.05	0.89
Total	1.79	8.95

Table 4.2: Percentage of signal and $B\overline{B}$ events where the selected π_f candidate is either a muon, electron, kaon or proton.

True id of π_s candidate	% of mis-identified π_s candidates	
	signal	$B\overline{B}$
μ	1.34	2.47
e	1.08	6.75
K	0.08	0.62
p	0.40	0.96
Total	2.9	10.8

Table 4.3: Percentage of signal and $B\overline{B}$ events where the selected π_s candidate is either a muon, electron, kaon or proton.

Helicity Angles

The helicity angle (or decay angle) of a particle is defined in its rest frame as the angle between the momentum vector of one of its decay products and the momentum vector of its mother. Figure 4.5 illustrates this. Since the momentum vector of the B is not completely known, the ρ helicity angle is defined using the momentum vector of the π^0 and the CM. For the D^*, the helicity angle is defined as the angle between the B and the $\overline{D}^0$ and is determined using

$$\cos\theta_{D^*} = \frac{-\beta_{D^*}(E_s^* - E_D^*)}{2p_s^*} + \frac{p_s^2 - p_D^2}{2\gamma_{D^*}^2\beta_{D^*}M_{D^*}p_s^*}, \tag{4.2}$$

where E_D^*, E_s^* and p_s^* are the energy and momentum of the D and π_s in the D^* rest frame; p_X is the momentum of X in the CM frame; γ_{D^*} and β_{D^*} are the Lorentz boost parameters for boosting the D^* from the CM frame to the D^* rest frame and $M_{D^*} = 2010.0 \pm 0.5\,\text{MeV}$ is the mass of the charged D^* [9]. E_D^* and p_s^* are calculated by applying conservation of energy and momentum to the decay of the D^*. p_D is

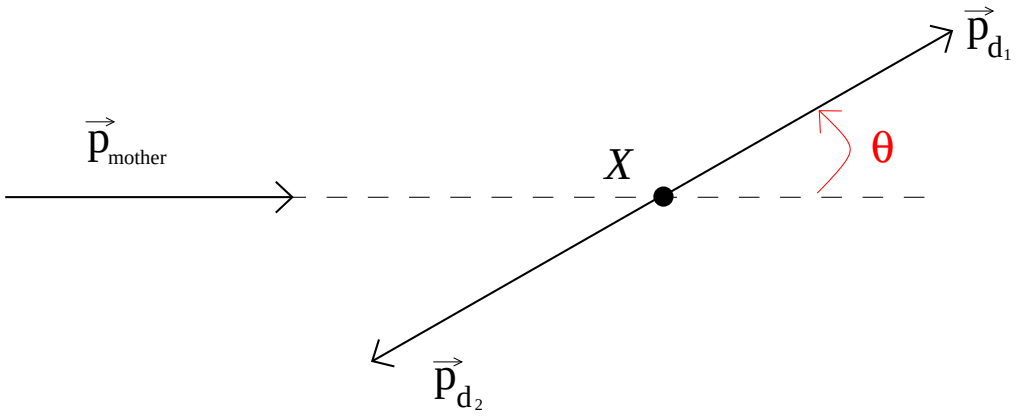

Figure 4.5: The helicity angle is defined, in the rest frame of X, as the angle between the momentum vectors $\vec{p}_{\rm mother}$ and $\vec{p}_{\rm d_1}$. For the ρ, $\rm d_1$ is the π^0. For the D^* $\rm d_1$ is the $\overline{D}^0$.

calculated using

$$p_D^2 = (E_B - E_{\pi_s} - E_\rho)^2 - M_D^2, \tag{4.3}$$

where E_X is the CM energy of X and $M_D = 1864.5 \pm 0.5\,\mathrm{MeV/c^2}$ is the mass of the D^0 [9]. The magnitude of $\cos\theta_{D^*}$ is not restricted to physical values as this would bias the background $m_{\rm miss}$ distribution to peak in the signal region.

The spins of the D^* and the ρ will be correlated because the B is a spin-0 meson which decays to spin-1 particles. Figure 4.6 shows the distributions of $\cos\theta_\rho$ and $\cos\theta_{D^*}$ for different event types. As can be seen, signal events are clustered towards $|\cos\theta| = 1$, whereas $q\overline{q}$ events have a more even distribution. Events are accepted if they satisfy $|\cos\theta| > 0.3$. However, events that satisfy $\cos\theta_\rho > -0.3$ and $\cos\theta_{D^*} < 0.3$ are rejected since $B\overline{B}$ background events are clustered in this region.

Selection of the Best Candidate

For each event there can be more than one $\rho\pi_s$ pair that passes the event selection criteria. Fig. 4.7 shows the candidate multiplicity for different event types. As can be seen there is normally more than one $\rho\pi_s$ candidate per event that passes all of the selection criteria described above. In this case, the candidate with the smallest value of $m_{\rm miss} - M_D$ is selected. The efficiency of this selection is 84.6% for signal events.

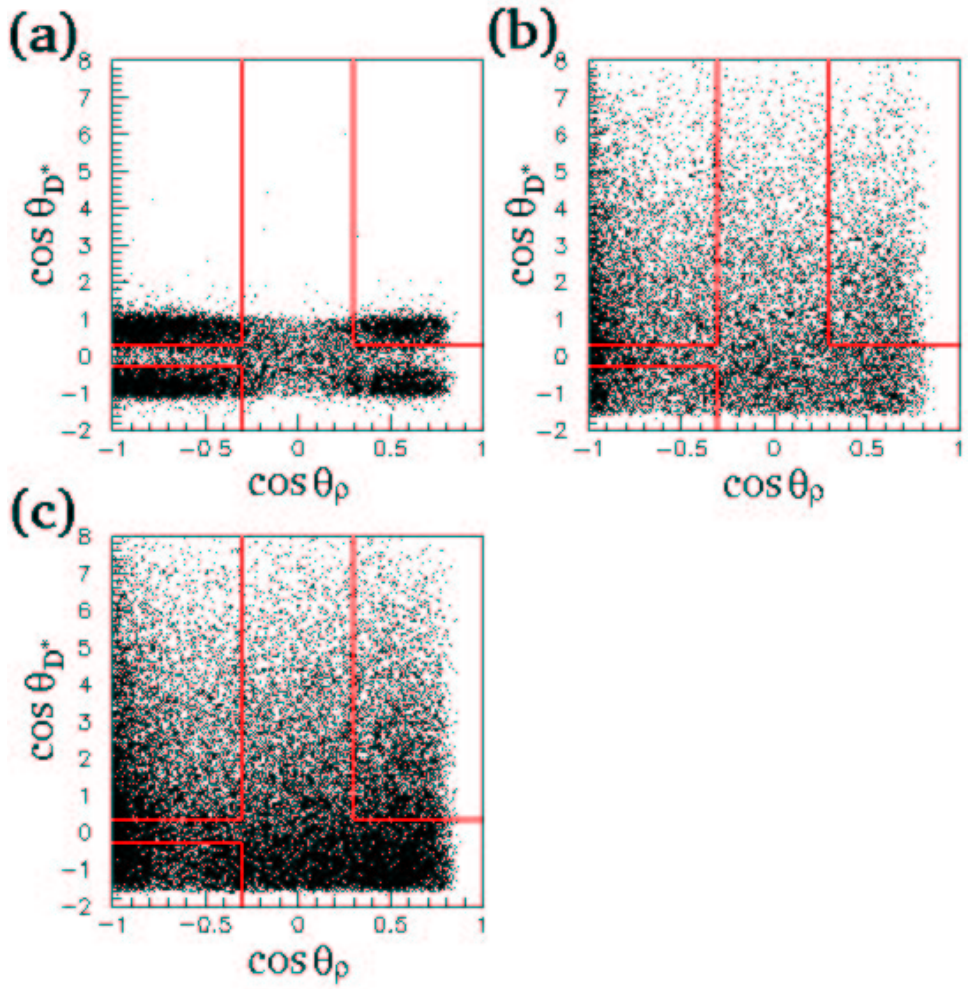

Figure 4.6: Distribution of $\cos\theta_{D^*}$ and $\cos\theta_\rho$ for (a) Signal, (b) $q\overline{q}$ and (c) $B\overline{B}$ events.

4.3 Quality of the Event Selection

Table 4.4 lists the efficiencies, after all the selection criteria have been applied and the expected numbers of events in the on-resonance sample, i.e. $20\,\mathrm{fb}^{-1}$. The efficiencies given also include the cuts that restrict the range of the variables used for the branching fraction and B lifetime fits. In determining the expected number of events in the on-resonance sample the following branching fractions for the D_1^0 and D_2^{*0} modes were used [23]:

$$\mathcal{B}(D_1^0 \to D^{*+}\pi^-) = 2/3 \text{ and} \quad (4.4)$$

$$\mathcal{B}(D_2^{*0} \to D^{*+}\pi^-) = 0.209 \quad (4.5)$$

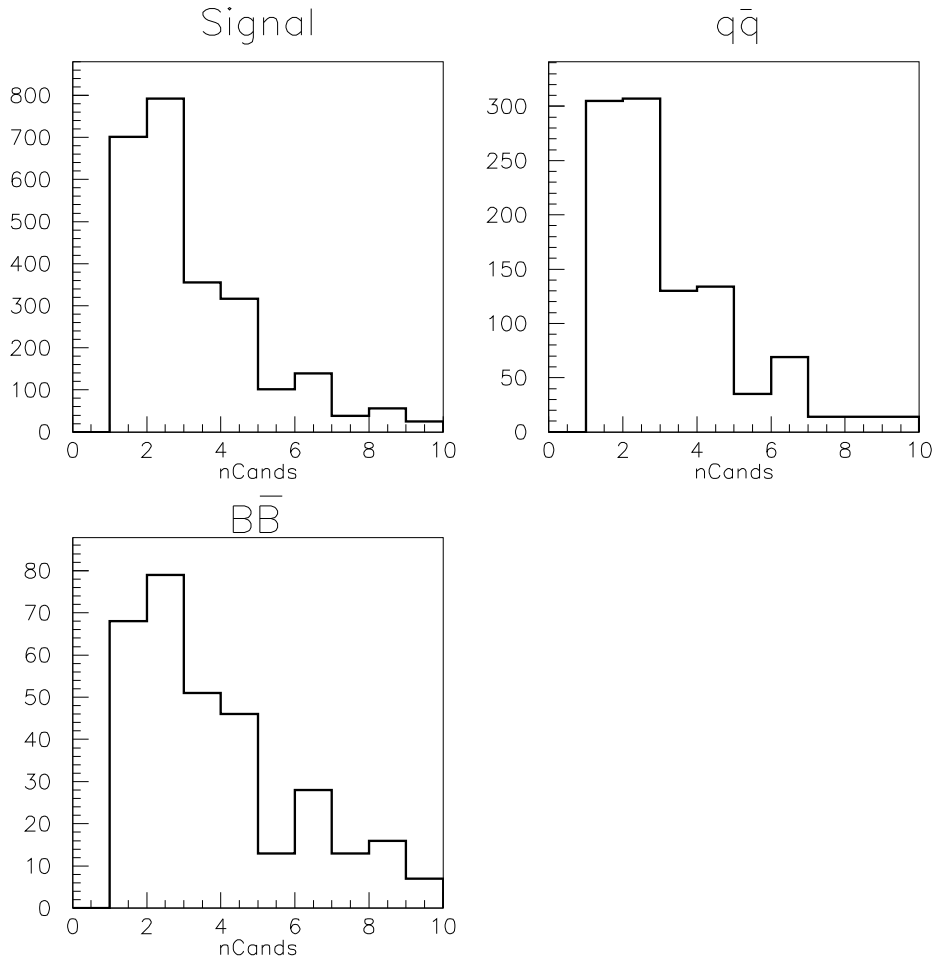

Figure 4.7: Number of $\rho\pi_s$ candidates per event for signal, $q\overline{q}$ and $B\overline{B}$ events.

and for the decay of the D^*, $\mathcal{B}(D^{*+} \to D^0\pi^+) = 0.677$ [9] was used.

The modes $B \to D^* a_1$, $B^+ \to D_2^0\rho^+$, $B \to D^*\pi\pi^0$ and $B^+ \to D_1^0\rho^+$ peak in $m_{\rm miss}$ at the D mass. Since the total efficiency for these events is significant, selecting events using $m_{\rm miss}$ only would lead to a bigger systematic error due to the uncertainty in the branching fractions of these modes. For the branching fraction measurement two additional variables are included to determine the signal yield; the ρ mass and the output of a Fisher discriminant. This is described in the following chapter.

Event type	Efficiency (%)	Expected Number of Events in 20 fb^{-1}
$q\overline{q}$	0.26	1.8×10^5
$B^0\overline{B}^0$	0.26	5.4×10^4
B^+B^-	0.52	1.1×10^5
$B \to D^* a_1$	1.44	2.7×10^3
$B^+ \to D_2^{*0}\rho^+$	3.24	7.6×10^1
$B \to D^*\pi\pi^0$	3.57	4.2×10^3
$B^+ \to D_1^0\rho^+$	5.42	2.3×10^3
$B^0 \to D^{*-}\rho^+$	11.5	1.1×10^4

Table 4.4: Total efficiencies for each of the event types. The statistical errors on the efficiencies are negligible.

Chapter 5

Measurement of the Branching Fraction of $B \to D^*\rho$

> "'That is quite so, 6655321. Of course, it's only in the experimental stage at the moment. It's very simple but very drastic."'
>
> A Clockwork Orange, Anthony Burgess.

After an event has passed the selection criteria described in the previous chapter, three variables for each event are written out to a text file: the output of a Fisher discriminant designed to separate $B\overline{B}$ events from $q\overline{q}$ events, the ρ candidate mass and the missing mass. These variables are then used in an unbinned maximum likelihood fit to determine the signal yield, from which the branching fraction can be calculated.

The following sections describe the probability density functions (pdfs) used to model the distributions of the variables, the procedure used to determine the signal yield and the study of systematic effects.

5.1 Fit Procedure

Using the partial reconstruction method means that the event selection has a lower purity than if all the decay products of the D were reconstructed. Each of the background modes listed in Sec. 4.1 are treated separately by constructing pdfs for each of them. Thus, the pdf that describes the on-resonance data is the weighted

sum of each background pdf and the pdf for signal events. This is described in more detail in Sec. 5.1.4. To determine the shapes of the background pdfs, Monte Carlo (for B decays) and off-resonance (for $q\overline{q}$ events) data are used. The following sections describe the pdfs used to describe the distributions of each variable.

5.1.1 The Fisher Discriminant Variable

Fisher discriminants are designed to take as input a number of variables and output a single test statistic based on a weighted linear combination of the input variables. Using Monte Carlo data it is possible to determine the weights that provide the optimal discrimination between different hypotheses. See [25] for a more general description of Fisher discriminants. The Fisher discriminant described here is used to provide separation between $B\overline{B}$ and $q\overline{q}$ events and is constructed using nine variables. These are the total CM energy (E_i) of particles found within nine concentric cones, each 10°-wide around $\vec{p}_\rho$, computed using all tracks and clusters excluding the ρ and π_s candidates. These energy-cone variables were first introduced by the CLEO experiment [26] and were found to be useful for constructing a Fisher discriminant. The Fisher discriminant variable is given by

$$\mathcal{F} = \sum_{i=1}^{9} w_i E_i, \tag{5.1}$$

where the w_i are weights determined by training the Fisher discriminant using $B^0 \to D^{*-}\pi^+$ and $q\overline{q}$ Monte Carlo events. $B^0 \to D^{*-}\pi^+$ events were used because this Fisher discriminant was first used for studying $B^0 \to D^{*-}\pi^+$ decays. Since the topologies of $B^0 \to D^{*-}\pi^+$ and $B^0 \to D^{*-}\rho^+$ events are similar, the Fisher discriminant was not retrained with $B^0 \to D^{*-}\rho^+$ Monte Carlo data. Figure 5.1 shows the distributions of $\mathcal{F}$ for signal, generic $B\overline{B}$ (excluding signal) Monte Carlo data and off-resonance data. A bifurcated Gaussian pdf, i.e. a Gaussian where the parameter sigma has different values either side of the mean, is found to match the distribution of $\mathcal{F}$ well. Figure 5.1 shows the results of the fits to Monte Carlo and off-resonance data. As can be seen, for $q\overline{q}$ events $\mathcal{F}$ peaks at a higher value than for $B\overline{B}$ events and the distribution of $\mathcal{F}$ for $B \to D^*\pi\pi^0$ events is more skewed than the distribution for signal events.

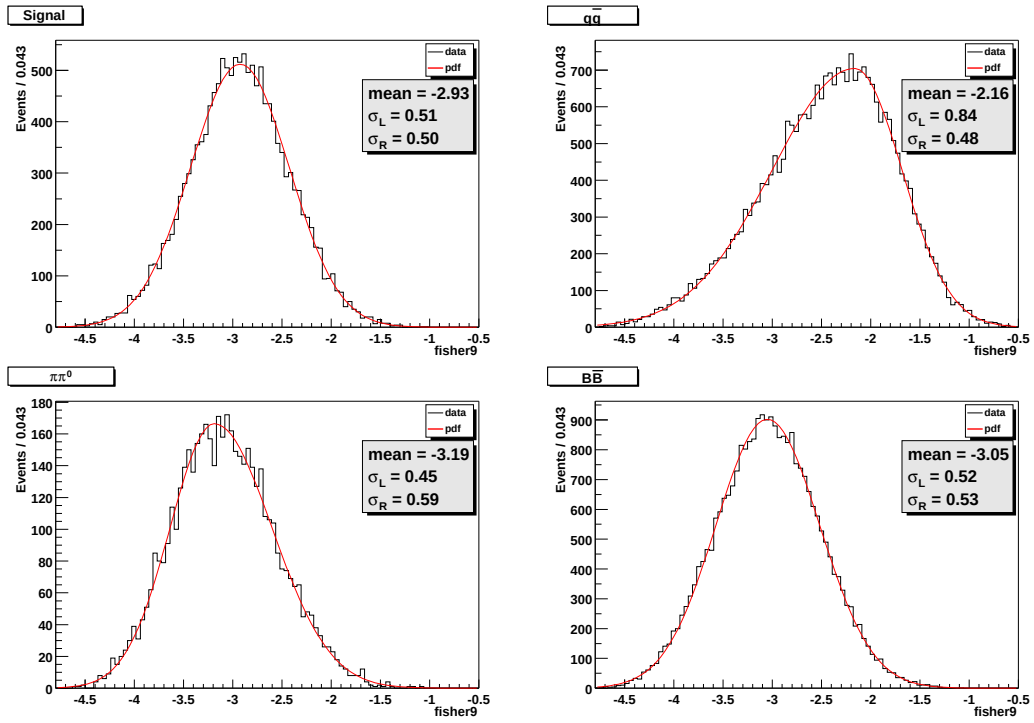

Figure 5.1: Fisher variable ($\mathcal{F}$) distributions and fitted pdfs for signal, $q\overline{q}$, $B \to D^*\pi\pi^0$ and generic $B\overline{B}$ events. The distribution of $\mathcal{F}$ peaks at higher values for jet-like events (i.e. $q\overline{q}$ events). As can be seen from the values of the two sigmas of the bifurcated Gaussian pdfs ($\sigma_{\rm L}$ and $\sigma_{\rm R}$), the shape of the peak for signal and generic $B\overline{B}$ events is fairly symmetric but is skewed for $B \to D^*\pi\pi^0$ events.

5.1.2 Rho-candidate Mass

The ρ-candidate mass (m_ρ) distribution is described by the weighted sum of a p-wave Breit-Wigner pdf and a 2$^{\rm nd}$ order polynomial. The p-wave Breit Wigner used is the one recommended for the m_ρ distribution in [27] and has the form

$$f_{\rm BW}(x\,;m,\Gamma) = \frac{1}{N}\cdot\frac{x^2m^4}{(m^2-x^2)^2+x^2\Gamma^2(x)}, \tag{5.2}$$

where $\Gamma(x)$ is given by

$$\Gamma(x) = \Gamma\cdot\frac{m^2p^3}{x^2p_0^3}$$

and p is the momentum of a daughter in the rest frame of the ρ when the mass of the ρ is x and p_0 is the momentum of a daughter when the mass is m. The normalization factor (N) is calculated by numerically integrating the pdf over the range of x, i.e. 0.450 to 1.070 GeV/c^2. The 2$^{\rm nd}$ order polynomial is used to describe the non-resonant background, i.e. $\pi^\pm\,\pi^0$ combinations that do not come from a ρ.

The weighting of the polynomial component depends on the event type. Figure 5.2 shows the distributions of m_ρ for some of the event types and the corresponding shapes of the pdf. As can be seen, for $B \to D^*\pi\pi^0$ events there is no p-wave Breit Wigner component and for $B \to D^*\rho$ events the polynomial component is small.

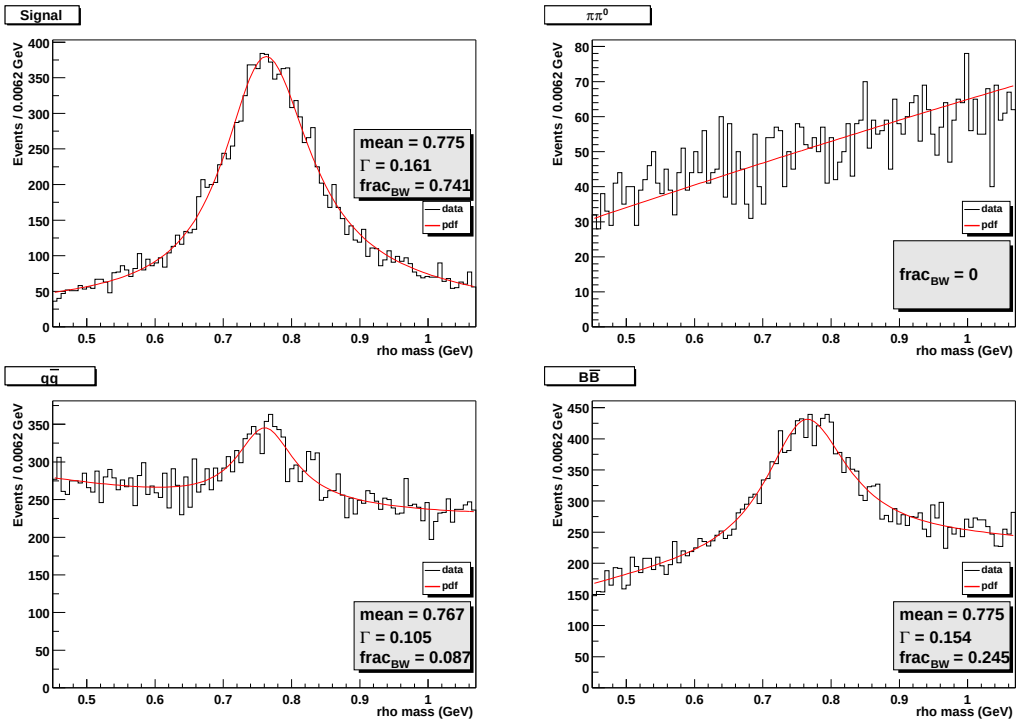

Figure 5.2: m_ρ distributions and fitted pdfs for signal, $B \to D^*\pi\pi^0$, $q\overline{q}$ and generic $B\overline{B}$ events. The pdf for signal events shows that the combinatoric background is small (i.e. the weighting of the p-wave Breit Wigner component, frac_{BW}, is large). For $B \to D^*\pi\pi^0$ events frac_{BW} is fixed at 0, which matches the data well.

5.1.3 Missing Mass

The missing mass is the mass of the system that recoils against the ρ and π_s in the decay of the B. Since the momentum vector of the B is not completely known, it is not possible to determine unambiguously the missing mass. In this case an estimator for the missing mass is constructed using the reconstructed tracks and the known boost direction of the CM system.

Constructing an Estimator for the Missing Mass

Consider the decay chain in Fig. 4.1. Conservation of four-momentum in the CM frame gives:

$$\begin{aligned} P_{\mathrm{D}^*} &= P_{\mathrm{B}} - P_\rho \\ m^2_{\mathrm{D}^*} &= m^2_{\mathrm{B}} + m^2_\rho - 2(E_{\mathrm{B}}E_\rho - |\vec{p}_{\mathrm{B}}||\vec{p}_\rho|\cos(\theta_{\mathrm{B}\rho})) \\ \cos\theta_{\mathrm{B}\rho} &= \frac{m^2_{\mathrm{D}^*} - m^2_{\mathrm{B}} - m^2_\rho + 2E_{\mathrm{B}}E_\rho}{2|\vec{p}_{\mathrm{B}}||\vec{p}_\rho|}, \end{aligned} \tag{5.3}$$

where m_{X} is the mass of X [9]. $|\vec{p}_{\mathrm{B}}|$ is calculated using the mass of the B^0. For an on-resonance run the energy of the B (E_B) is taken to be half the CM energy. For off-resonance events the CM energy is less than twice the mass of the B meson and therefore the momentum of the B candidate cannot be calculated using

$$p_B = \sqrt{E_B^2 - m_B^2}. \tag{5.4}$$

In this case the energy of the B is taken to be half the average of the CM energies of recent on-resonance runs, which is typically 5.29 GeV. The magnitude of $\cos\theta_{\mathrm{B}\rho}$ is required to be less than 1.

To calculate the missing mass, consider four-momentum conservation

$$P_{\mathrm{D}} = P_{\mathrm{B}} - P_\rho - P_{\pi_{\mathrm{s}}}. \tag{5.5}$$

Squaring both sides gives

$${m_{\mathrm{miss}}}^2 = (P_{\mathrm{B}} - P_\rho)\cdot(P_{\mathrm{B}} - P_\rho) - 2P_{\pi_{\mathrm{s}}}(P_{\mathrm{B}} - P_\rho) + m^2_{\pi_{\mathrm{s}}}. \tag{5.6}$$

Equation 5.3 gives

$$(P_{\mathrm{B}} - P_\rho)\cdot(P_{\mathrm{B}} - P_\rho) = m^2_{\mathrm{D}^*} \tag{5.7}$$

and therefore,

$$\begin{aligned} {m_{\mathrm{miss}}}^2 &= m^2_{\mathrm{D}^*} + m^2_{\pi_{\mathrm{s}}} + 2E_\rho E_{\pi_{\mathrm{s}}} - 2|\vec{p}_\rho||\vec{p}_{\pi_{\mathrm{s}}}|\cos\theta_{\rho\pi_{\mathrm{s}}} \\ &\quad -2E_{\mathrm{B}}E_{\pi_{\mathrm{s}}} + 2|\vec{p}_{\mathrm{B}}||\vec{p}_{\pi_{\mathrm{s}}}|\cos\theta_{\mathrm{B}\pi_{\mathrm{s}}}. \end{aligned} \tag{5.8}$$

The only quantity here that is not measured is $\cos\theta_{\mathrm{B}\pi_s}$. Since only $\cos\theta_{\mathrm{B}\rho}$ is known and not the azimuthal angle of $\vec{p}_{\mathrm{B}}$ about $\vec{p}_\rho$, there is an infinite number of solutions for $\vec{p}_{\mathrm{B}}$ and thus an infinite number of solutions for $\cos\theta_{\mathrm{B}\pi_s}$. The estimator for m_{miss} is constructed using the two solutions for $\cos\theta_{\mathrm{B}\pi_s}$ that maximise and minimise the missing mass, i.e. when $\cos\theta_{\mathrm{B}\pi_s}$ is maximal and minimal, respectively. These two solutions can be determined by considering the momentum vectors of the B, ρ and π_s in the coordinate system illustrated in Fig. 5.3. One basis vector is parallel to

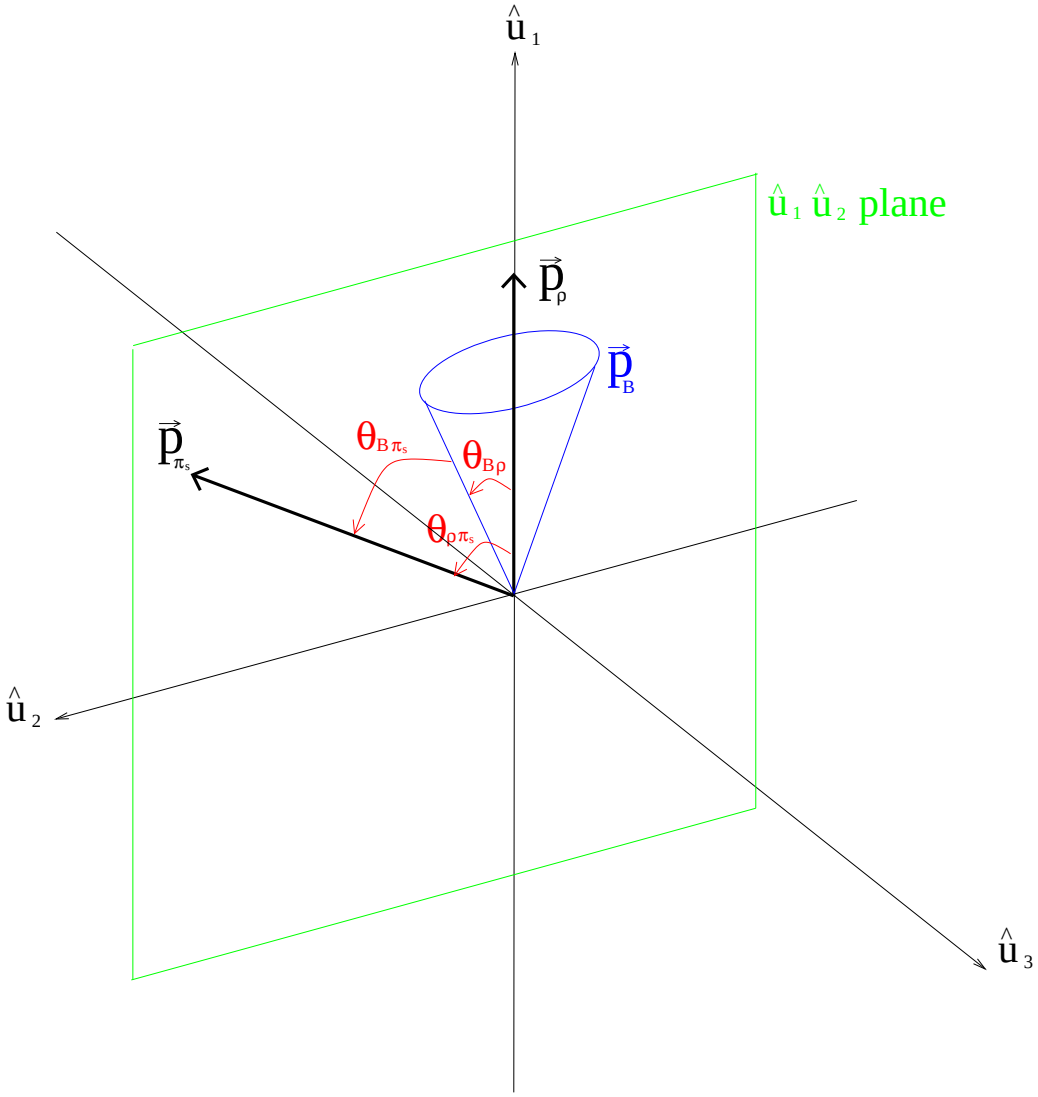

Figure 5.3: Diagram illustrating how the maximum and minimum values of $\theta_{B\pi_s}$ are determined. $\vec{p}_\rho$ and $\vec{p}_{\pi_s}$ are in the $\hat{u}_1\hat{u}_2$ plane and the possible $\vec{p}_{\mathrm{B}}$ solutions are given by the cone around $\vec{p}_\rho$ that subtends an angle $\theta_{\mathrm{B}\rho}$.

the ρ ($\hat{u}_1$) and the other ($\hat{u}_2$), which is perpendicular to $\hat{u}_1$, is defined such that the plane $\hat{u}_1\hat{u}_2$ contains the π_s and the ρ and that the angle between $\vec{p}_{\pi_s}$ and $\hat{u}_2$ is acute.

Figure 5.3 illustrates that $\cos\theta_{\mathrm{B}\pi_\mathrm{s}}$ is minimal and maximal when $\vec{p}_\mathrm{B}$ is in the plane $\hat{u}_1\hat{u}_2$, i.e. when $\theta_{\mathrm{B}\pi_\mathrm{s}}$ is maximal and minimal, respectively. This is calculated in the analysis algorithm as follows. The momentum vector of the B can therefore be written as

$$\vec{p}_\mathrm{B} = |\vec{p}_\mathrm{B}|(\cos\theta_{\mathrm{B}\rho}\hat{u}_1 \pm \sin\theta_{\mathrm{B}\rho}\hat{u}_2) \tag{5.9}$$

and the π_s as

$$\vec{p}_{\pi_\mathrm{s}} = |\vec{p}_{\pi_\mathrm{s}}|(\sin(\pi/2-\theta_{\rho\pi_\mathrm{s}})\hat{u}_1 + \cos(\pi/2-\theta_{\rho\pi_\mathrm{s}})\hat{u}_2). \tag{5.10}$$

The minimum and maximum solutions of $\cos\theta_{\mathrm{B}\pi_\mathrm{s}}$ can now be calculated by taking the dot product of $\vec{p}_\mathrm{B}$ and $\vec{p}_{\pi_\mathrm{s}}$

$$\cos\theta_\mathrm{max} = \sin(\pi/2-\theta_{\rho\pi_\mathrm{s}})\cos\theta_{\mathrm{B}\rho} + \sin\theta_{\mathrm{B}\rho}\cos(\pi/2-\theta_{\rho\pi_\mathrm{s}}) \tag{5.11}$$

$$\cos\theta_\mathrm{min} = \sin(\pi/2-\theta_{\rho\pi_\mathrm{s}})\cos\theta_{\mathrm{B}\rho} - \sin\theta_{\mathrm{B}\rho}\cos(\pi/2-\theta_{\rho\pi_\mathrm{s}}). \tag{5.12}$$

So, using these two solutions in equation 5.8 we have two solutions for m_miss from which we take the mean. From here on, the term 'missing mass' will be used to denote the mean of the two solutions, as defined here. Figure 5.4 shows the distribution of the missing mass for different event types.

Parameterisation of the missing mass pdf

The pdf used to describe the m_miss distribution is the weighted sum of a bifurcated Gaussian and an ARGUS function [28]. The ARGUS function is given by

$$f_\mathrm{ARGUS}(m; m_0,\ c) = m\sqrt{1-(m/m_0)^2}\cdot\exp\left(c\left(1-(m/m_0)^2\right)\right)\cdot\theta(m<m_0), \tag{5.13}$$

where $\theta(m < m_0)$ is a step function. The ARGUS function is used to describe background events where a random $\rho\,\pi$ combination has been selected. In this case the m_miss distribution will not peak at the D mass but will have a flatter distribution over a much broader range. For signal-like background modes (i.e. $B \to D^*\pi\pi^0$, $B \to D^* a_1$ and $B \to D^{**}\rho$) there is a peak at the D mass and a significant ARGUS function component. For signal events there is a small ARGUS component that is

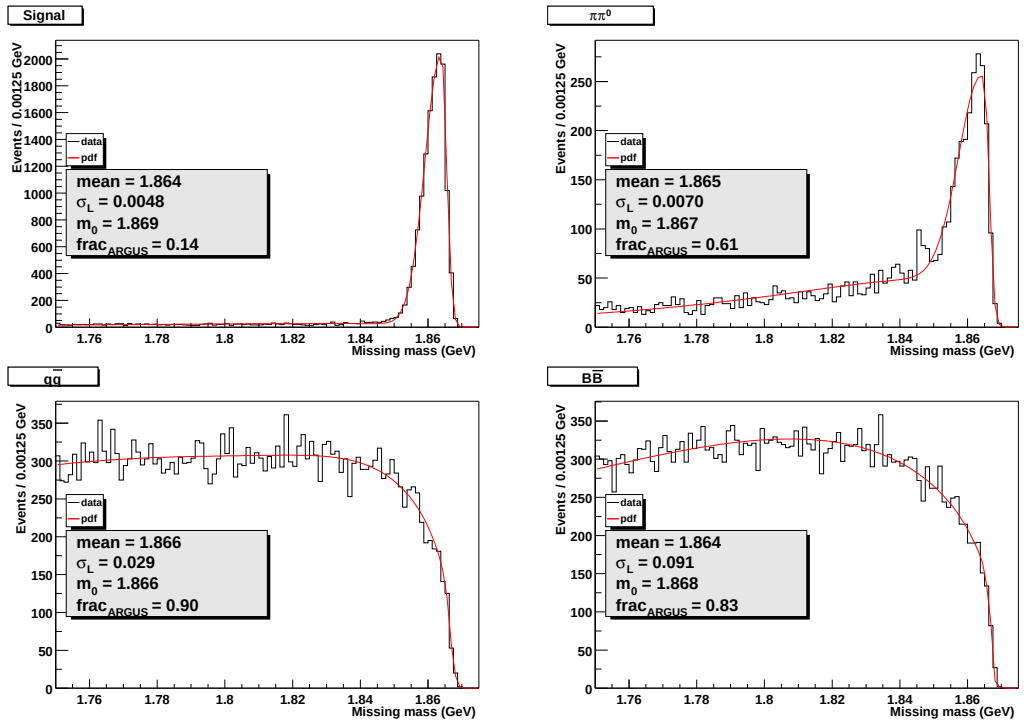

Figure 5.4: $m_{\rm miss}$ distributions and fitted pdfs for signal, $B \to D^*\pi\pi^0$, $q\overline{q}$ and generic $B\overline{B}$ events. The pdf for signal events shows that the combinatoric background is small (i.e. the weighting of the ARGUS function component, $\mathrm{frac}_{\rm ARGUS}$, is small). For $q\overline{q}$ and $B\overline{B}$ events the pdf is dominated by the ARGUS function component.

due to misreconstruction.

5.1.4 The Global Fit

For each event type a three dimensional pdf ($m_{\rm miss}$, $\mathcal{F}$ and m_ρ) is constructed by taking the product of the pdfs that describe each variable. To verify that this ansatz for the joint pdf is reasonable, i.e. that correlations are negligible, the correlation coefficient is estimated from the on-resonance data using

$$r = \frac{\sum_{i=1}^{N}\left(x_i - \overline{x}\right)\left(y_i - \overline{y}\right)}{\sqrt{\sum_{j=1}^{N}\left(x_j - \overline{x}\right)^2 \cdot \sum_{k=1}^{N}\left(y_k - \overline{y}\right)^2}}. \tag{5.14}$$

Table 5.1 lists the values of r obtained for $m_{\rm miss}$, $\mathcal{F}$ and m_ρ.

Since the correlations are small, the pdf that describes event type x can be well approximated by

$$f_x(m_\rho, m_{\rm miss}, \mathcal{F}) = f_{m_\rho}(m_\rho) \cdot f_{m_{\rm miss}}(m_{\rm miss}) \cdot f_{\mathcal{F}}(\mathcal{F}), \tag{5.15}$$

	$m_{\rm miss}$	$\mathcal{F}$	m_ρ
$m_{\rm miss}$	1	1.43×10^{-2}	4.27×10^{-4}
$\mathcal{F}$		1	-4.40×10^{-2}
m_ρ			1

Table 5.1: Correlations between the variables used in the fit for the branching fraction.

where f_{m_ρ} is the weighted sum of a p-wave Breit-Wigner and a 2^{nd} order polynomial, $f_{m_{\rm miss}}$ is the weighted sum of a bifurcated Gaussian and the ARGUS function and $f_{\mathcal{F}}$ is a bifurcated Gaussian. The pdf used to describe the on-resonance data is the weighted sum of the components that describe the different event types

$$\begin{aligned} f_{\rm on}(m_\rho, m_{\rm miss}, \mathcal{F}) &= w_{\rm signal} f_{\rm signal} + w_{D^*\pi\pi^0} f_{D^*\pi\pi^0} + w_{D^*a_1} f_{D^*a_1} \\ &\quad + w_{D_1} f_{D_1} + w_{D_2} f_{D_2} + w_{q\bar{q}} f_{q\bar{q}} \\ &\quad + (1 - w_{\rm signal} - w_{D^*\pi\pi^0} - w_{D^*a_1} - w_{D_1} - w_{D_2} - w_{q\bar{q}}) f_{B\bar{B}} \end{aligned} \quad (5.16)$$

The important parameter here is $w_{\rm signal}$ which gives us the signal yield. The parameters in the B decay mode background pdfs are determined by fitting to Monte Carlo data. For the continuum component, off-resonance data is used to determine the parameters of $f_{q\bar{q}}$. In principle, this could be done by doing a simultaneous fit to all the data sets whereby the Monte Carlo and off-resonance data is used to constrain the shapes of the background pdfs at the same time that the on-resonance data is fitted. In this case the statistical error, which includes the correlations between the parameters, is more accurately determined. However, this was found to be numerically difficult due to the complexity of the pdf. Instead, each background mode was separately fitted to Monte Carlo and off-resonance data to obtain the background parameters, which were then fixed in the fit to the on-resonance data. Thus, in the fit to determine the signal yield, all the parameters of $f_{\rm on}$, except the weights w_x, were fixed.

5.2 Fit Results

Table 5.2 gives the results of the fit. Figure 5.5 shows the projections of the three

Parameter	Fitted value
w_{signal}	$(2.510\pm0.054)\times10^{-2}$
$w_{D^*\pi\pi^0}$	$0\pm9\times10^{-5}$
$w_{D^*a_1}$	$0\pm1\times10^{-4}$
w_{D_1}	$0\pm8\times10^{-5}$
w_{D_2}	$0\pm9\times10^{-5}$
$w_{q\overline{q}}$	$(7.47\pm0.02)\times10^{-1}$

Table 5.2: Fitted values of the weights w_x.

variables of the fitted on-resonance pdf with its individual components overlaid. Figure 5.6 shows the on-resonance data with the pdfs of the different event types overlaid, as in Fig 5.5 but with the weights w_x (defined in Eq. 5.16) set to those used to generate the Monte Carlo data. This plot indicates that the branching fraction used in the Monte Carlo is higher than in the data, which is consistent with the result obtained.

5.3 Branching Fraction Result

The branching fraction is calculated from the signal yield, signal efficiency and the number of B mesons produced. The number of B mesons produced is determined using:

$$N_B = \sigma_{\Upsilon(4S)} \times \mathcal{L} \tag{5.17}$$

$$= 1.14\,\text{nb} \times 20.07 \times 10^6\,\text{nb}^{-1} = 22.88 \times 10^6, \tag{5.18}$$

where $\sigma_{\Upsilon(4S)}$ is the $\Upsilon(4S)$ production cross-section [29] and $\mathcal{L}$ is the integrated luminosity of the on-resonance data set [30]. The assumption made here is that

$$\mathcal{B}(\Upsilon(4S) \to B^+B^-) = \mathcal{B}(\Upsilon(4S) \to B^0\overline{B}^0) = 50\%. \tag{5.19}$$

The signal yield is given by

$$N_s = w_{\text{signal}} \times N_{\text{on}} \tag{5.20}$$

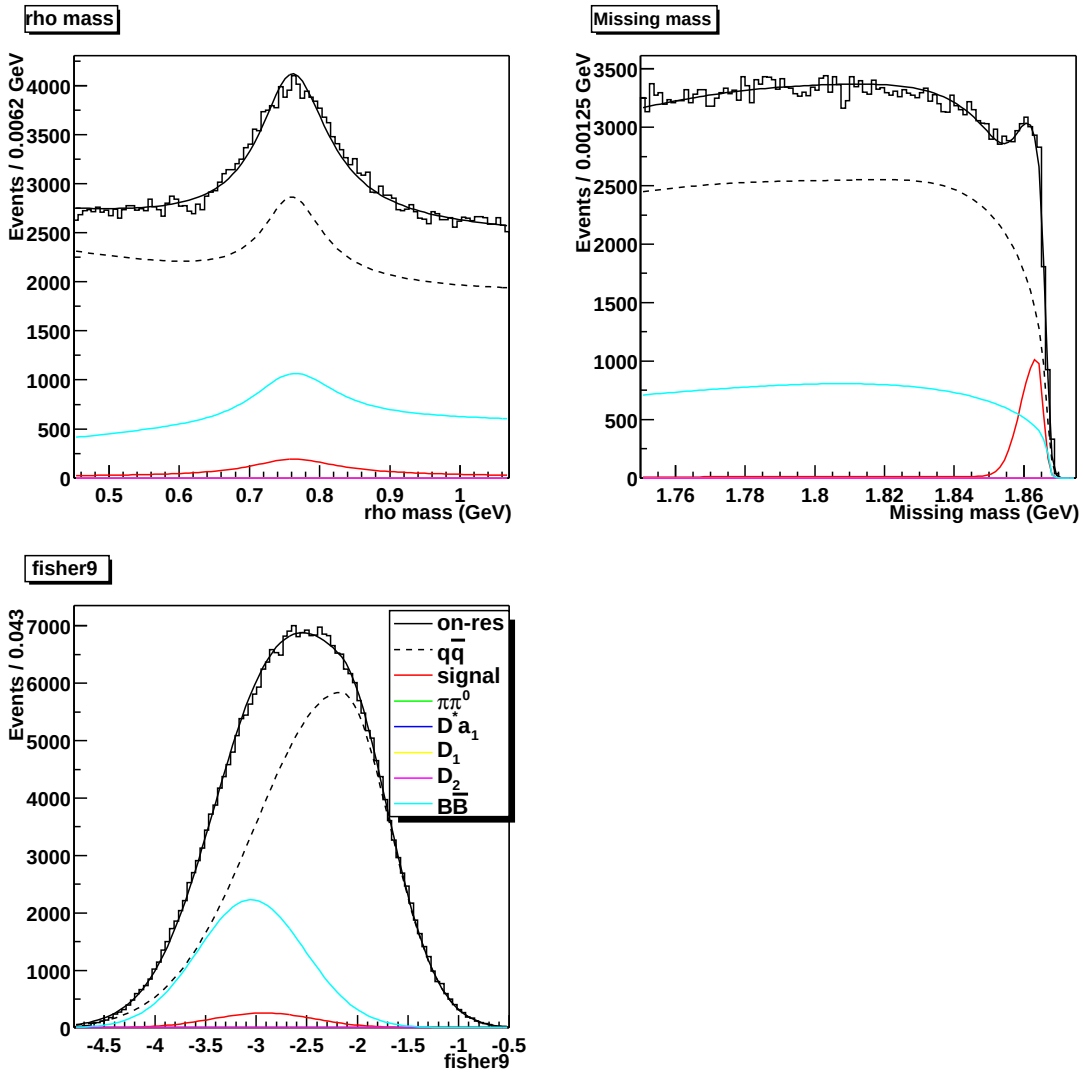

Figure 5.5: Results of the fit showing the projections of m_ρ, $m_{\rm miss}$ and $\mathcal{F}$ with the different event types overlaid. The weight of each event type is taken from Tab. 5.2.

$$= \quad (2.510 \pm 0.053) \times 10^{-2} \times 300821 = 7551 \pm 159, \tag{5.21}$$

where $w_{\rm signal}$ and its error are taken from the fit results in Tab. 5.2 and $N_{\rm on}$ is the number of events in the on-resonance data sample. Therefore, the branching fraction is

$$\begin{aligned} \mathcal{B}(B \to D^* \rho) &= \frac{N_s}{N_B \cdot \varepsilon} \\ &= \frac{7551}{22.88 \times 10^6 \times 0.0779} = (4.24 \pm 0.09) \times 10^{-3}, \end{aligned} \tag{5.22}$$

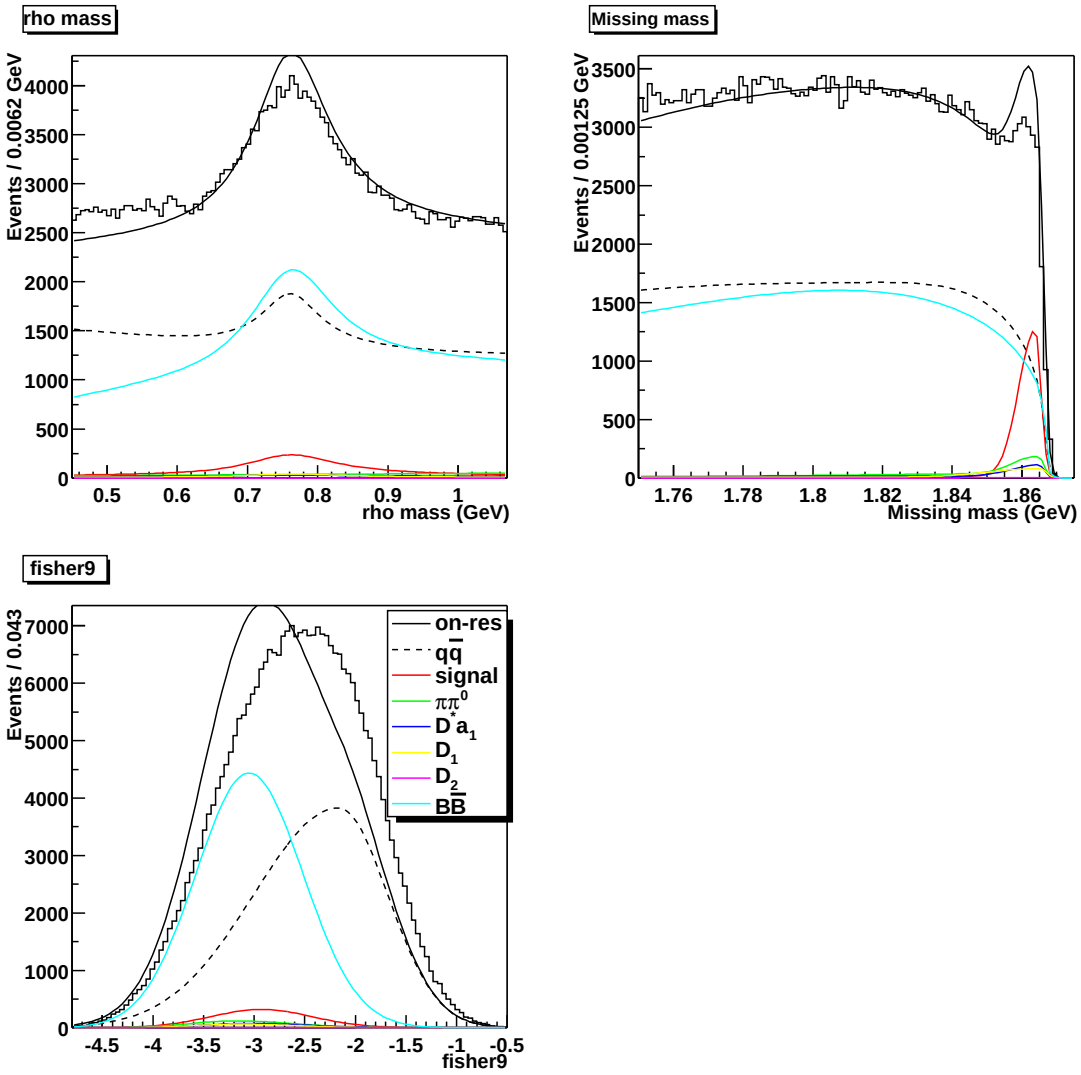

Figure 5.6: Projections of m_ρ, m_{miss} and $\mathcal{F}$ with the values of w_x taken from the expected number of events in Tab. 4.4.

where ε is the total efficiency for signal events and is the product of the signal efficiency from Tab. 4.4 and $\mathcal{B}(D^{*+} \to D^0\pi^+) = 0.677 \pm 0.005$ [9].

5.4 Systematic Checks

Several things were looked at to estimate the systematic error. Previous studies of $\mathcal{B}(B^0 \to D^{*-}\rho^+)$, using a similar method [33], have shown that the major sources of systematic errors due to the chosen values for cuts come from the R_2, the helicity angle (described in Sec. 4.2.2) and the π^0 mass and momentum cuts. Based on these studies, the error due to the R_2 cut is taken to be 2.6%. The other cuts

Variable	Cut Values	Change in Branching Fraction (%)
$\lvert m_{\pi^0} - M_{\pi^0}\rvert$	0.025 and 0.01 GeV/c^2	12
$\lvert\vec{p}_{\pi^0}\rvert$	0.75 and 1 GeV/c	11
$\cos\theta_\rho$ and $\cos\theta_{D^*}$	0.1 and 0.5	28
Total		32

Table 5.3: Change in the measured branching fraction due to cut variation.

were varied and the complete fit procedure was repeated. Table 5.3 gives the cut ranges studied and the change in the measured branching fraction. The cut values were chosen to give a reasonable coverage over the range of the variable without significantly changing the signal efficiency. As can be seen, the largest contribution to the systematic error comes from the variation of the helicity angle cut.

The fit method was tested by using a test data set of 1119 pb^{-1} (i.e. approximately 5% of the actual data sample) that was constructed using $B\overline{B}$ Monte Carlo and off-resonance data. This data set is independent of those used to obtain the values in Tab. 5.2. The fit was repeated using this data set instead of the on-resonance data. The results of this are given in Tab. 5.4. The value for w_{signal} obtained gives a value of $(8.46 \pm 0.75) \times 10^{-3}$ for the branching fraction. This value is 2.2σ higher than the value used in the $B\overline{B}$ Monte Carlo simulation, i.e. 6.8×10^{-3}. The contribution to the systematic error, due to this bias, was estimated by taking the quadratic difference

$$\sigma_{\text{MC}} = \frac{\sqrt{(8.46 - 6.8)^2 - 0.75^2}}{8.46} = 17.5\%. \tag{5.23}$$

Figure 5.7 shows the projections of m_ρ, m_{miss} and $\mathcal{F}$ with the components of each

Parameter	Fitted value
w_{signal}	$(3.36 \pm 0.30) \times 10^{-2}$
$w_{D^*\pi\pi^0}$	$0 \pm 5 \times 10^{-3}$
$w_{D^* a_1}$	$(1 \pm 7) \times 10^{-3}$
w_{D_1}	$(4 \pm 7) \times 10^{-3}$
w_{D_2}	$0 \pm 5 \times 10^{-3}$
$w_{q\overline{q}}$	$(6.03 \pm 0.07 \times 10^{-1})$

Table 5.4: Fitted values of the weights w_x using the test data sample.

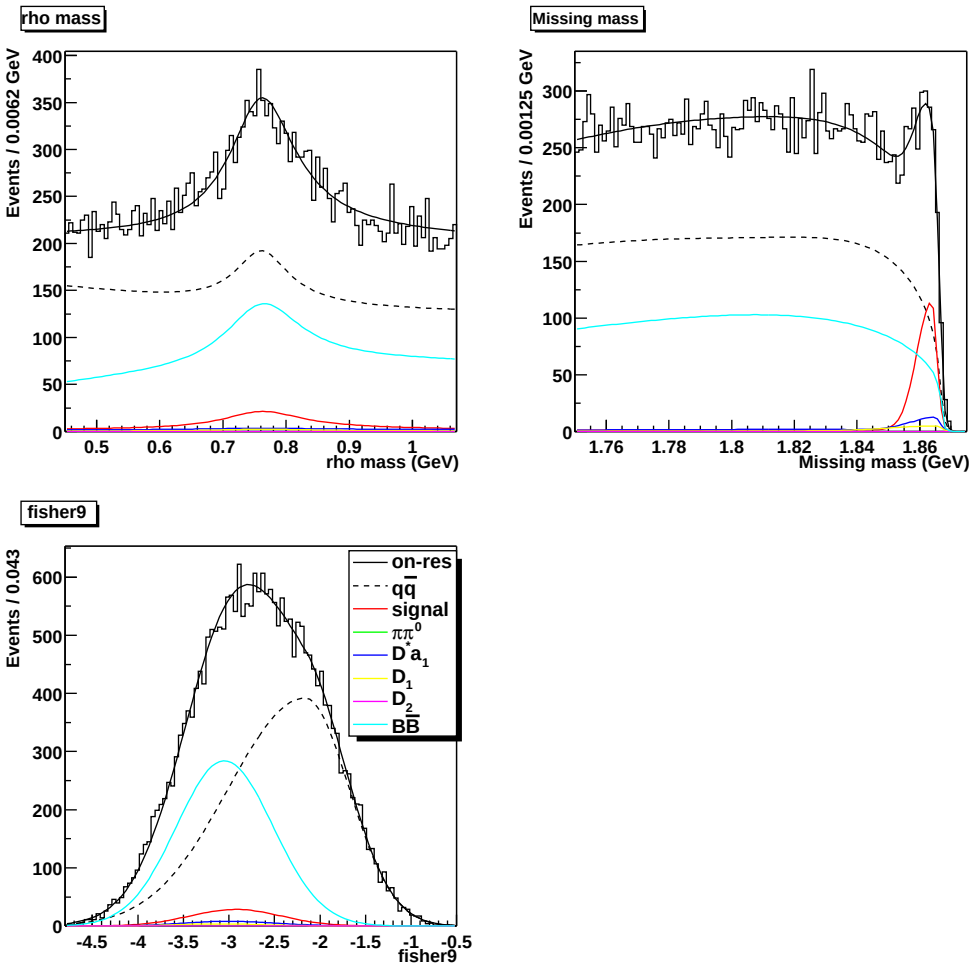

Figure 5.7: Projections of m_ρ, $m_{\rm miss}$ and $\mathcal{F}$ with the values of w_x taken from Tab. 5.4.

event type overlaid.

The error on the $B\overline{B}$ cross-section is 4.7% [29]. Studies done by other groups in the *BABAR* collaboration have recommended tracking efficiency errors of 1.3% per track and 2.6% for the slow pion [31]. The slow pion tracking error is 50% correlated with the tracking error of the fast pion. This gives an total tracking efficiency error of 3.4%. The error on the π^0 reconstruction efficiency is taken to be 5% [32]. Table 5.5 lists the contributions to the systematic error from the different sources.

5.5 Conclusions

The branching fraction was found to be

$$\mathcal{B}(B^0 \to D^{*-}\rho^+) = (4.24 \pm 0.09 \pm 1.57) \times 10^{-3} \qquad (5.24)$$

Source	Contribution to the relative systematic error (%)
Track reconstruction	3.4
π^0 reconstruction	5
$B\overline{B}$ cross-section	5
Test fit to Monte Carlo data	17
Cut variation	32
Total	37

Table 5.5: Contributions to the systematic error.

This result is consistent with the current best measurement, $(6.8 \pm 3.4) \times 10^{-3}$ [9] and has a smaller error. However, since it was necessary to fix parameters in the final fit to determine the signal yield, the systematic error does not include effects due to the correlations between the parameters of the pdfs for the different event types.

The results of the fit to the test Monte Carlo data sample showed that a significant systematic error (17.5%) had to be included to account for the discrepancy between the measured branching fraction and the branching fraction used to generate the Monte Carlo data. This discrepancy could be due to the version of the code used to reconstruct the data being different between the test Monte Carlo data set and the other data sets used to determine the background parameters.

The largest source of systematic error was found to be due to the variation of the cut on the cosine of the helicity angles. For all of the cut variation studies the systematic contribution to the error could be disentangled from the statistical error by following the method given in [34]. However, the signal efficiency in this case was higher by 12% and so the large systematic error is not due to an increase in the statistical error. The systematic error is likely to be due to differences between the Monte Carlo simulation and data. The helicity angle distribution used to generate the $B^0 \to D^{*-}\rho^+$ Monte Carlo data was taken from the CLEO experiment's measurement of the helicity amplitudes; see Sec. 7.1.2. The errors on the measurements are significant (17% and 40% for the transverse helicity amplitudes) and could be the cause of the large variation in the branching fraction. To determine if this is the case, the measurement of the helicity amplitudes needs to be improved.

The aim of measuring the branching fraction was to determine how well the partial reconstruction method is able to select $B^0 \to D^{*-}\rho^+$ events. The results of this study demonstrate that the partial reconstruction method can be used to select $B^0 \to D^{*-}\rho^+$ events with a relatively high efficiency.

Chapter 6

B Lifetime Study

> "He had scarcely finished his sentance when we heard a loud cracking noise. The bolts had given way. The dinghy was torn from its socket and thrown out into the whirlpool like a stone hurled from a sling. My head hit an iron rib, and with this violent blow I lost consciousness."
>
> 20,000 Leagues Under the Sea, Jules Verne.

The goal of this study is to determine the lifetime of the neutral B-meson using the mode $B^0 \to D^{*-}\rho^+$, where $D^{*-} \to \overline{D}^0\pi^-$ and $\overline{D}^0 \to X$. Although it is not expected that this will yield a result competitive with other measurements of the B lifetime, this study is a necessary step in determining whether it will be possible to study $CP-$violation using this reconstruction method with the mode $B^0 \to D^{*-}\rho^+$. Throughout this analysis, the charge conjugate of this decay chain is also considered. To study $CP-$violation the separation of the decay vertices of both B-mesons needs to be determined. This is also true for measuring the B^0 lifetime and therefore this study can be used to investigate how accurately the decay vertices can be measured using the partial reconstruction method.

The measurement of the B lifetime is an extension of the branching fraction measurement. This analysis uses the same variables used in the fit for the branching fraction but also includes the measured time difference (Δt) between the decays of the B mesons and its error ($\sigma_{\Delta t}$). To measure these variables requires being able to measure the separation between the decay vertex of the B that decays to $D^*\rho$ (referred to as $B_{\rm CP}$) and the other B meson (referred to as $B_{\rm tag}$). Using the partial reconstruction method introduces a complication in determining both B decay

vertices. The following sections describe how Δt is measured for the partial reconstruction method and describes the fit method and results.

6.1 Determining Δt

The decay time difference, Δt, is calculated from the measured separation of the decay vertices of both B mesons and the boost of the $\Upsilon(4S)$, i.e.

$$\Delta t = \frac{\Delta z}{\beta\gamma c}, \tag{6.1}$$

where

$$\Delta z = z_{\rm CP} - z_{\rm tag} \tag{6.2}$$

and is of the order of a few hundred micrometers and $\beta\gamma$ is close to 0.56. Using the partial reconstruction method to select events creates difficulties when measuring Δz. The fact that the decay products of the D are not identified not only gives a poorer measurement of the decay vertex of $B_{\rm CP}$ but it also means that it is harder to determine the decay products of $B_{\rm tag}$. If the decay products of the D were known it would be simple to create a list of particles assumed to have been produced by the decay of $B_{\rm tag}$. Since this is not the case, an assumption needs to be made to estimate which products come from the decay of the D in order to estimate which particles were produced by the $B_{\rm tag}$ decay. The following sections describe how the decay vertices of $B_{\rm CP}$ and $B_{\rm tag}$ are determined.

6.1.1 Determining the $B_{\rm CP}$ Vertex

Consider the decay illustrated in Fig 4.1. Since the decay products of the D are not reconstructed, the decay vertex of $B_{\rm CP}$ has to be determined using $\vec{p}_{\pi_{\rm s}}$ and $\vec{p}_{\rho}$. In principle it would be best to determine the decay vertex of the $B_{\rm CP}$ using both the π_s and the ρ but since the π_s has a very low momentum its track is usually poorly determined due to multiple scattering and the low number of points used to calculate its trajectory. Instead the position of the $B_{\rm CP}$ vertex is determined by fitting the π_f daughter of the ρ using the beamspot as a constraint. Events are rejected if the χ^2

probability of the fit is less than 1%.

6.1.2 Estimating Which Tracks Come From the D

In order to estimate which tracks come from the decay of the D, the assumption that all decay products are produced within a cone around the momentum vector of the D is made. Obviously, the size of this cone will determine how accurately the $B_{\rm tag}$ vertex can be measured and will therefore have an effect on the measurement of the B lifetime. If all the tracks from the D decay are not removed from the list of tracks assumed to come from the $B_{\rm tag}$, Δt will be biased towards 0. In order to estimate which tracks come from the D decay $\vec{p}_D$ needs to be determined. However, the fact that $\vec{p}_B$ is not exactly known leads to an ambiguity in determining $\vec{p}_D$, i.e. we end up with two solutions for $\vec{p}_D$. Both of these solutions are used to estimate which tracks come from the D decay.

To calculate these solutions, consider the decay in the CM frame as illustrated in Fig. 6.1. This shows the momentum vectors of the ρ and π_s in a right-handed coordinate system where $\vec{p}_{\pi_{\rm s}}$ is along the $\hat{z}$ direction and $\vec{p}_\rho$ is in the $\hat{y}\hat{z}$-plane. The momentum vector of the B must lie on a cone around $\vec{p}_\rho$ which subtends an angle $\theta_{{\rm B}\rho}$ given by equation 5.3, which is determined by the measured quantities. Applying four-momentum conservation to the decay of the D^* gives

$$\begin{aligned} P_{\rm D} &= P_{\rm D^*} - P_{\pi_{\rm s}} \\ m^2_{\rm D} &= m^2_{\rm D^*} + m^2_{\pi_{\rm s}} - 2E_{\rm D^*}E_{\pi_{\rm S}} + 2|\vec{p}_{\rm D^*}||\vec{p}_{\pi_{\rm s}}|\cos\theta_{{\rm D^*}\pi_{\rm s}}, \end{aligned}$$

thus

$$\cos\theta_{{\rm D^*}\pi_{\rm s}} = \frac{m^2_{\rm D} - m^2_{\rm D^*} - m^2_{\pi_{\rm s}} + 2E_{\rm D^*}E_{\pi_{\rm S}}}{2|\vec{p}_{\rm D^*}||\vec{p}_{\pi_{\rm s}}|}. \tag{6.3}$$

This gives us a cone of possible $\vec{p}_{D^*}$ solutions. Another cone of possible D^* solutions can be constructed using

$$\vec{p}_{\rm D^*} = \vec{p}_{\rm B} - \vec{p}_\rho. \tag{6.4}$$

As illustrated in Fig. 6.1, there are two solutions for the momentum vector of the D^* from the intersections of these two cones. These solutions are determined as follows.

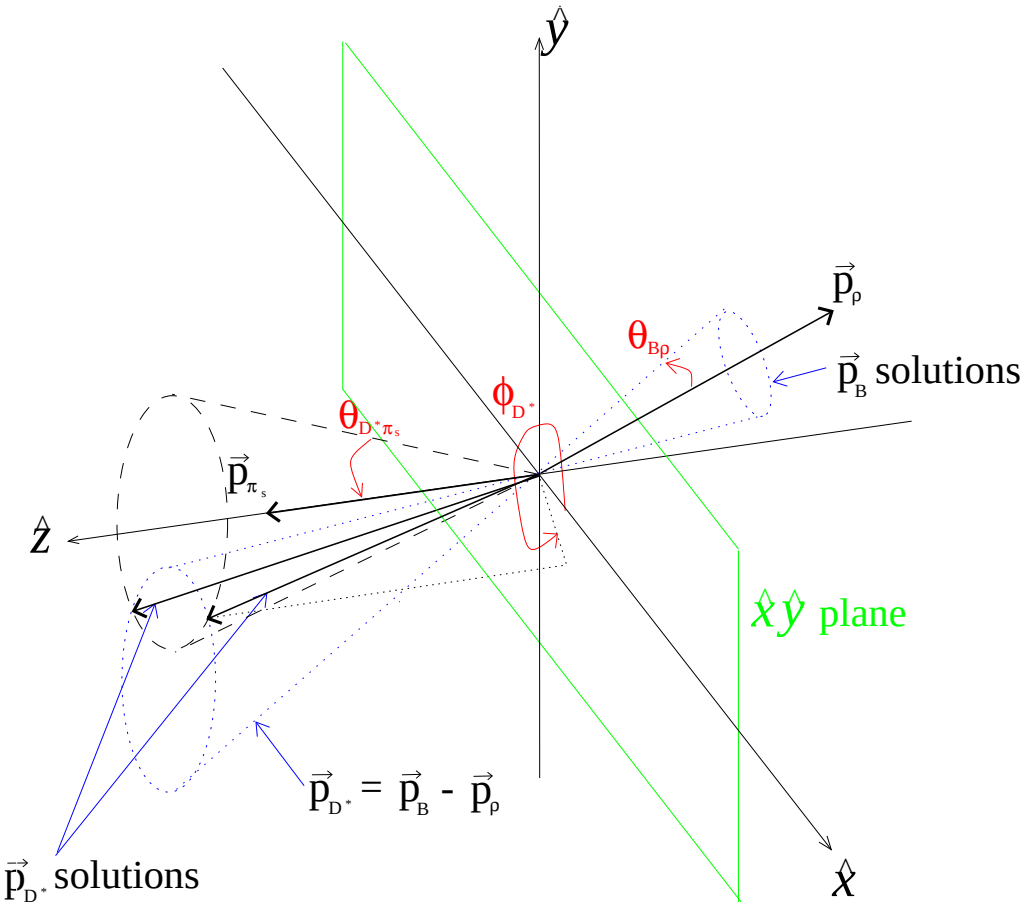

Figure 6.1: Diagram showing how the two $\vec{p}_{\mathrm{D}^*}$ solutions are determined, in the CM frame, from the intersection of the two cones given by $\vec{p}_{\mathrm{D}^*} = \vec{p}_{\mathrm{B}} - \vec{p}_{\rho}$ and the other by the angle between $\vec{p}_{\mathrm{D}^*}$ and $\vec{p}_{\pi_S}$.

The momentum vectors of the ρ and D^* in this coordinate system are given by

$$\vec{p}_{\rho} = |\vec{p}_{\rho}| \left(\sin\theta_{\rho\pi_{\mathrm{s}}}\hat{y} + \cos\theta_{\rho\pi_{\mathrm{s}}}\hat{z}\right) \tag{6.5}$$

$$\vec{p}_{\mathrm{D}^*} = |\vec{p}_{\mathrm{D}^*}| \left(\cos\phi_{\mathrm{D}^*}\sin\theta_{\mathrm{D}^*\pi_{\mathrm{s}}}\hat{x} + \sin\phi_{\mathrm{D}^*}\sin\theta_{\mathrm{D}^*\pi_{\mathrm{s}}}\hat{y} + \cos\theta_{\mathrm{D}^*\pi_{\mathrm{s}}}\hat{z}\right), \tag{6.6}$$

where ϕ_{D^*} is the azimuthal angle of $\vec{p}_{\mathrm{D}^*}$, measured anti-clockwise from the x-axis, about the z-axis. Conservation of momentum gives us

$$\vec{p}_{\mathrm{B}} = \vec{p}_{\mathrm{D}^*} + \vec{p}_{\rho}, \tag{6.7}$$

thus

$$\vec{p}_{\rho} \cdot \vec{p}_{\mathrm{B}} = \vec{p}_{\rho} \cdot \vec{p}_{\mathrm{D}^*} + |\vec{p}_{\rho}|^2. \tag{6.8}$$

Using the above expressions for $\vec{p}_\rho$ and $\vec{p}_{D^*}$ gives

$$|\vec{p}_\rho||\vec{p}_{\rm B}|\cos\theta_{{\rm B}\rho} - |\vec{p}_\rho|^2 = |\vec{p}_\rho||\vec{p}_{\rm D^*}|\left(\sin\theta_{\rho\pi_{\rm s}}\sin\theta_{{\rm D}^*\pi_{\rm s}}\sin\phi_{\rm D^*} + \cos\theta_{\rho\pi_{\rm s}}\cos\theta_{{\rm D}^*\pi_{\rm s}}\right), \quad (6.9)$$

thus

$$\sin\phi_{\rm D^*} = \frac{|\vec{p}_{\rm B}|\cos\theta_{{\rm B}\rho} - |\vec{p}_\rho| - |\vec{p}_{\rm D^*}|\cos\theta_{\rho\pi_{\rm s}}\cos\theta_{{\rm D}^*\pi_{\rm s}}}{|\vec{p}_{\rm D^*}|\sin\theta_{\rho\pi_{\rm s}}\sin\theta_{{\rm D}^*\pi_{\rm s}}}. \quad (6.10)$$

Using this and

$$\cos\phi_{\rm D^*} = \pm\sqrt{1-\sin^2\phi_{\rm D^*}} \quad (6.11)$$

in 6.6 gives the two solutions for $\vec{p}_{\rm D^*}$. Thus using

$$\vec{p}_{\rm D} = \vec{p}_{\rm D^*} - \vec{p}_{\pi_{\rm s}} \quad (6.12)$$

gives two solutions for the momentum vector of the D. Tracks are assumed to come from the D decay if they lie within a cone that subtends an angle $\theta_{\rm cone} = 1.0\,{\rm rad}$ around either solution of $\vec{p}_{\rm D}$. Figure 6.2 shows how effective this method is for different values of $\theta_{\rm cone}$.

6.1.3 Determining the $B_{\rm tag}$ Vertex

Now that the tracks assumed to come from the decay of the D have been identified it is straightforward to determine which tracks come from the $B_{\rm tag}$ decay. All tracks in the track list (defined in Section 3.3.1) are taken and then the tracks that are selected by the cone method, the π_f and the π_s are removed. The remaining tracks are assumed to come from the decay of the $B_{\rm tag}$. A standard algorithm is then used to determine the $B_{\rm tag}$ decay vertex. Initially, K^0_s mesons, Λ baryons and γ conversions are identified in the $B_{\rm tag}$ track list. The remaining tracks and composite particles are then fitted to a common vertex using the beamspot as a constraint to determine the $B_{\rm tag}$ decay vertex. If the χ^2 probability of the fit is less than 0.1% then the track with the highest contribution to the χ^2 is removed and the fit procedure is repeated. Events are rejected if the final χ^2 probability is less than 0.5%.

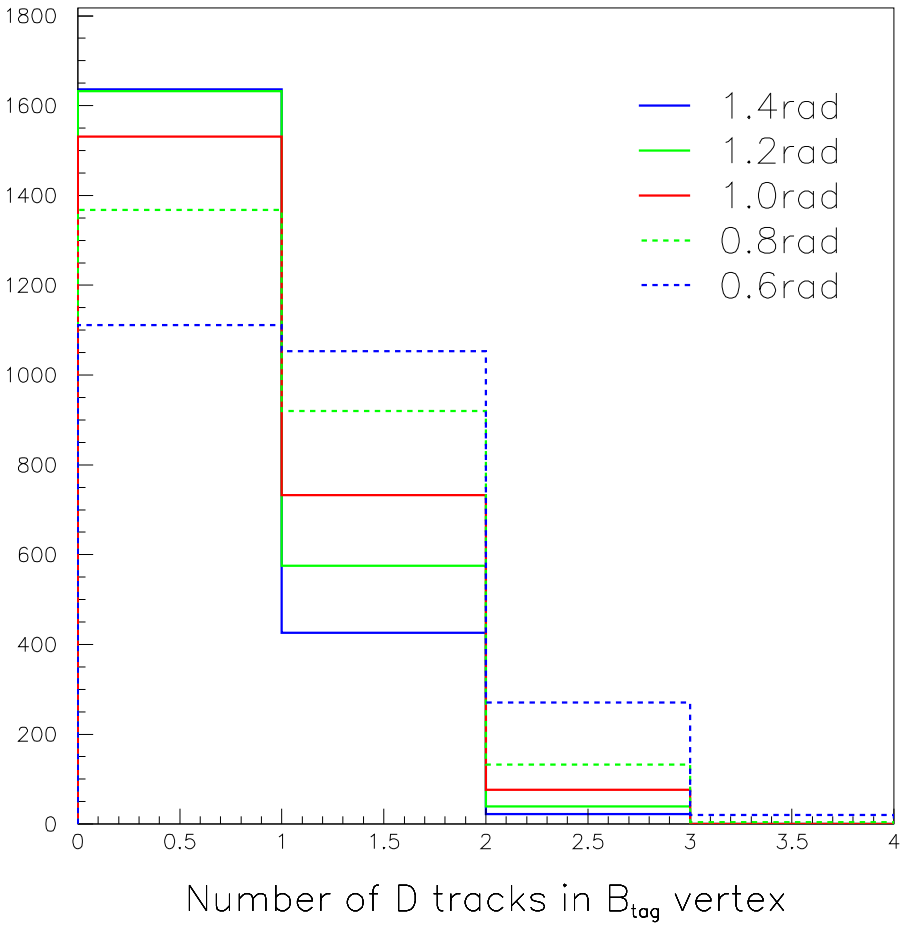

Figure 6.2: Number of tracks from the decay of the D included in the B_{tag} vertex for different sizes of cone.

6.2 Fit Procedure

The fit procedure used to fit for the B lifetime is similar to the one used for the branching fraction study. In addition to the method described in Sec. 5.1 two additional variables, Δt and $\sigma_{\Delta t}$, are included in the pdf. The joint pdf of Δt and $\sigma_{\Delta t}$ is taken to be

$$h(\Delta t, \sigma_{\Delta t}) = f(\Delta t; \sigma_{\Delta t}) \cdot g(\sigma_{\Delta t}) \tag{6.13}$$

The following sections describe the pdfs used to model the distributions of Δt and $\sigma_{\Delta t}$ for the different event types.

6.2.1 Parameterisation of the Δt Pdf

There are two pdfs used to describe the distribution of Δt for the different event types. The Δt distribution of the on-resonance data is described by

$$\begin{aligned} f_{\rm on}(\Delta t; \sigma_{\Delta t}) &= w_{\rm signal} f_{\rm sig} + w_{D^*\pi\pi^0} f_{\pi\pi^0} + w_{D^* a_1} f_{a_1} + w_{D_1} f_{D_1} + w_{D_2} f_{D_2} \\ &+ w_{q\bar{q}} f_{qq} + (1 - w_{\rm signal} - w_{D^*\pi\pi^0} - w_{D^* a_1} - w_{D_1} - w_{D_2} - w_{q\bar{q}}) f_{B\bar{B}}, \end{aligned} \tag{6.14}$$

where the weights w_x are the same as in Eq. 5.16 but the pdfs f_x only describe the Δt distribution. The functional form of $f_{\rm sig}$ and $f_{\pi\pi^0}$ is given by a 3 Gaussian resolution function convoluted with an exponential

$$f_s(\Delta t; \sigma_{\Delta t}) = \frac{1}{2\tau} e^{-|\Delta t|/\tau} \otimes \left[\begin{array}{l} c_n G_n(\Delta t; \sigma_{\Delta t}) + c_o G_o(\Delta t; \sigma_{\Delta t}) + \\ (1 - c_n - c_o) G_w(\Delta t; \sigma_{\Delta t}) \end{array} \right], \tag{6.15}$$

where G_n, G_w and G_o are the narrow, wide and outlier Gaussians of the form

$$G_i(\Delta t; \sigma_{\Delta t}, b_i, s_i) = \frac{1}{\sqrt{2\pi}\sigma_{\Delta t} s_i} \exp\left(-\frac{(\Delta t - b_i)^2}{2(\sigma_{\Delta t} s_i)^2} \right). \tag{6.16}$$

The outlier Gaussian is used to describe events with large but poorly measured Δt. The pdf used to describe the other B decay modes is given by

$$f_b(\Delta t; \sigma_{\Delta t}) = c \left(\frac{1}{2\tau_1} e^{-|\Delta t|/\tau_1} \otimes [c_n G_n(\Delta t; \sigma_{\Delta t}) + (1 - c_n) G_w(\Delta t; \sigma_{\Delta t})] \right)$$

$$+(1-c)\left(\frac{1}{2\tau_2}e^{-|\Delta t|/\tau_2}\otimes[c_nG_n(\Delta t;\sigma_{\Delta t})+(1-c_n)G_w(\Delta t;\sigma_{\Delta t})]\right). \quad (6.17)$$

For the event types described by f_b there could be a significant number of events where the π_f, assumed to come from the decay of $B_{\rm CP}$, actually comes from the $B_{\rm tag}$. In this case the measured Δz will be biased towards zero. To account for this the second exponential in f_b has its lifetime fixed at zero. The pdf used to describe $q\overline{q}$ events is taken to be

$$f_{qq}(\Delta t;\sigma_{\Delta t},b_o,s_o,c_o)=c_oG_o(\Delta t;b,s)+(1-c_o)f_b(\Delta t;\sigma_{\Delta t}), \quad (6.18)$$

where,

$$G_o(\Delta t;b_o,s_o)=\frac{1}{\sqrt{2\pi}s_o}\exp\left(-\frac{(\Delta t-b_o)^2}{2s_o^2}\right). \quad (6.19)$$

The pdf f_{qq} also includes two exponentials. The first exponential describes $c\overline{c}$ events where there can be a significant separation between the decay vertices due to the D lifetime. The second exponential describes $u\overline{u}$, $d\overline{d}$ and $s\overline{s}$ events and has the lifetime fixed at zero. The purely Gaussian term (G_o) does not include $\sigma_{\Delta t}$ and is used to describe events with large values of Δt where the track taken to be the π_f daughter of the ρ does not come from the interaction region. The results of the individual fits of the pdfs to Monte Carlo and off-resonance data, for signal, $B\overline{B}$ and $q\overline{q}$ event types, are given in Fig. 6.3.

6.2.2 Parameterisation of the $\sigma_{\Delta t}$ Pdf

The distribution of $\sigma_{\Delta t}$, for all events types, is described by

$$g(\sigma_{\Delta t})=c_gG(\sigma_{\Delta t})+(1-c_g)CB(\sigma_{\Delta t}), \quad (6.20)$$

where G is a Gaussian and CB is the Crystal Ball function [35] given by

$$CB(\sigma_{\Delta t};m,\sigma,\alpha,n)=\begin{cases}\exp\left(-(\sigma_{\Delta t}-m)^2/(2\sigma^2)\right) & ,\ \sigma_{\Delta t}>m-\alpha\sigma\\ \frac{(n/\alpha)^n\exp(-\alpha^2/2)}{((m-\sigma_{\Delta t})/\sigma+n/\alpha-\alpha)^n} & ,\ \sigma_{\Delta t}\leq m-\alpha\sigma\end{cases} \quad (6.21)$$

There is no theoretical reasoning for using this form for $g(\sigma_{\Delta t})$. However, this function fits the observed distribution well. Figure 6.4 shows the distribution of $\sigma_{\Delta t}$ and $f_{\sigma_{\Delta t}}$ for different event types.

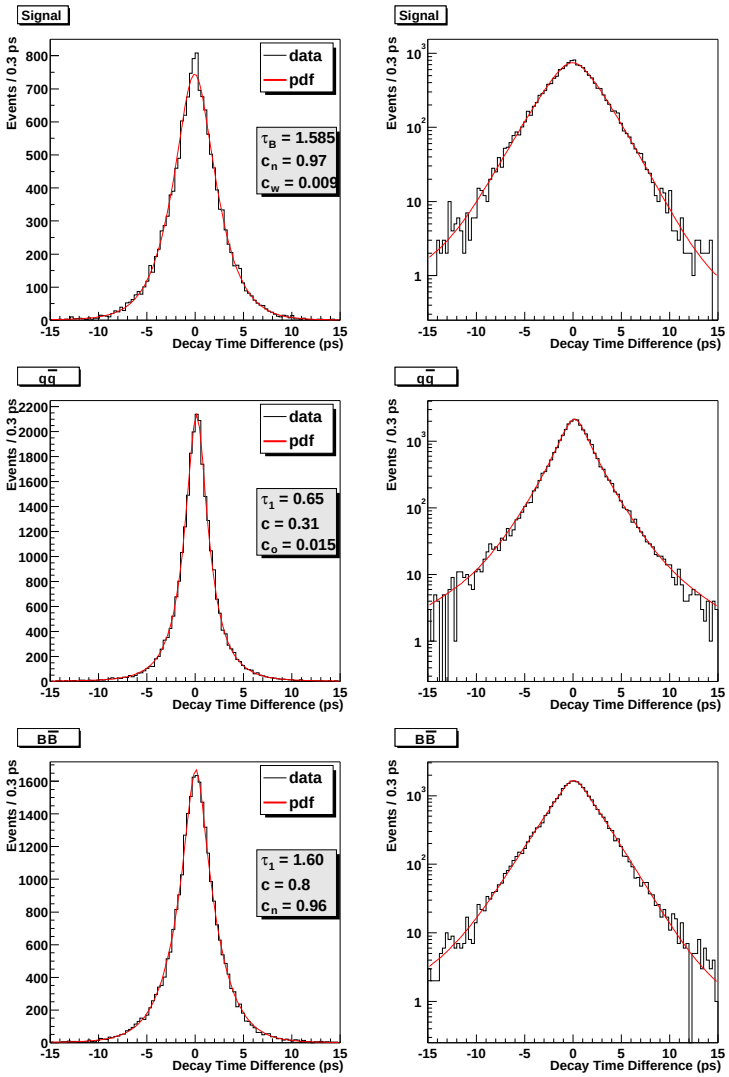

Figure 6.3: Δt distributions and fitted pdfs for signal, $q\overline{q}$ and generic $B\overline{B}$ events. The plots on the right are of the Δt distribution but with a logarithmic vertical axis. For signal and $B\overline{B}$ events, the value of the lifetime is close to the value used to generated the Monte Carlo and the narrow Gaussian dominates the resolution function. For $q\overline{q}$ events the lifetime and outlier fraction is small.

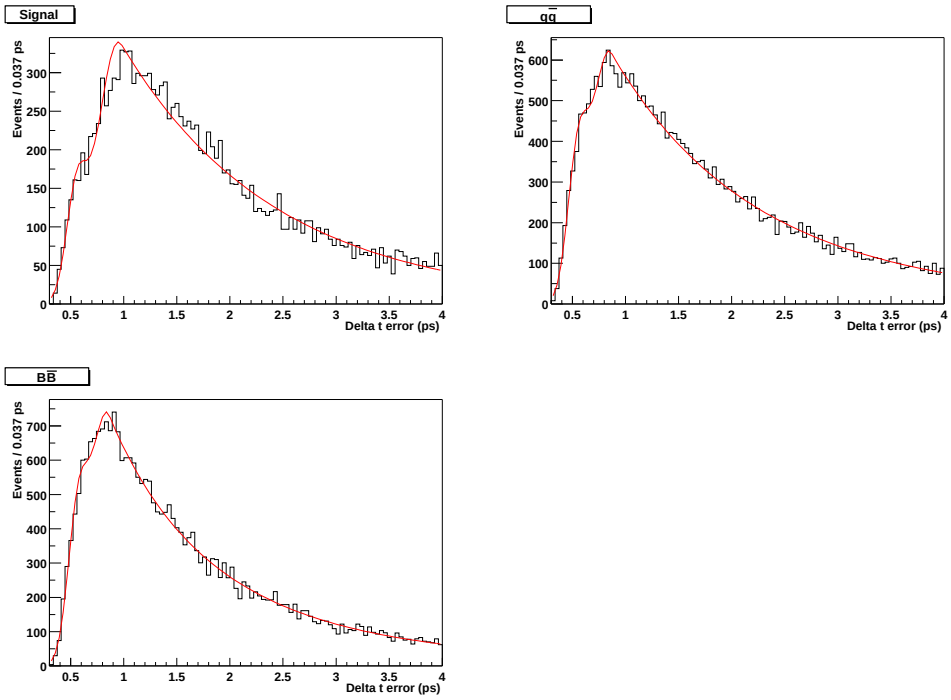

Figure 6.4: $\sigma_{\Delta t}$ distributions and fitted pdfs for signal, $q\overline{q}$ and generic $B\overline{B}$ events.

	$m_{\rm miss}$	$\mathcal{F}$	m_ρ	Δt	$\sigma_{\Delta t}$
Δt	5.53×10^{-4}	1.31×10^{-2}	-2.67×10^{-3}	1	1.55×10^{-2}
$\sigma_{\Delta t}$	4.76×10^{-2}	4.22×10^{-2}	6.84×10^{-2}	1.55×10^{-2}	1

Table 6.1: Correlations between Δt, $\sigma_{\Delta t}$ and the other variables used in the fit for the B lifetime.

6.2.3 The Global Fit

As for the branching fraction fit, the joint pdf used to describe an event type is taken to be the product of the pdfs of all the variables, i.e.

$$f_x = f_{m_\rho} \cdot f_{m_{\rm miss}} \cdot f_{\mathcal{F}} \cdot f(\Delta t, \sigma_{\Delta t}) \cdot g(\sigma_{\Delta t}). \tag{6.22}$$

Table 6.1 gives the correlations between Δt, $\sigma_{\Delta t}$ and the other variables used in the branching fraction study. Since these correlations are relatively small, the assumption that the joint pdf has the form given by Eq. 6.22 is reasonable.

The pdf that describes on-resonance data ($f_{\rm on}(m_\rho, m_{\rm miss}, \mathcal{F}, \Delta t, \sigma_{\Delta t})$) is given by equation 5.16 but with the pdfs for each event type (f_x) given by Eq. 6.22. As in the case of the branching fraction measurement, the background parameters were determined using Monte Carlo and off-resonance data and were fixed in the fit to the on-resonance data. The only parameters allowed to float in the fit were the B lifetime and the scale factors of the narrow and the wide Gaussians of the resolution function, i.e. $\tau_{\rm B}$, s_n and s_w, for the signal component of $f_{\rm on}$.

6.3 Fit Results

Table 6.2 gives the results of the fit and Fig. 6.5 shows the projections of Δt and $\sigma_{\Delta t}$ of the fitted on-resonance pdf with its individual components overlaid.

6.4 Systematic Checks

The fit method was tested using the same test Monte Carlo data sample used to test the branching fraction measurement. Table 6.3 gives the results of the fit. The

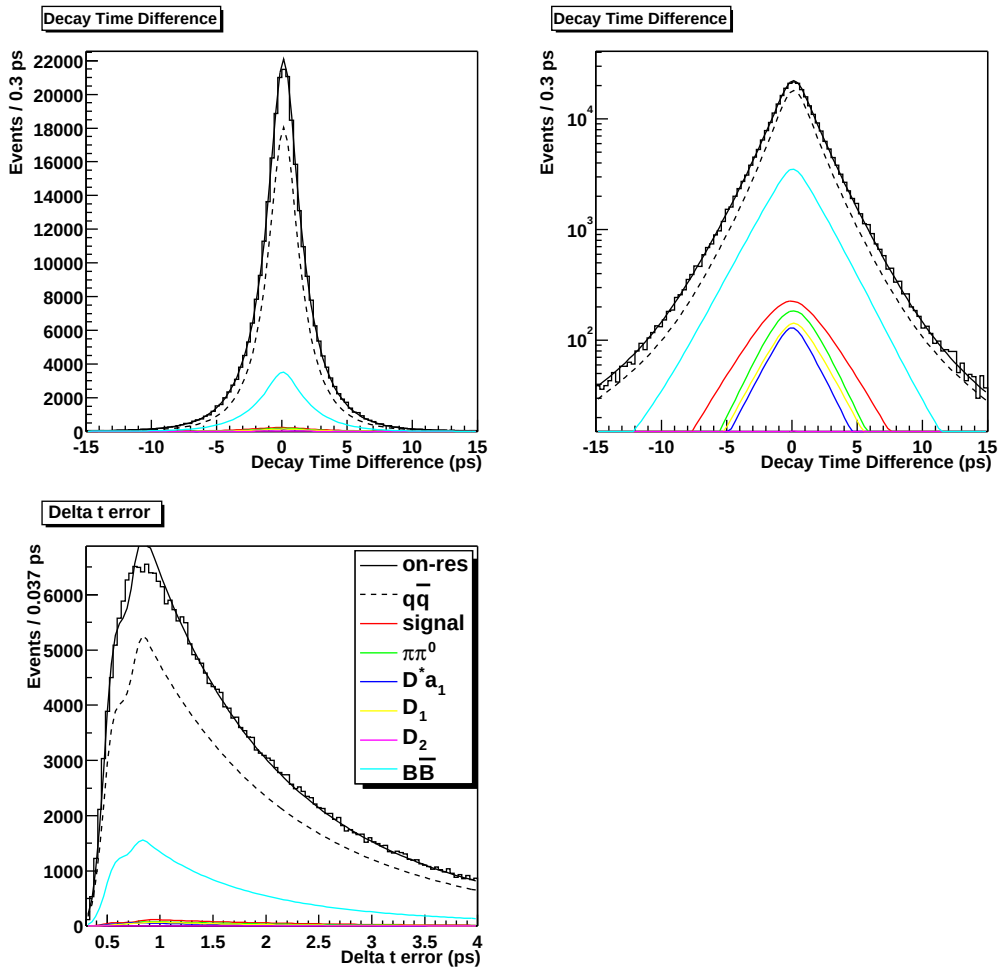

Figure 6.5: Results of the fit to the on-resonance data showing the projections of Δt and $\sigma_{\Delta t}$ of $f_{\rm on}$ with the components of each event type overlaid.

value for the B lifetime is consistent with the value of the B lifetime, 1.548 ps, used to generate the Monte Carlo data. Figure 6.6 shows the projections of Δt and $\sigma_{\Delta t}$ of the fitted pdf with the components of each event type overlaid. The systematic error due to cut variation, as described in Sec. 5.4, was looked at. However, the fit to determine the lifetime was unable to converge for each cut variation looked at.

Parameter	Fitted value
τ_{B}	1.75±0.06
s_n	1.17±0.05
s_w	7.0±3.7
w_{signal}	$(2.60\pm0.05)\times10^{-2}$
$w_{D^*\pi\pi^0}$	$0\pm9\times10^{-5}$
$w_{D^*a_1}$	$0\pm9\times10^{-5}$
w_{D_1}	$0\pm9\times10^{-5}$
w_{D_2}	$0\pm1\times10^{-4}$
$w_{q\overline{q}}$	$(7.40\pm0.02)\times10^{-1}$

Table 6.2: Fitted values of the B lifetime, the narrow and wide scale factors of the signal component and the weights w_x.

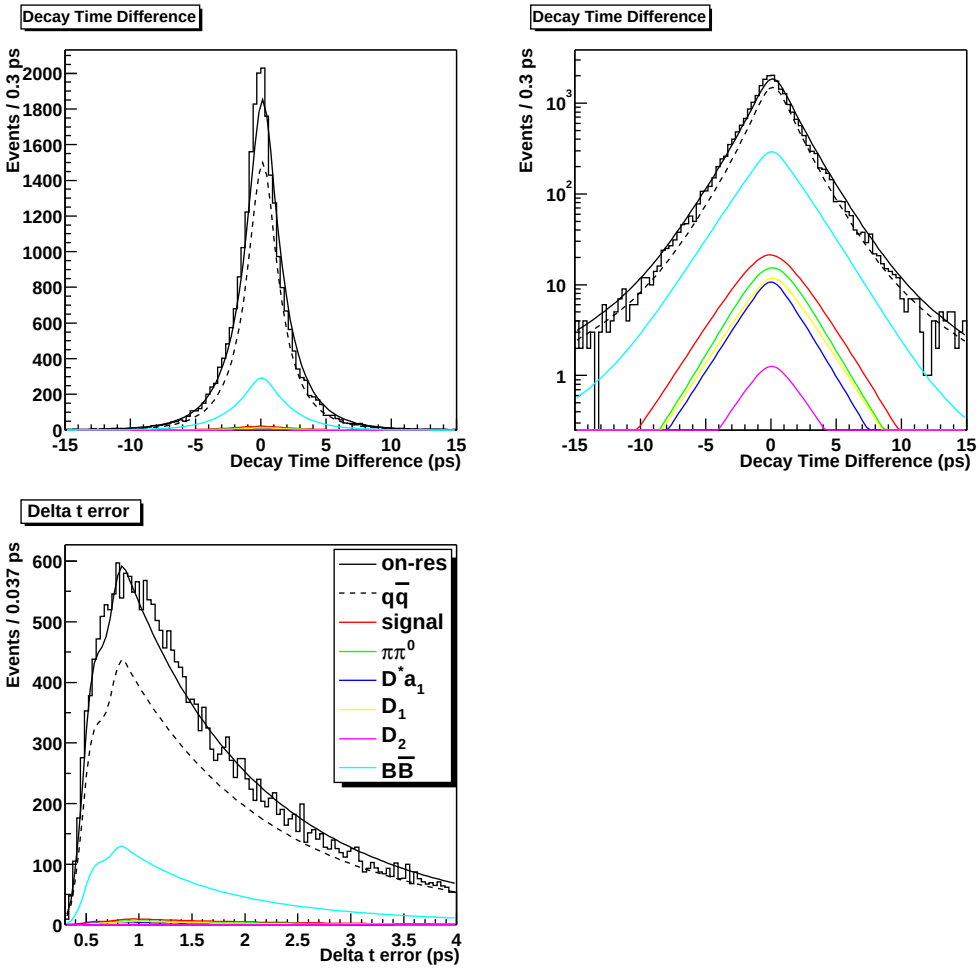

Figure 6.6: Results of the fit to the Monte Carlo test data showing the projections of Δt and $\sigma_{\Delta t}$ of the on-resonance pdf (f_{on}) with the components of each event type overlaid.

Parameter	Fitted value
τ_{B}	1.46±0.16
s_n	1.01±0.12
s_w	1.0±4.6
w_{signal}	$(3.37\pm0.35)\times10^{-2}$
$w_{D^*\pi\pi^0}$	$0\pm3\times10^{-3}$
$w_{D^*a_1}$	$(9.5\pm8.9)\times10^{-3}$
w_{D_1}	$0\pm3\times10^{-3}$
w_{D_2}	$(8.8\pm5)\times10^{-3}$
$w_{q\overline{q}}$	$(6.17\pm0.06)\times10^{-1}$

Table 6.3: Fitted values of the B lifetime, the narrow and wide scale factors of the signal component and the weights w_x using the test data sample.

6.5 Conclusions

The B lifetime was found to be 1.75 ps with a statistical error of 0.06 ps. This value is 12% higher than the current best measurement, which is 1.548 ± 0.032 ps [9]. The result of the fit to the test Monte Carlo data sample gave a value of the B lifetime consistent with the value used to generate the data. However, the Δt projection of the fitted pdf shows that although the fit converged, there is a significant discrepancy between the pdf and the data. The weights (w_x in Eq. 5.16) were found to be consistent with those in Tab. 5.4 except $w_{q\overline{q}}$, which is 19% higher. The fact that the cut variation fits failed to converge indicates that there is either a problem in the functional forms used to describe the distributions of Δt and $\sigma_{\Delta t}$ or that there is a discrepancy between the Monte Carlo and on-resonance data. Most of the background parameters are determined from fits to Monte Carlo data and are fixed in the fit to the on-resonance data. Thus, a discrepancy between Monte Carlo and on-resonance data could cause the fit to encounter problems.

The aim of the lifetime study is to determine the extent to which the partial reconstruction method can be used to measure the time between the decays of $B^0\overline{B}^0$ pairs, where one B decays to $D^{*\mp}\rho^{\pm}$. This study is therefore not intended to provide a competitive measurement of the B lifetime. The problems described above show that this method is not able to reliably determine the time between the B decays. Chapter 8 discusses ways of improving the B lifetime fit.

Chapter 7

Measuring $\sin(2\beta+\gamma)$ Using an Angular Analysis Method.

On their way back to London, I slowly wakes up on the back seat of the car. Jimi Hendrix's Voodoo Child starts playing in the background.
`I:` What's going on.
`Withnail:` I'm making time.
`I:` Are you out of your mind! Pull over, you haven't got a licence.
`Withnail:` No. I'm making time.

Withnail and I, Bruce Robinson.

The aim of the branching fraction and B lifetime measurements is to determine the extent to which, using the partial reconstruction method, it is possible to measure $\sin(2\beta+\gamma)$. There, all the information on $\sin(2\beta+\gamma)$ is obtained from the measured Δt distribution. Since the decay $B \to D^*\rho$ is a decay of a scalar particle to two vector particles, it is possible to improve the measurement by also measuring certain decay angles. This method was proposed by London, Sinha and Sinha [36]. In the simple case where only Δt is measured, the time-dependent decay rate is given by Eq. 2.48, i.e.

$$\Gamma(B^0 \to D^{*-}\rho^+) = |\mathcal{A}|^2 e^{-\Gamma\Delta t} \left[\begin{array}{l} \frac{1+|\lambda|^2}{2} + \frac{1-|\lambda|^2}{2}\cos(\Delta m \Delta t) \\ -\sin(2\beta+\gamma+\delta)\sin(\Delta m \Delta t) \end{array} \right] \qquad (7.1)$$

where λ is proportional to the ratio of the magnitudes of the amplitudes for the suppressed (Eq. 2.35) and favoured (Eq. 2.33) decays. The $\cos(\Delta m\Delta t)$ term here

is due to $B^0\overline{B}^0$ mixing and the $\sin(\Delta m\Delta t)$ term accounts for $CP-$violation effects. The coefficient of the $\sin(\Delta m\Delta t)$ term includes two angles of the CKM matrix, β and γ and the phase δ is due to strong interaction effects. In this case it is only possible to measure $\sin(2\beta+\gamma+\delta)$, i.e. it is not possible to disentangle the strong phase δ from $2\beta+\gamma$. However, by writing each of the amplitudes in Eq. 2.33-2.36 in a linear polarisation basis [37], i.e.

$$\mathcal{A} = A_0 g_0 + A_1 g_1 + iA_3 g_3, \tag{7.2}$$

$$\overline{\mathcal{A}} = \overline{A}_0 g_0 + \overline{A}_1 g_1 - i\overline{A}_3 g_3, \tag{7.3}$$

$$\mathcal{A}' = A'_0 g_0 + A'_1 g_1 - iA'_3 g_3, \tag{7.4}$$

$$\overline{\mathcal{A}}' = \overline{\mathcal{A}}'_0 g_0 + \overline{\mathcal{A}}'_1 g_1 + i\overline{\mathcal{A}}'_3 g_3, \tag{7.5}$$

where each term (A_λ) is a combination of helicity amplitudes gives

$$\Gamma(B^0 \to D^{*-}\rho^+) = e^{-\Delta t/\tau} \sum_{\lambda\leq\sigma} \left(\Lambda_{\lambda\sigma} + \Sigma_{\lambda\sigma}\cos(\Delta m\Delta t) - \rho_{\lambda\sigma}\sin(\Delta m\Delta t)\right) g_\lambda g_\sigma, \tag{7.6}$$

where $\Lambda_{\lambda\sigma}$, $\Sigma_{\lambda\sigma}$ and $\rho_{\lambda\sigma}$ are eighteen free parameters, λ and σ take the values $\{1,2,3\}$ and g_λ are functions of the decay angles, illustrated in Fig. 7.1 and are given by

$$g_1 = \cos\theta_1 \cos\theta_2, \tag{7.7}$$

$$g_2 = \frac{1}{\sqrt{2}} \sin\theta_1 \sin\theta_2 \cos\Phi, \tag{7.8}$$

$$g_3 = -\frac{1}{\sqrt{2}} \sin\theta_1 \sin\theta_2 \sin\Phi. \tag{7.9}$$

It can be seen that the form is similar to Eq. 7.1 in that there are three terms; the first term does not include Δt, the second includes a $\cos(\Delta m\Delta t)$ factor and the third has a $\sin(\Delta m\Delta t)$ factor. In this case the strong phases that appear in the coefficient of the $CP-$violation term (i.e. in $\rho_{\lambda\sigma}$) also appear in the coefficients of the other terms (i.e. also in $\Lambda_{\lambda\sigma}$ and $\Sigma_{\lambda\sigma}$). Therefore, in principle, it is possible to measure $2\beta+\gamma$ directly. However, this pdf is much more complicated than the pdf for Δt only and could give rise to computational problems. For Eq. 7.1 the statistical

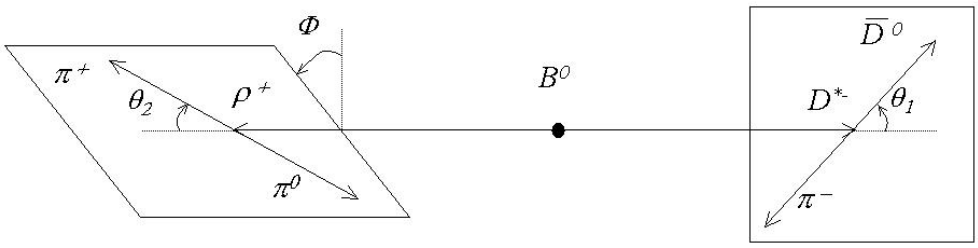

Figure 7.1: Diagram illustrating the decay angles, θ_1, θ_2 and Φ. The angle θ_1 (θ_2) is defined as the angle between the $\overline{D}^0$ (π^+) and the B direction in the D^{*-} (ρ^+) rest frame. The angle Φ is the angle between the planes that contain θ_1 and θ_2.

error on $\sin(2\beta+\gamma)$ is $\sigma_{\sin(2\beta+\gamma)} \propto 1/r^2$ but for Eq. 7.6 the error $\sigma_{\tan(2\beta+\gamma)} \propto \sqrt{r}$ [38], where r is the ratio of the magnitudes of the amplitudes of the suppressed and favoured decays. Since $r \ll 1$, this is expected to provide a significant improvement in the error on $\sin(2\beta+\gamma)$. However, since Eq. 7.6 has more parameters than Eq. 7.1 we may not get this improvement in practice. A toy Monte Carlo study was done to estimate the improvement in the error on $\sin(2\beta+\gamma)$ by doing an angular analysis. The following sections describe the details and conclusions of this analysis.

7.1 Toy Monte Carlo Study

The aim of the toy Monte Carlo study is to see if there is an advantage in using the angular analysis method proposed in [36]. In theory, there should be a significant improvement in the statistical error however, due to the complexity of the pdf, this may not be the case. Consider Eq. 7.6. Writing this out explicitly gives

$$\Gamma(B^0 \to D^{*-}\rho^+) = e^{-\Delta t/\tau}\left(A + C\cos(\Delta m \Delta t) - S\sin(\Delta m \Delta t)\right), \tag{7.10}$$

where

$$\begin{aligned} A \;=\; & \frac{a_1^2+b_1^2}{2} g_1 g_1 + \frac{a_2^2+b_2^2}{2} g_2 g_2 + \frac{a_3^2+b_3^2}{2} g_3 g_3 \\ & + \left(b_3 b_1 \sin(\delta_3^b - \delta_1^b) - a_3 a_1 \sin(\delta_3^a - \delta_1^a)\right) g_3 g_1 \\ & + \left(b_3 b_2 \sin(\delta_3^b - \delta_2^b) - a_3 a_2 \sin(\delta_3^a - \delta_2^a)\right) g_3 g_2 \\ & + \left(a_2 a_1 \cos(\delta_2^a - \delta_1^a) + b_2 b_1 \cos(\delta_2^b - \delta_1^b)\right) g_2 g_1, \end{aligned} \tag{7.11}$$

$$
\begin{aligned}
C &= \frac{a_1^2 - b_1^2}{2} g_1 g_1 + \frac{a_2^2 - b_2^2}{2} g_2 g_2 + \frac{a_3^2 - b_3^2}{2} g_3 g_3 \\
&\quad - \left(\begin{array}{l} a_3 a_1 \sin(\delta_3^a - \delta_1^a) \\ + b_3 b_1 \sin(\delta_3^b - \delta_1^b) \end{array} \right) g_3 g_1 \\
&\quad - \left(\begin{array}{l} a_3 a_2 \sin(\delta_3^a - \delta_2^a) \\ + b_3 b_2 \sin(\delta_3^b - \delta_2^b) \end{array} \right) g_3 g_2 \\
&\quad + \left(\begin{array}{l} a_2 a_1 \cos(\delta_2^a - \delta_1^a) \\ - b_2 b_1 \cos(\delta_2^b - \delta_1^b) \end{array} \right) g_2 g_1, \qquad (7.12) \\
S &= a_1 b_1 \sin(\delta_1^b - \delta_1^a - \phi) g_1 g_1 \\
&\quad + a_2 b_2 \sin(\delta_2^b - \delta_2^a - \phi) g_2 g_2 \\
&\quad - a_3 b_3 \sin(\delta_3^b - \delta_3^a - \phi) g_3 g_3 \\
&\quad - \left(\begin{array}{l} a_3 b_1 \cos(\delta_1^b - \delta_3^a - \phi) \\ + a_1 b_3 \cos(\delta_3^b - \delta_1^a - \phi) \end{array} \right) g_3 g_1 \\
&\quad - \left(\begin{array}{l} a_3 b_2 \cos(\delta_2^b - \delta_3^a - \phi) \\ + a_2 b_3 \cos(\delta_3^b - \delta_2^a - \phi) \end{array} \right) g_3 g_2 \\
&\quad + \left(\begin{array}{l} a_2 b_1 \sin(\delta_1^b - \delta_2^a - \phi) \\ + a_1 b_2 \sin(\delta_2^b - \delta_1^a - \phi) \end{array} \right) g_2 g_1 \qquad (7.13)
\end{aligned}
$$

and $\phi = 2\beta + \gamma$. In this form there are fifteen free parameters including Δm and Δt. Monte Carlo data can be generated using this pdf from which an estimate of the statistical error can be obtained and other systematic effects can be studied. Monte Carlo data is generated from this pdf using the acceptance-rejection method. The integral of Eq. 7.10 needs to be known. The Appendix describes the derivation of the analytic integral. The generation method was tested by comparing the marginal pdf for the variable x to the generated data for different values of the variable y, where x,$y = \theta_1$, θ_2, Φ and Δt. This was done for all combinations of x and y and the generated data was found to match the pdf well.

Due to the complexity of the pdf, all the parameters δ_i^a and δ_i^b were set to 1 and therefore cancel. The following sections investigate the effect of different values of a_i and b_i on the measured statistical error.

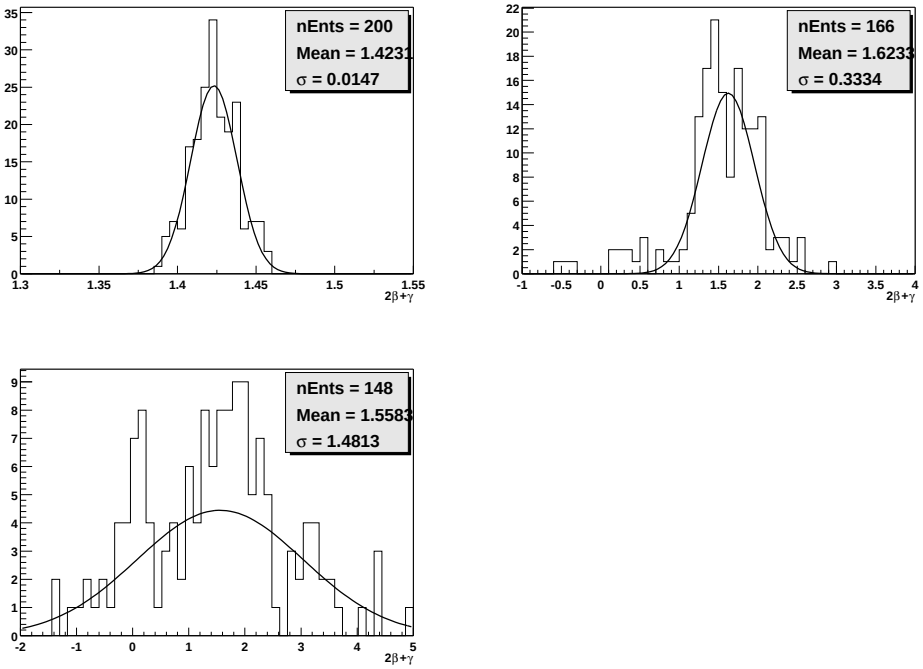

Figure 7.2: Distribution of the fitted values of $2\beta + \gamma$ for the three cases $b_i/a_i = 1$ (a), $b_i/a_i = 0.04$ (b) and $b_i/a_i = 0.01$ (c), where a_i has been set to 1.

7.1.1 Simple Case

The first scenario looked at was the simple case where all the values for a_i were set to 1 but the ratio b/a was varied. The ratio b/a is the ratio of the magnitude of the amplitude for the suppressed to non-suppressed decay. From theoretical predictions this ratio is expected to be within the range 0.01 to 0.04. The size of this ratio will affect the statistical error of $2\beta + \gamma$. Three cases were looked at $b/a = 1, 0.04$ and 0.01. The generated value of $2\beta + \gamma$ was set to 1.43, which is the best estimate from current measurements and theoretical predictions [39]. For each case 10000 events were generated 200 times. For each trial, Eq. 7.10 was used to fit the generated data to determine the value of $2\beta + \gamma$. The statistical error was measured by fitting a Gaussian to the distribution of the measured values of $2\beta + \gamma$. Figure 7.2 shows the results of the fits for the different ratios of b/a.

As can be seen, the statistical error increases as the ratio b/a decreases. So, for 10000 events, the expected statistical error is

$$\sigma_{2\beta+\gamma} \quad = \quad 0.015,$$

$$\begin{aligned} \sigma_{2\beta+\gamma} &= 0.33 \text{ and} \\ \sigma_{2\beta+\gamma} &= 1.5, \end{aligned}$$

for the three cases $b/a = 1$, $b/a = 0.04$ and $b/a = 0.01$, respectively.

7.1.2 Realistic Helicity Distributions

The simple case described above does not include the fact that the magnitudes of the amplitude for a particular helicity state are not the same. These helicity amplitudes were measured by the CLEO experiment [40] and were found to be

$$\begin{aligned} H_0 &= 0.936, \\ H_- &= 0.317 \pm 0.052 \pm 0.013, \\ H_+ &= 0.152 \pm 0.058 \pm 0.037. \end{aligned} \tag{7.14}$$

Thus, the magnitudes of the amplitudes A_λ are given by

$$\begin{aligned} a_0 = |A_0| &= |H_0| = 0.936, \\ a_1 = |A_1| &= \left| \frac{1}{\sqrt{2}} (H_+ + H_-) \right| = 0.332 \\ a_2 = |A_2| &= \left| \frac{1}{\sqrt{2}} (H_+ - H_-) \right| = 0.117. \end{aligned} \tag{7.15}$$

Since no measurements have been made of the suppressed mode, i.e. of $|\mathcal{A}'|$, the assumption is made that the magnitudes are the same as in Eq. 7.15 but are scaled by a factor. As in the simple case, three values were taken for this factor 1, 0.04 and 0.01. For these three cases, 10000 events were generated for 200 trials. For each trial all parameters, except $2\beta + \gamma$, were fixed in the fit for $2\beta + \gamma$. The results are given in Fig. 7.3. As in the simple case, the statistical error increases as b/a decreases. However, here the distribution of $2\beta + \gamma$ becomes non-Gaussian. Figures 7.4 and 7.5 show the log likelihood as a function of $2\beta+\gamma$ for six trials with $b_i/a_i = 1$ and $b_i/a_i = 0.04$. For the case $b_i/a_i = 1$ there is only one maximum around the generated value of $2\beta + \gamma$, as expected. However, for $b_i/a_i = 0.04$, there are often two local maxima. This ambiguity is due to the $\sin(2\beta + \gamma)$ term, which is

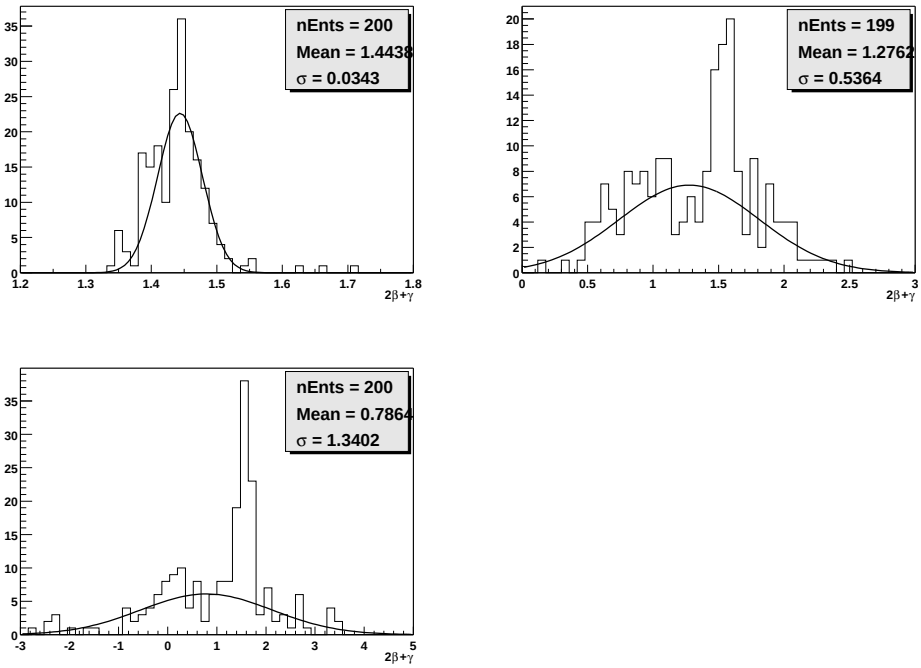

Figure 7.3: Distribution of the fitted values of $2\beta + \gamma$ for the three cases $b_i/a_i = 1$ (a), $b_i/a_i = 0.04$ (b) and $b_i/a_i = 0.01$ (c), where a_i has been set to the values given in Eq. 7.15.

symmetrical about 1.57 rad. Therefore, there will be two maxima for generated values of $2\beta + \gamma \neq 1.57\,\text{rad}$. In order to overcome this problem, Eq. 7.10 was reparameterised to be given in terms of $\sin(2\beta + \gamma)$ and not $2\beta + \gamma$.

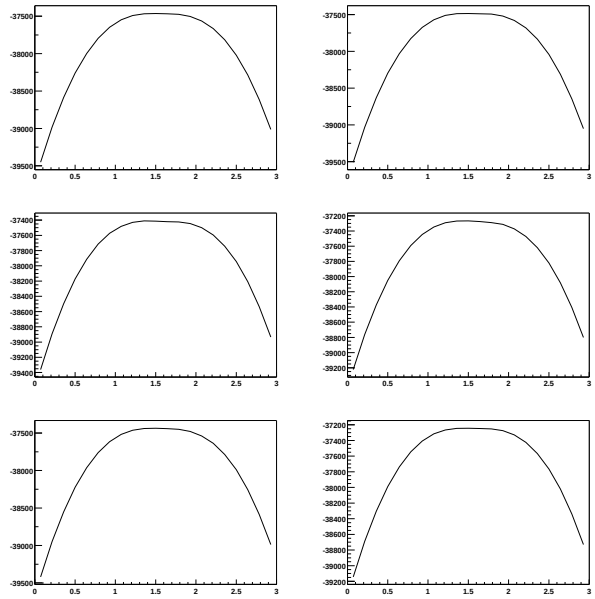

Figure 7.4: Plots showing the log likelihood versus $2\beta + \gamma$ where $b_i/a_i = 1$ for six trials.

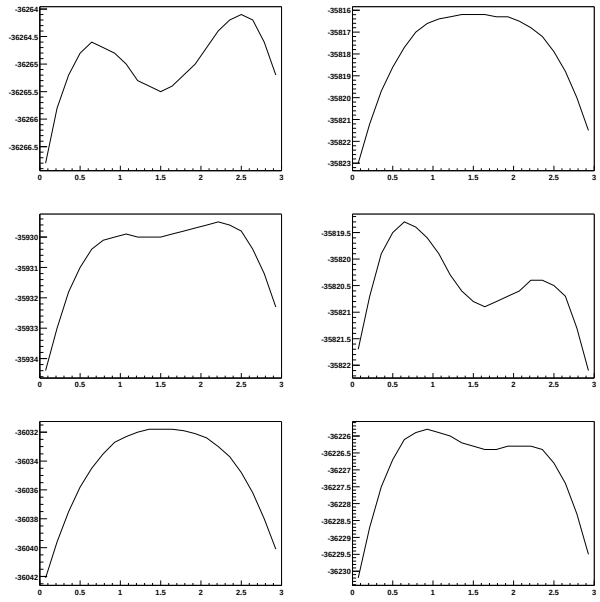

Figure 7.5: Plots showing the log likelihood versus $2\beta + \gamma$ where $b_i/a_i = 0.04$ for six trials. The two peak structure shows that the pdf is ambiguous.

7.1.3 Reparameterisation of the Angular Pdf

The need to reparameterise the pdf means that it is now no longer possible to measure $2\beta+\gamma$ directly but only $\sin(2\beta+\gamma)$. The pdf now becomes

$$\Gamma(B^0 \to D^{*-}\rho^+) = e^{-\Delta t/\tau}\left(A + C\cos(\Delta m \Delta t) - S\sin(\Delta m \Delta t)\right), \tag{7.16}$$

where

$$\begin{aligned}
A &= \frac{a_1^2+b_1^2}{2}g_1g_1 + \frac{a_2^2+b_2^2}{2}g_2g_2 + \frac{a_3^2+b_3^2}{2}g_3g_3 \\
&\quad + \left(b_3b_1\sin(\delta_3^b-\delta_1^b) - a_3a_1\sin(\delta_3^a-\delta_1^a)\right)g_3g_1 \\
&\quad + \left(b_3b_2\sin(\delta_3^b-\delta_2^b) - a_3a_2\sin(\delta_3^a-\delta_2^a)\right)g_3g_2 \\
&\quad + \left(a_2a_1\cos(\delta_2^a-\delta_1^a) + b_2b_1\cos(\delta_2^b-\delta_1^b)\right)g_2g_1, \qquad (7.17) \\
C &= \frac{a_1^2-b_1^2}{2}g_1g_1 + \frac{a_2^2-b_2^2}{2}g_2g_2 + \frac{a_3^2-b_3^2}{2}g_3g_3 \\
&\quad - \left(\begin{array}{l} a_3a_1\sin(\delta_3^a-\delta_1^a) \\ +b_3b_1\sin(\delta_3^b-\delta_1^b)\end{array}\right)g_3g_1 \\
&\quad - \left(\begin{array}{l} a_3a_2\sin(\delta_3^a-\delta_2^a) \\ +b_3b_2\sin(\delta_3^b-\delta_2^b)\end{array}\right)g_3g_2 \\
&\quad + \left(\begin{array}{l} a_2a_1\cos(\delta_2^a-\delta_1^a) \\ -b_2b_1\cos(\delta_2^b-\delta_1^b)\end{array}\right)g_2g_1 \quad \text{and} \qquad (7.18) \\
S &= \cos(2\beta+\gamma)\left(\begin{array}{l} a_1b_1\sin(\delta_1^b-\delta_1^a)g_1g_1 \\ +a_2b_2\sin(\delta_2^b-\delta_2^a)g_2g_2 \\ -a_3b_3\sin(\delta_3^b-\delta_3^a)g_3g_3\end{array}\right) \\
&\quad - \sin(2\beta+\gamma)\left(\begin{array}{l} a_1b_1\sin(\delta_1^b-\delta_1^a)g_1g_1 \\ +a_2b_2\sin(\delta_2^b-\delta_2^a)g_2g_2 \\ -a_3b_3\sin(\delta_3^b-\delta_3^a)g_3g_3\end{array}\right) \\
&\quad - \left(\begin{array}{l} \cos(2\beta+\gamma)\left(\begin{array}{l} a_3b_1\cos(\delta_1^b-\delta_3^a) \\ +a_1b_3\cos(\delta_3^b-\delta_1^a)\end{array}\right) \\ +\sin(2\beta+\gamma)\left(\begin{array}{l} a_3b_1\sin(\delta_1^b-\delta_3^a) \\ +a_1b_3\sin(\delta_3^b-\delta_1^a)\end{array}\right)\end{array}\right)g_3g_1
\end{aligned}$$

$$
\begin{aligned}
&- \left(\begin{array}{l} \cos(2\beta+\gamma) \left(\begin{array}{l} a_3 b_2 \cos(\delta_2^b - \delta_3^a) \\ +a_2 b_3 \cos(\delta_3^b - \delta_2^a) \end{array} \right) \\ +\sin(2\beta+\gamma) \left(\begin{array}{l} a_3 b_2 \sin(\delta_2^b - \delta_3^a) \\ +a_2 b_3 \sin(\delta_3^b - \delta_2^a) \end{array} \right) \end{array} \right) g_3 g_2 \\
&+ \left(\begin{array}{l} \cos(2\beta+\gamma) \left(\begin{array}{l} a_2 b_1 \sin(\delta_1^b - \delta_2^a) \\ +a_1 b_2 \sin(\delta_2^b - \delta_1^a) \end{array} \right) \\ -\sin(2\beta+\gamma) \left(\begin{array}{l} a_2 b_1 \cos(\delta_1^b - \delta_2^a) \\ +a_1 b_2 \cos(\delta_2^b - \delta_1^a) \end{array} \right) \end{array} \right) g_2 g_1 . \qquad (7.19)
\end{aligned}
$$

Figures 7.6 and 7.7 show the log-likelihood as a function of $\sin(2\beta+\gamma)$. As can be seen, the ambiguity is no longer there. Using Eq. 7.16, 200 trials of 10000 events were generated for two cases where the a_i were set to the values in Eq. 7.15 and the ratio b_i/a_i was set to 0.04 and 0.01. For each trial, all parameters, except $\sin(2\beta+\gamma)$, were fixed in the fit for $\sin(2\beta+\gamma)$. The value of $\sin(2\beta+\gamma)$ used to generate the data was 0.99. Figure 7.8 shows the distributions of $\sin(2\beta+\gamma)$ obtained for the two cases. As can be seen, the statistical error of $\sin(2\beta+\gamma)$ is 0.25 for the case where $b_i/a_i = 0.04$ and 0.9 where $b_i/a_i = 0.01$. If all the parameters are allowed to float in the fit for $\sin(2\beta+\gamma)$, 103 trials fail to find a fitted value of $\sin(2\beta+\gamma)$ for the case where $b_i/a_i = 0.04$ and 131 trials fail for $b_i/a_i = 0.01$. Figure 7.9 shows the distributions of $\sin(2\beta+\gamma)$.

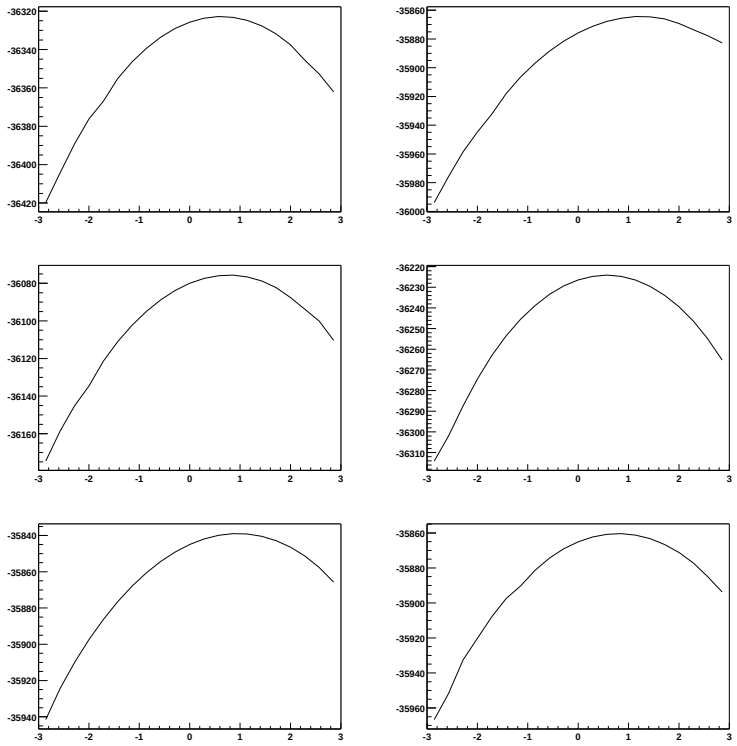

Figure 7.6: Plots showing the log likelihood versus $\sin(2\beta+\gamma)$ where $b_i/a_i = 0.04$ for six trials.

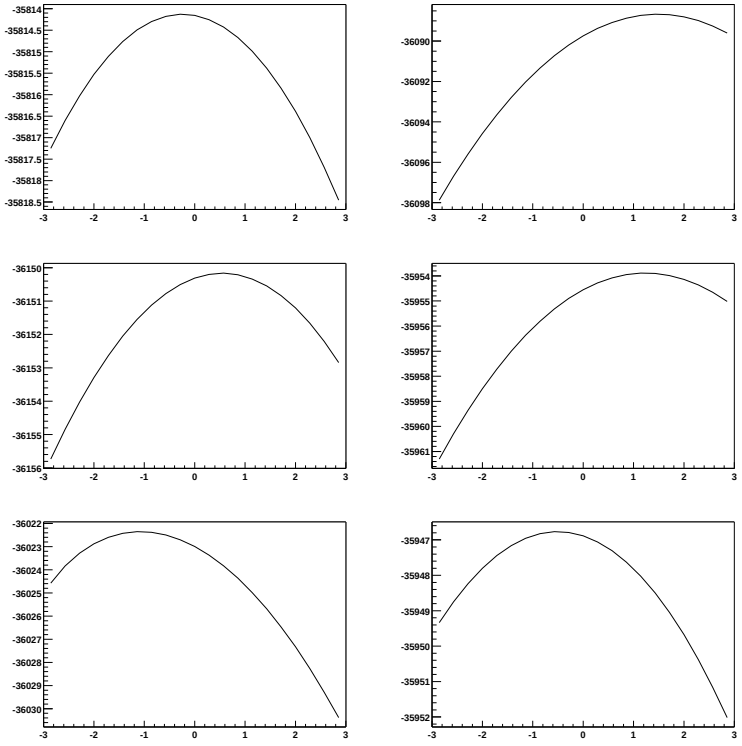

Figure 7.7: Plots showing the log likelihood versus $\sin(2\beta+\gamma)$ where $b_i/a_i = 0.01$ for six trials.

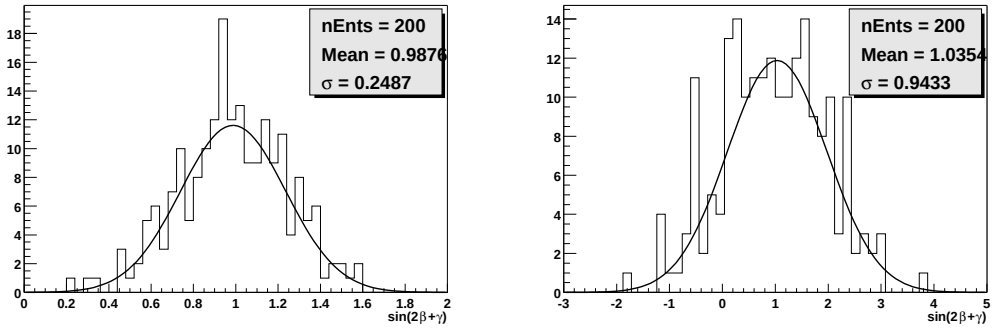

Figure 7.8: Distributions of $\sin(2\beta+\gamma)$ for the two cases where $b_i/a_i = 0.04$ and $b_i/a_i = 0.01$. For both cases, all parameters, except $\sin(2\beta+\gamma)$, were fixed in the fits.

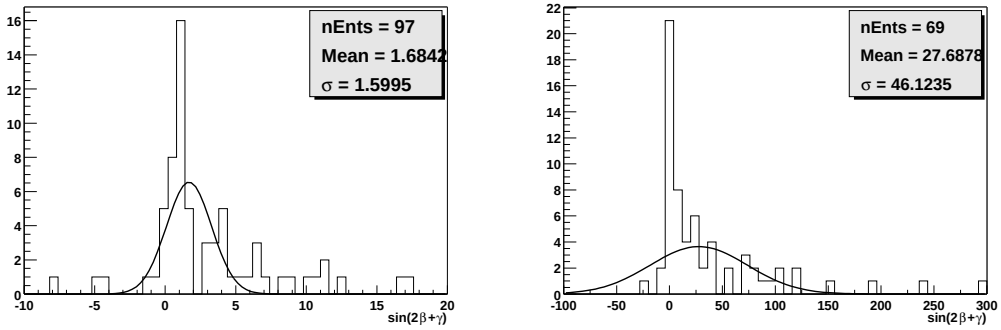

Figure 7.9: Distributions of $\sin(2\beta+\gamma)$ for the two cases where $b_i/a_i = 0.04$ and $b_i/a_i = 0.01$. For both cases, all parameters, except Δm and τ, were allowed to float in the fits.

7.2 Conclusions

The aim of this study is to investigate the extent to which the statistical error on $\sin(2\beta+\gamma)$ could be improved by using the method proposed by London, Sinha and Sinha in [36]. It was initially thought that, by using this method, it could be possible to directly measure $2\beta+\gamma$. However, it was found that using the helicity amplitudes measured by the CLEO experiment gave rise to an ambiguity in the pdf. The ambiguity in the pdf was removed by reparameterising the pdf to be specified by $\sin(2\beta+\gamma)$ instead of $2\beta+\gamma$. It is therefore not possible to directly measure $2\beta+\gamma$, as originally expected but only $\sin(2\beta+\gamma)$. The strong phases in the reparameterised pdf are separate from the $\sin(2\beta+\gamma)$ term and therefore performing the angular analysis still provides advantages over the Δt only fit. Only preliminary studies were done using the new pdf and this showed that the fit procedure often ran into numerical difficulties when all the parameters were allowed to float. If the ratio of the magnitudes of the suppressed and favoured decay is equal to its upper value, i.e. $b_i/a_i = 0.04$, then the expected error on $\sin(2\beta+\gamma)$, from approximately 100 fb^{-1} of fully reconstructed $B^0 \to D^{*-}\rho^+$ events, is 1.6.

Toy Monte Carlo studies of the Δt only pdf have been done by other groups [41]. These showed that the error on $\sin(2\beta+\gamma)$ is expected to be 0.21 with 100 fb^{-1} for the mode $B^0 \to D^{*-}\pi^+$. This is considerably smaller than the error from the angular analysis pdf. This significant increase in the error is likely to be due to the correlations between the parameters of the angular analysis pdf. Chapter 8 discusses the implications of these results and suggests further work.

Chapter 8

Conclusions and Discussion

> "How could he leave them on Christmas Eve? What harm was one more day? He turned away from the dissolving exit and crunched up the drive to 220. One more night of that pinball smile. Just one. He couldn't leave them on Christmas Eve. But, of course, in Bedford Falls it was always Christmas Eve ..."
>
> Reddwarf, Grant Naylor.

The aim of the studies presented here is to investigate different methods that could be used for measuring $\sin(2\beta+\gamma)$ with the mode $B^0 \to D^{*-}\rho^+$. The branching fraction measurement was used to demonstrate that $B^0 \to D^{*-}\rho^+$ events could be selected using the partial reconstruction method. The purpose of the B lifetime measurement was to investigate the extent to which the partial reconstruction method affects the measurement of the time difference Δt. The third study investigated the improvement in the statistical error of $\sin(2\beta+\gamma)$ by including measurements of decay angles as well as Δt. The results and their implications are discussed below.

The result of the branching fraction measurement is

$$\mathcal{B}(B^0 \to D^{*-}\rho^+) = (4.24 \pm 0.09 \pm 1.57) \times 10^{-3}, \tag{8.1}$$

which is consistent with the measurement in [9], i.e. $(6.8 \pm 3.4) \times 10^{-3}$ and has a smaller error. This shows that the partial reconstruction method can be used to select $B^0 \to D^{*-}\rho^+$ events. The major sources of systematic errors were from the test Monte Carlo data fit and the variation of the cosine of the helicity angle cut. A systematic error from the fit to the test Monte Carlo data could be due to the

version of the code used to reconstruct the test Monte Carlo data being different to that used to reconstruct the other data sets, which were used to determine the background parameters. To investigate this will require reprocessing all data sets with the newer version of the reconstruction code.

The aim of the B lifetime measurement is to determine the extent to which the partial reconstruction method can be used to measure the time between the decays of the $B^0\overline{B}^0$ pair. The measurement of this time difference, Δt, is also necessary for measuring $\sin(2\beta+\gamma)$. Therefore the measurement of the B lifetime will give an indication of how well the partial reconstruction method is able to measure Δt. The measured value of the B lifetime is 1.75 ps with a statistical error of 0.06 ps. This value is 12% higher than the current best measurement, which is 1.548 ± 0.032 ps. The fit procedure was tested using a mock data set composed of generic $B\overline{B}$ Monte Carlo and off-resonance data. These data sets are independent to the ones used to fix the background parameters of the pdfs. This test did not reveal any significant systematic error from the fit procedure. However, the study of the systematic error due to the variation of the cuts showed that there were problems with the fit method. The significant difference between the measured lifetime and the current best measurement could be due to the fit procedure or the way that Δt is measured. The fit procedure relies on the Monte Carlo data being accurate in order to determine the values of the background parameters. This dependence can be lessened by using other control samples to determine the background parameters. Another measurement of the B lifetime has been made, using $B^0 \to D^{*-}\rho^+$ and the partial reconstruction method but with a different fit procedure [42]. In this case, exclusively reconstructed decays (i.e. $B^0 \to D^{*-}\rho^+$ decays where the decay products of the D are reconstructed), are used to constrain the shape of the signal pdf. The value of the B lifetime obtained from this is $1.616 \pm 0.064 \pm 0.075$ ps, which is consistent with the current best measurement.

The purpose of the toy Monte Carlo study is to determine the extent to which the error on $\sin(2\beta+\gamma)$ can be improved by using the angular analysis method proposed by London, Sinha and Sinha. Initially, it was thought that this method could be used to directly measure $2\beta+\gamma$. It was found that this was not possible, due to the ambiguity of the pdf. However, $\sin(2\beta+\gamma)$ can be measured separately from the

strong phases using this method. This is an advantage over the Δt only method but the statistical error is expected to be approximately eight times greater. Estimates from perturbative QCD predict small values for the strong phases and these could be used with the Δt only fit to extract $\sin(2\beta+\gamma)$. However, these predictions are not believed to be very reliable [37] and so there could still be an advantage to using the angular analysis method. It is possible that the correlations between $\sin(2\beta+\gamma)$ and the other parameters could be reduced by reparameterising the pdf. One possiblity is to specify the pdf in terms of $\sin^2(2\beta+\gamma)$. All these studies have only looked at the statistical error and have not included the effects of background modes or the effects due to misidentifying the flavour of the $B_{\rm tag}$. Since the partial reconstruction method selects events with a low purity, the effect of background modes is likely to be significant. The effect of the background modes could be incorporated by including a component to the pdf. However, this would significantly increase the complexity of the pdf and is likely to lead to numerical problems. Thus, a better way to minimise the effect of the background modes would be to improve the purity of the event selection.

Appendix

This appendix gives the derivation of the analytic integral of the pdf given by Eq. 7.10, i.e.

$$\int \Gamma(\Delta t, \cos\theta_1, \cos\theta_2, \Phi)\, \mathrm{d}\Delta t\, \mathrm{d}(\cos\theta_1)\, \mathrm{d}(\cos\theta_2)\, \mathrm{d}\Phi. \tag{2}$$

First Δt is integrated over symmetrical limits from $-T$ to $+T$. The Δt dependent part of the pdf can be written as

$$\Gamma(\Delta t, \cos\theta_1, \cos\theta_2, \Phi) = e^{-|\Delta t|/\tau} \left(A + C\cos(\Delta m \Delta t) + S\sin(\Delta m \Delta t)\right), \tag{3}$$

where

$$\begin{aligned} A &= \frac{a_1^2 + b_1^2}{2} g_1 g_1 + \frac{a_2^2 + b_2^2}{2} g_2 g_2 + \frac{a_3^2 + b_3^2}{2} g_3 g_3 \\ &\quad + \left(b_3 b_1 \sin(\delta_3^b - \delta_1^b) - a_3 a_1 \sin(\delta_3^a - \delta_1^a)\right) g_3 g_1 \\ &\quad + \left(b_3 b_2 \sin(\delta_3^b - \delta_2^b) - a_3 a_2 \sin(\delta_3^a - \delta_2^a)\right) g_3 g_2 \\ &\quad + \left(a_2 a_1 \cos(\delta_2^a - \delta_1^a) + b_2 b_1 \cos(\delta_2^b - \delta_1^b)\right) g_2 g_1, \end{aligned} \tag{4}$$

$$\begin{aligned} C &= \frac{a_1^2 - b_1^2}{2} g_1 g_1 + \frac{a_2^2 - b_2^2}{2} g_2 g_2 + \frac{a_3^2 - b_3^2}{2} g_3 g_3 \\ &\quad - \begin{pmatrix} a_3 a_1 \sin(\delta_3^a - \delta_1^a) \\ + b_3 b_1 \sin(\delta_3^b - \delta_1^b) \end{pmatrix} g_3 g_1 \\ &\quad - \begin{pmatrix} a_3 a_2 \sin(\delta_3^a - \delta_2^a) \\ + b_3 b_2 \sin(\delta_3^b - \delta_2^b) \end{pmatrix} g_3 g_2 \\ &\quad + \begin{pmatrix} a_2 a_1 \cos(\delta_2^a - \delta_1^a) \\ - b_2 b_1 \cos(\delta_2^b - \delta_1^b) \end{pmatrix} g_2 g_1 \quad \text{and} \end{aligned} \tag{5}$$

$$
\begin{aligned}
S &= a_1 b_1 \sin(\delta_1^b - \delta_1^a - \phi) g_1 g_1 \\
&\quad + a_2 b_2 \sin(\delta_2^b - \delta_2^a - \phi) g_2 g_2 \\
&\quad - a_3 b_3 \sin(\delta_3^b - \delta_3^a - \phi) g_3 g_3 \\
&\quad - \left(\begin{array}{l} a_3 b_1 \cos(\delta_1^b - \delta_3^a - \phi) \\ + a_1 b_3 \cos(\delta_3^b - \delta_1^a - \phi) \end{array} \right) g_3 g_1 \\
&\quad - \left(\begin{array}{l} a_3 b_2 \cos(\delta_2^b - \delta_3^a - \phi) \\ + a_2 b_3 \cos(\delta_3^b - \delta_2^a - \phi) \end{array} \right) g_3 g_2 \\
&\quad + \left(\begin{array}{l} a_2 b_1 \sin(\delta_1^b - \delta_2^a - \phi) \\ + a_1 b_2 \sin(\delta_2^b - \delta_1^a - \phi) \end{array} \right) g_2 g_1 . \qquad (6)
\end{aligned}
$$

Thus,

$$
\begin{aligned}
\int_{-T}^{T} \Gamma(\Delta t, \cos\theta_1, \cos\theta_2, \Phi) \mathrm{d}\Delta t &= \int_{-T}^{T} e^{-|\Delta t|/\tau} \left(\begin{array}{l} A + C\cos(\Delta m \Delta t) \\ + S \sin(\Delta m \Delta t) \end{array} \right) \mathrm{d}\Delta t \\
&= A \left(\int_{-T}^{0} e^{\Delta t/\tau} \mathrm{d}\Delta t + \int_{0}^{T} e^{-\Delta t/\tau} \mathrm{d}\Delta t \right) \\
&\quad + C \left(\begin{array}{l} \int_{-T}^{0} e^{\Delta t/\tau} \cos(\Delta m \Delta t) \mathrm{d}\Delta t \\ + \int_{0}^{T} e^{-\Delta t/\tau} \cos(\Delta m \Delta t) \mathrm{d}\Delta t \end{array} \right) \\
&\quad + S \left(\begin{array}{l} \int_{-T}^{0} e^{\Delta t/\tau} \sin(\Delta m \Delta t) \mathrm{d}\Delta t \\ + \int_{0}^{T} e^{-\Delta t/\tau} \sin(\Delta m \Delta t) \mathrm{d}\Delta t \end{array} \right) . \qquad (7)
\end{aligned}
$$

Using

$$
\begin{aligned}
\int e^{ax} \cos bx \mathrm{d}x &= \frac{e^{ax}}{a^2 + b^2} (a \cos bx + b \sin bx) \qquad (8) \\
\int e^{ax} \sin bx \mathrm{d}x &= \frac{e^{ax}}{a^2 + b^2} (a \sin bx - b \cos bx) , \qquad (9)
\end{aligned}
$$

this becomes

$$
\begin{aligned}
&= A\tau \left(\left[e^{\Delta t/\tau} \right]_{-T}^{0} - \left[e^{-\Delta t/\tau} \right]_{0}^{T} \right) \\
&\quad + C \left(\begin{array}{l} \left[\frac{e^{\Delta t/\tau}}{1/\tau^2 + \Delta m^2} \left(\frac{1}{\tau} \cos(\Delta m \Delta t) + \Delta m \sin(\Delta m \Delta t) \right) \right]_{-T}^{0} \\ + \left[\frac{e^{-\Delta t/\tau}}{1/\tau^2 + \Delta m^2} \left(-\frac{1}{\tau} \cos(\Delta m \Delta t) + \Delta m \sin(\Delta m \Delta t) \right) \right]_{0}^{T} \end{array} \right)
\end{aligned}
$$

$$
\begin{aligned}
&+S\left(\begin{array}{l}\left[\frac{e^{\Delta t/\tau}}{1/\tau^2+\Delta m^2}\left(\frac{1}{\tau}\sin(\Delta m\Delta t)-\Delta m\cos(\Delta m\Delta t)\right)\right]_{-T}^{0}\\ +\left[\frac{e^{-\Delta t/\tau}}{1/\tau^2+\Delta m^2}\left(-\frac{1}{\tau}\sin(\Delta m\Delta t)-\Delta m\cos(\Delta m\Delta t)\right)\right]_{0}^{T}\end{array}\right)\\
&= 2A\tau+\frac{2C}{1/\tau^2+\Delta m^2}\left(\frac{1}{\tau}-e^{-T/\tau}\left(\begin{array}{l}\frac{1}{\tau}\cos(\Delta mT)\\ -\Delta m\sin(\Delta mT)\end{array}\right)\right). \qquad (10)
\end{aligned}
$$

To simplify this expression, the following variables are defined:

$$
\begin{aligned}
T_1 &= 2\tau, && (11)\\
T_2 &= \frac{2}{1/\tau^2+\Delta m^2}\left(\frac{1}{\tau}-e^{-T/\tau}\left(\frac{1}{\tau}\cos(\Delta mT)-\Delta m\sin(\Delta mT)\right)\right) && (12)\\
A &= c_1g_1g_1+c_2g_2g_2+c_3g_3g_3+c_4g_3g_1+c_5g_3g_2+c_6g_2g_1 && (13)\\
C &= d_1g_1g_1+d_2g_2g_2+d_3g_3g_3+d_4g_3g_1+d_5g_3g_2+d_6g_2g_1, && (14)
\end{aligned}
$$

where c_i and d_i are the coefficients of $g_\lambda g_\sigma$ in the expressions for A and C, respectively, in Eq. 4. Thus, the angle dependent part of the decay rate is given by

$$
\begin{aligned}
\Gamma(\cos\theta_1,\cos\theta_2,\Phi) &= (T_1c_1+T_2d_1)\,g_1g_1+(T_1c_2+T_2d_2)\,g_2g_2\\
&\quad+(T_1c_3+T_2d_3)\,g_3g_3+(T_1c_4+T_2d_4)\,g_3g_1\\
&\quad+(T_1c_5+T_2d_5)\,g_3g_2+(T_1c_6+T_2d_6)\,g_2g_1 \qquad (15)
\end{aligned}
$$

Substituting in the expressions for g_λ from Eq. 7.7 gives

$$
\begin{aligned}
\Gamma(\cos\theta_1,\cos\theta_2,\Phi) &= w_1\cos^2\theta_1\cos^2\theta_2+\frac{w_2}{2}\sin^2\theta_1\sin^2\theta_2\cos^2\Phi\\
&\quad+\frac{w_3}{2}\sin^2\theta_1\sin^2\theta_2\sin^2\Phi\\
&\quad-\frac{w_4}{\sqrt{2}}\sin\theta_1\cos\theta_1\sin\theta_2\cos\theta_2\sin\Phi\\
&\quad-\frac{w_5}{2}\sin^2\theta_1\sin^2\theta_2\sin\Phi\cos\Phi\\
&\quad+\frac{w_6}{\sqrt{2}}\sin\theta_1\cos\theta_1\sin\theta_2\cos\theta_2\cos\Phi, \qquad (16)
\end{aligned}
$$

where

$$
w_i = T_1c_i+T_2d_i. \qquad (17)
$$

This can be written as

$$\begin{aligned}\Gamma(\cos\theta_1,\cos\theta_2,\Phi) &= w_1x_1^2x_2^2+\frac{w_2}{2}(1-x_1^2)(1-x_2^2)\cos^2\Phi\\ &+\frac{w_3}{2}(1-x_1^2)(1-x_2^2)\sin^2\Phi\\ &-\frac{w_4}{\sqrt{2}}x_1\sqrt{1-x_1^2}x_2\sqrt{1-x_2^2}\sin\Phi\\ &-\frac{w_5}{2}(1-x_1^2)(1-x_2^2)\sin\Phi\cos\Phi\\ &-\frac{w_6}{\sqrt{2}}x_1\sqrt{1-x_1^2}x_2\sqrt{1-x_2^2}\cos\Phi, \end{aligned} \tag{18}$$

where

$$x_1 = \cos\theta_1 \tag{19}$$

$$x_2 = \cos\theta_2. \tag{20}$$

Integrating over Φ gives

$$\begin{aligned}\Gamma(\cos\theta_1,\cos\theta_2,\Phi) &= w_1x_1^2x_2^2+\frac{w_2\pi}{4}(1-x_1^2)(1-x_2^2)\cos^2\Phi\\ &+\frac{w_3\pi}{4}(1-x_1^2)(1-x_2^2)\\ &-w_4\sqrt{2}x_1\sqrt{1-x_1^2}x_2\sqrt{1-x_2^2}, \end{aligned} \tag{21}$$

since

$$\int_0^\pi \cos^2 x\mathrm{d}x = \frac{1}{2}\left[x+\frac{1}{2}\sin 2x\right]_0^\pi = \frac{\pi}{2}, \tag{22}$$

$$\int_0^\pi \sin^2 x\mathrm{d}x = \frac{1}{2}\left[x-\frac{1}{2}\sin 2x\right]_0^\pi = \frac{\pi}{2}, \tag{23}$$

$$\int_0^\pi \sin x\cos x\mathrm{d}x = \left[\frac{1}{2}\sin^2 x\right]_0^\pi = 0, \tag{24}$$

$$\int_0^\pi \sin x\mathrm{d}x = [-\cos x]_0^\pi = 2 \quad \text{and} \tag{25}$$

$$\int_0^\pi \cos x\mathrm{d}x = [\sin x]_0^\pi = 0. \tag{26}$$

Integrating this over x_1 and then x_2 gives

$$\int \Gamma(\Delta t,\cos\theta_1,\cos\theta_2,\Phi)\,\mathrm{d}\Delta t\,\mathrm{d}(\cos\theta_1)\,\mathrm{d}(\cos\theta_2)\,\mathrm{d}\Phi = \frac{4}{9}\left(w_1+\pi w_2+\pi w_3\right), \tag{27}$$

since

$$\int_{-1}^{1} x\sqrt{a^2 - x^2}\mathrm{d}x = \left[-\frac{1}{3}\left(a^2 - x^2\right)^{3/2}\right]_{-1}^{1} = 0 \text{ and} \tag{28}$$

$$\int_{-1}^{1}(1 - x^2)\mathrm{d}x = \left[x - \frac{1}{3}x^3\right]_{-1}^{1} = \frac{4}{3}. \tag{29}$$

Bibliography

[1] O. W. Greenberg, Phys. Rev. Lett. **13** (1964),598.

[2] T.D. Lee and C.N. Yang, Phys. Rev. **104** (1956), 254.

[3] C.S. Wu, E. Ambler, R.W. Haywood, D.D. Hoppes and R.P. Hudson, Phys. Rev. **105** (1957), 1413.

[4] J.H. Christenson, J. Cronin, V. Fitch and R. Turlay, Phys. Rev. Lett. **13** (1964), 138.

[5] S.L. Glashow, Nucl. Phys. **22** (1961), 579.; A. Salam, in Proceedings of the 8th Nobel Symposium, ed. N. Swartholm, Almquist and Wiksells, Stockholm (1968); S. Weinberg, Phys. Rev. Lett. **19** (1967), 1264.

[6] M. Kobayashi and K. Maskawa, Prog. Theor. Phys. **49** (1973), 652.

[7] L. Wolfenstein, Phys. Rev. Lett. **51** (1983), 1945.

[8] N. Cabibbo, Phys. Rev. Lett. **10** (1963), 531.

[9] Particle Data Group (D.E. Groom *et al.*), "Review of Particle Physics", Eur. Phys. J. C **15** (2000).

[10] P.F. Harrison and H.R. Quinn (ed.), "The *BABAR* Physics Book", SLAC-R-504 (1998).

[11] S. Stone (ed.), "B Decays", World Scientific (1994).

[12] Web site of the *BABAR* experiment, `www.slac.stanford.edu/BFROOT`.

[13] "PEP-II - An Asymmetric B Factory, Conceptual Design Report", SLAC-418 (1993).

[14] Web site of the Stanford Linear Accelerator Center, `www.slac.stanford.edu`.

[15] "*BABAR* Technical Design Report", SLAC-R-457 (1995).

[16] The *BABAR* Collaboration (B. Aubert *et al.*), "The BaBar Detector", Nucl. Instrum. Meth. A **479** (2002), 1.

[17] A. Drescher *et al.*, Nucl. Instrum. Methods **A237** (1985), 464.

[18] R. Sinkus and T. Voss, Nucl. Instrum. Methods **A391** (1997), 360.

[19] D.J. Lange, "The Evtgen Particle Decay Simulation Package", Nucl. Instrum. Meth. A **462** (2001), 152.

[20] T. Sjöstrand, "PYTHIA 5.7 and JETSET 7.4 Physics and Manual", CERN-TH 7112/93 (1993).

[21] "GEANT, Detector Description and Simulation Tool", CERN Program Library Long Writeup W5013 (1994).

[22] The CLEO Collaboration (G. Brandenburg *et al.*), Phs. Rev. Lett. **80** (1998), 2762.

[23] T.K. Nelson, Ph.D Thesis, University of California, Santa Barbara, USA, (1998).

[24] G.C. Fox and S. Wolfram, Nucl. Phys. **B149** (1979), 413; [E:ibid. **B157** (1979), 543].

[25] G. Cowan, "Statistical Data Analysis", Oxford University Press (1998), 53.

[26] CLEO Collaboration (D. M. Asner *et al.*), Phys. Rev. D **53** (1996), 1039.

[27] J.H. Kuhn and A. Santamaria, Z. Phys. **C48** (1990), 445.

[28] The ARGUS Collaboration (H. Albrecht *et al.*), Phys. Lett. **B254** (1991), 288.

[29] C. Hearty, *BABAR* Internal Note BAD#30 (2000).

[30] C. Touramanis and P. Wang, *BABAR* Internal Note BAD#229 (2001).

[31] The *BABAR* Collaboration Tracking Efficiency Web Page, `www.slac.stanford.edu/BFROOT/www/Physics/TrackEfficTaskForce/Recipe/TrackingEfficiencies.html`

[32] C. Touramanis, *BABAR* Internal Note BAD#20 (2000).

[33] A. Kurup and A. Soffer, *BABAR* Internal Note BAD#50 (2000).

[34] Particle Data Group Collaboration (K. Hagiwara *et al.*), Phys. Rev. D **66** (2002), 010001, Section 4.2.

[35] T. Skwarnicki, DESY F31-86-02 (thesis), (1986).

[36] D. London, N. Sinha and R. Sinha, Phys. Rev. Lett. **85** (2000), 1807.

[37] N. Sinha and R. Sinha, personal communication (2002).

[38] A. Soffer, personal communication (2001).

[39] A. Höcker, H. Lacker, S. Laplace and F. Le Diberder, Eur. Phys. Jour. C **21** (2001), 225.

[40] The CLEO Collaboration, ICHEP98 852, CLEO CONF 98-23 (1998).

[41] C. Voena, Presentation at the *BABAR* Collaboration Meeting April 2001.

[42] M. Krishnamurthy, A. Kurup and A. Soffer, *BABAR* Internal Note BAD#124 (2002).